Advanced methods of glaciological modelling and time series analysis

A doctoral thesis by Aslak Grinsted

Supervised by
Docent John Moore
Professor Sven-Erik Hjelt

Opponent
Dr. Martin Miles

Examiners
Professor Ralf Greve
Associate Professor Roderik van der Wal

Abstract

This thesis covers a wide range of methods and research subjects and is thus broad in scope. The methods are applied to ice cores, Antarctic blue ice areas, sea level, and large scale climate variability.

Two new ice core proxies for continentality and summer melt were developed for the Lomonosovfonna ice core, central Svalbard. The melt proxy was based on the preferential washout different ions and the continentality proxy on the amplitudes of the annual signal in $\delta^{18}O$. These proxies suggest that summers in the Barents region were as warm (or warmer) than the present during the medieval warm period. A high quality chemical record of environmental changes was proven to be preserved in the core.

A simple and flexible flow model based on the continuity equation was developed with the purpose of dating the ancient surface ice in Antarctic blue ice areas. The model has been applied to three very different ice fields in East and West Antarctica.

The wavelet coherence and singular spectrum analysis methods were advanced and a phase-aware teleconnections method was developed. The methods were utilized in isolating a ~14 year quasi-periodic component in multiple climate series from the Arctic and the equatorial Pacific. It was determined that the signals shared a common source and a linking mechanism was found. The same techniques were applied for signal enhancement in ground penetrating radar.

The proposed wide spread influence of decadal solar variability on climate was scrutinized and it was concluded that the 11-year cycle sometimes seen in climate proxy records is unlikely to be driven by solar forcing.

Global sea level was reconstructed from tide gauge data using a new ‘virtual station’ method. The 1920-1945 rate of sea level rise was as large as the rate observed during the 1990s. The impact of major volcanic eruptions on global sea level was studied and it was found that a disturbance of the global water cycle causes a rise in sea level in the first year following an eruption.

Keywords: wavelet coherence, singular spectrum analysis, non-linear trend, phase-aware teleconnections, sea level, paleoclimate, ice core, continentality, Antarctic blue ice, glacier modelling

Acknowledgements

The research for this thesis was conducted at the Arctic Centre, University of Lapland and the department of geophysics, University of Oulu.

I am most grateful to my supervisor Docent John Moore for his guidance and friendship. I also want to thank Prof. Sven-Erik Hjelt for being supportive of my pursuits into glaciological research and for being open to cooperation between Oulu and Lapland universities.

I want to express gratitude to all my co-authors, contributors, and colleagues, many of which I now count as friends. In particular, I want to thank Dr. Svetlana Jevrejeva, Anna Sinisalo, Kristiina Virkkunen, and Teija Kekonen.

To all the members of the 2003/2004 FINNARP and the 2002 Lomonosovfonna expeditions: thanks for all the great experiences.

Finally, my deepest gratitude belongs to my wife Suvikukka. You inspire me to be the best that I can.

The work was financially supported by the Thule Institute, Academy of Finland, the Maj & Tor Nessling Foundation and the Finnish Antarctic Research Programme (FINNARP).

List of original papers

The following papers comprise the work in this thesis:

I Grinsted A, Moore J, Spikes VB & Sinisalo A (2003) Dating Antarctic blue ice areas using a novel ice flow model. Geophys Res Lett 30(19). doi:10.1029/2003GL017957.

II Grinsted A, Moore JC & Jevrejeva S (2004) Application of the cross wavelet transform and wavelet coherence to geophysical time series. Nonlin Process Geophys 11: 561-566. (http://www.pol.ac.uk/home/research/waveletcoherence/).

III Grinsted A, Moore JC, Pohjola V, Martma T & Isaksson E (2006a) Svalbard summer melting, continentality, and sea ice extent from the Lomonosovfonna ice core. J Geophys Res 111: D07110. doi:10.1029/2005JD006494.

IV Grinsted A, Moore JC & Jevrejeva S (2006b) Observational evidence for volcanic impact on sea level and the global water cycle. (Manuscript).

V Moore & Grinsted (2006) Singular spectrum analysis and envelope detection: methods of enhancing the utility of ground penetrating radar data. J Glaciol 52(176): 159-163(5).

VI Moore J, Grinsted A & Jevrejeva S (2006a) Is there evidence for sunspot forcing of climate at multi-year and decadal periods? Geophys Res Lett 33: L17705. doi:10.1029/2006GL026501.

VII Jevrejeva S, Moore JC & Grinsted A (2004) Oceanic and atmospheric transport of multi-year ENSO signatures to the polar regions. Geophys Res Lett 31: L24210. doi:10.1029/2004GL020871.

VIII Jevrejeva S, Grinsted A, Moore JC & Holgate S (2006c) Nonlinear trends and multiyear cycles in sea level records. J Geophys Res 111: C09012. doi:10.1029/2005JC003229.

In the text these papers are referred to by authors and year followed by the roman numerals in superscript e.g. “Grinsted *et al.* (2006a^{III})”.

In papers V, VI, VII, and VIII, A. Grinsted was responsible for the development of the mathematical methods and their practical application, while the first author and second authors were responsible for the interpretation of the results.

Contents

1 Overview

Public interest into climate change research is increasing as people see the local impacts of anthropogenic global warming (e.g. ACIA 2004). Projecting the consequences of different courses of action (IPCC 2001a, ACIA 2004) is only one aspect of climate change research and relies on thorough understanding of the Earth climate system. Past behaviour can give clues and insights into the inner workings of the system and can serve as both calibration and validation data for the projection models. The past is also the context in which recent changes should be seen. Unfortunately systematic weather monitoring is very sparse prior to 1950 and virtually non-existent pre-1850. Proxy climate indicators from such sources as ice cores, phenology, and tree rings are very valuable. E.g. using proxy climate reconstructions there is evidence that post-1990 Northern Hemisphere (NH) mean temperatures are higher than they have been for the last 2000 years (Moberg *et al.* 2005).

At present there is a great dichotomy of opinion concerning the behaviour of the climate. In general, the modelling community sees climate from a deterministic world view where the present reality is considered to be a direct consequence of the past. In contrast, some mathematicians consider the climate to be a manifestation of stochastic scaling processes (e.g. Koutsoyiannis 2005), whereby even events such as the glacial/inter-glacial cycles may be considered 'random fluctuations'. The approach taken to climate here is to use the tools and concepts from both camps to interpret past climate records in terms of plausible hypotheses on the mechanisms of climate change.

Increases in computing power have allowed more focussed regional scale climate modelling to be done. Therefore climate proxies from the central parts of Greenland and Antarctica are no longer sufficient. There is a need for proxies from wider and more typical regions than just the large ice sheets. This is especially important in remote areas such the Arctic where instrumental data and historical evidence is limited. Advances in sea ice modelling have led to the need for better records and proxies of past sea ice extent. The distance to open water from a site can be considerably modified by the presence of sea ice. This effectively causes a more continental climate locally with larger seasonal temperature range. We can therefore hope to reconstruct past sea ice extent through a continentality proxy.

Antarctic blue ice areas have ancient ice exposed on the surface and are usually located much nearer to the coast than the traditional deep ice cores (Bintanja 1999). This is a valuable source of paleoclimatic data on the southern ocean that has not been utilized to date, largely because of difficulties in dating the ice. As with vertical ice cores, flow modelling is one approach to dating the ice. However, most BIAs are found in proximity with mountain ranges and nunataks which complicate flow modelling considerably (Bintanja 1999).

Global sea level rise (GSL) is a critical issue for billions of people on the planet. Indeed it can be argued that this is the single largest threat from anthropogenic global warming – both through the direct loss of available land area and through increased penetration of coastal flooding to inland areas. To assess the performance of models and to detect any acceleration in sea level rise, it is necessary to establish a good record of past GSL. Satellite altimetry provides the only direct measurement of sea level globally, but the altimetry data begins only in 1992. Tide gauges provide measurements of relative sea level at points located along the coast and we can reconstruct GSL back to ~1850 using these measurements. In practice, this is complicated by the time-varying spatial distribution of tide gauge records and vertical land movement of the station reference. The contributions to sea level rise can be divided into two major groups: Contributions to the total mass of the oceans and changes in the average density (due to heat content). It is important to assess the relative importance of these contributions on different time scales. Comparisons between observed and modelled regional sea level may provide answers in this respect.

2 Time series analysis

2.1 Introduction

Climate change implies a change over time and the tools from time series analysis are therefore natural choices when researching this subject. Time series analysis does not comprise a particular set of tools and is only defined by the subject of the analysis. A time series is a finite series of successive observations usually taken at regular intervals. In geophysics we encounter many such time series. Some examples are the yearly record of maximum ice extent in the Baltic Sea, monthly global sea surface temperature, or the hourly sea level at a tide gauge. Using time series analysis we can attempt to characterize, predict, and model the system. E.g. we may examine how time series from different parts of the system are linked, and in this manner gain insights into the mechanisms involved.

As physicists we may imagine the Earth climate system to be a deterministic system for which it, in theory, should be possible to write down the governing equations. We can describe the state of the system by a set of numbers such as the pressure at every point in the atmosphere. This set of values describes the state of the system completely and can be called a coordinate in the phase (/state) space of the system.

It is clear that the phase space of the climate system must be very high dimensional. However, pressure and temperature are useful concepts when dealing with the motion of billions of molecules and the laws of statistical mechanics justify the use of macro scale physics. Hence, we can hope to describe the interesting dynamical behaviour of the system in a reduced phase space with only a few active dimensions. Analyzing past behaviour of a complex system is notably different from the operational weather forecasting problem where sensitivity to initial conditions limits utility. Time series traditionally attributed to linear systems with many degrees of freedom (d.o.f.) can be generated by non-linear systems with few d.o.f. (Hilborn 2000). We can use time series analysis to uncover a pseudo-basis for the active dimensions and create a skeleton of the system dynamics in this reduced space.

2.1.1 Regression analysis

The simplest linear systems respond passively to an external forcing. Regression analysis is in these cases very useful for finding the relationship between the forcing and the response. Many systems, however, have an internal memory. The response depends both on the forcing and on the past observations of the system (e.g. a forced oscillator). Regression analysis has been generalized for such systems in e.g. auto-regressive/moving average (ARMA) analysis (Sprott 2003). These systems are very well understood, but appear to be of very limited value in real geophysical applications where non-linearities are significant (see also section 2.1.3). They are, however, valuable as they provide a simple null-hypothesis to test the significance of features, such as quasi-periodic oscillations or trends, against. This is further discussed in section 2.1.5 .

2.1.2 Stationarity

Traditional time series analysis methods generally implicitly assume that the data come from a linear dynamical system plus noise. For such systems the variability in the series can be described by a superposition of basis functions such as exponentials and sines (Sprott 2003). Obvious examples are linear trend analysis and Fourier analysis. If the signal appears complex then a high order linear model is needed to capture its variability. The value of the model can be gauged by its utility if we were to repeat the measurement. This is closely connected to the stationarity of the underlying process (Kantz & Schreiber 2004). We call a process stationary if the probability density functions (p.d.f.) of all the relevant parameters for the dynamics remain constant through time (Kantz & Schreiber 2004). Unfortunately, what is relevant change from application to application. There is no absolute test for stationarity. Instead, we may test if the observed time series show non-stationary behaviour. As a first characterization of a time series we often look at the p.d.f. and a common definition of weak stationarity is that the mean and the variance (and auto covariance) does not change over time. In reality, we often have no possibility to re-measure the time series and must instead rely on comparing the statistical properties in different windows of the time series. Following the definition for weak stationarity the dynamical behaviour of e.g. linear growth would be a non-stationary process because the mean is changing over time (Sprott 2003). In the following I will use the word stationary more loosely in the spirit of the original meaning where relevance also has importance.

2.1.3 Non-linear systems

The deterministic world view is a fundamental aspect of science which largely relies on the repeatability of experiments. It was therefore a great surprise when simple deterministic systems showed behaviour that was neither repeatable nor predictable (Lorenz 1963). A tiny change in initial conditions or a slightly different external forcing

produces wildly different outcomes even when the governing equations are known exactly. This type of behaviour has come to be known as chaos.

Chaos only occurs in systems whose governing equations are non-linear. We call such systems non-linear systems. Not all non-linear systems exhibit chaotic behaviour and some exhibit it to such a degree that it is practically indistinguishable from random noise. Linear time series analysis is applicable if the system is linear or if the chaotic behaviour can be approximated by random noise (Gershenfeld 1999). The reality is usually somewhere in between, and this is where non-linearity matters.

Natural time series such as those observed in the climate system are most likely generated by open Hamiltonian systems where energy is gained externally and dissipated internally (Lorenz 1963). The invariant sets towards which all solutions tend towards asymptotically are called strange attractors (Ruelle & Takens 1971). A long time series from a forced dissipative system can be used to reconstruct the attractor of the system because the solution of the system will densely map out the attractor in a state space of appropriate dimension. However, in practice the presence of noise and limited number of observations in almost all geophysical time series limits the usefulness of this idea.

When we consider the range of dynamical systems from the simple to the complex we find in turn: stable equilibria (fixed points), stable periodic solutions (or limit cycles), quasi-periodic solutions lying on tori, and strange attractors (Ghil *et al.* 2002). On this road to chaos we find fixed points and limit cycles. These simple attractors can still provide meaningful analogues for the system behaviour in some parts of phase space even though they may be unstable in some directions (some of their local Lyaponov exponents are positive). Such partially unstable attractors are called ‘ghost fixed points’ and ‘ghost limit cycles’ (Ghil *et al.* 2002). When the system gets close to a ghost fixed point then it will tend to linger in the neighbourhood for a time. Similarly, when the system gets close to a ghost limit cycle then it will likely follow a few orbits around the cycle. This will lead to quasi periodic behaviour as long as the system is near the ghost limit cycle.

2.1.4 Time domain versus Frequency domain

Time series do not have to be analyzed in the time domain. The observations can also be presented in other forms without loss of information. It is common to inspect the data in the frequency domain by e.g. Fourier transforming the data. The quasi-periodic behaviour of ghost limit cycles will produce peaks in the power spectral density in the frequency domain. One disadvantage of frequency domain methods is that they implicitly assume that the signal is stationary in time. Ghost limit cycles are inherently unstable and will only lead to near periodic behaviour as long as the system is in that region of phase space.

Many time domain methods also assume stationarity. To overcome the problem of non-stationarities it is common to apply the methods on sub sections or moving windows of the data. E.g. Moving averages of a time series can be used to detect regime shifts where the statistical properties change abruptly.

We can also present the data in a hybrid time-frequency domain by making spectral analysis in a moving window. This type of analysis is called Windowed Fourier

Transform (WFT). In a window of a certain size will sample more oscillations of at short wavelengths compared to long. The WFT features will therefore be more robust at short wavelengths. Further for short windows aliasing of high and low frequency components become a serious issue. The WFT represents an inaccurate and inefficient method of time-frequency localization (Torrence & Compo 1998). A more useful method of presenting the data in time-frequency space is wavelet transforms. There are two classes of wavelet transforms; the Continuous Wavelet Transform (CWT) and its discrete counterpart (DWT). The DWT is a compact representation of the data and is particularly useful for noise reduction and data compression whereas the CWT is better for intuitive feature extraction purposes.

A wavelet is a function with zero mean and that is localized in both frequency and time (Torrence & Compo 1998, Foufoula-Georgiou & Kumar 1995). The idea behind the CWT is to apply the wavelet as a series of band pass filters to the time series. The centre frequency of the band pass filters is continuously altered by stretching in the wavelet in time and normalizing it to have unit energy.

2.1.5 Statistical significance

In order not to over-interpret the information in a time series it is important to assess the statistical significance of the results. The significance is estimated by calculating the probability that the same or an even more conclusive result may have occurred by chance. In order to do that it is necessary to define what is meant by chance. This is called the null-hypothesis for the statistical test.

In many traditional methods the null hypothesis is that the signal is generated by an uncorrelated Gaussian noise process. This is called a white noise null-hypothesis because the power spectrum is flat for such a process. Geophysical time series, however, have distinctive red noise characteristics with much more variability on long wavelengths than on short. This usually reflects the fact that there is some memory in the system. The observed value at any given time is not independent from the previous observations and therefore the effective d.o.f. is usually much smaller than the number of observed values in the time series. This means that traditional methods such as correlation analysis over-estimate the significance unless this reduction in the d.o.f. is taken into account. An auto-regressive noise model of order 1 (AR1) is the simplest and most common model for red noise and this is a much better choice for the null-hypothesis than pure white noise (with an AR1 coefficient of zero). The theoretical background spectrum is usually not known and the AR1 coefficient used in the red noise null-hypothesis therefore has to be estimated from the observed series (Allen & Smith 1996).

In practice, many time series methods do not have analytical expressions for how to estimate significance against a red-noise null-hypothesis. Fortunately increased computer power allows us to simply generate many surrogate noise data series with the proposed noise characteristics and run them through our time series analysis tools. We can then easily calculate the empirical probability distribution function for the measure of interest, and hence the significance. This approach is called Monte Carlo significance testing. One of the strengths of Monte Carlo testing is that it is easy to adapt the null-hypothesis to a

particular case. It is e.g. a simple matter to generate noise with exactly the same Fourier power spectrum as the observed series (Gershenfeld 1999).

2.1.6 Method of delays

The state of an N-dimensional deterministic system can be uniquely characterized by N independent variables. The method of delays refers to a technique that enables us to sketch out a basis for the state space from a univariate time series measured in the system. The 'natural' basis spanning the state space is only defined within a specific mathematical formulation of the system and can not be retrieved from the single time series. However, it is useful to think of the measured time series $x=\{x_1, x_2, \dots, x_n\}$ as the output of a measurement function $x_i=h(\underline{y_i})$ that maps the state described by the vector $\underline{y_i}$ into a scalar x_i. The method of delays maps a univariate time series through a delay coordinate function H,

$$H(x_i) = \left(x_{i-m+1}, \cdots, x_{i-1}, x_i\right), \tag{1}$$

where m is called the embedding dimension or lag. Mapping the entire time series x through $H(x)$ will construct a trajectory matrix X with m columns and n-m+1 rows. Takens' theorem (Takens 1981) guarantees that any smooth attractor can be reconstructed using X with under certain conditions. The mathematical conditions are rarely, if ever, strictly fulfilled for geophysical time series. The concept of a measurement function is problematic for several reasons. Climate time series will contain noise and thus can not be said to be the output of a measurement function of the 'climatic state'. Further, numeric truncation errors further violates the assumption that the measurement function has a continuous first derivative. Despite this, the theorem still gives hope that we can learn as much from a trajectory in the delay coordinate system, as from a trajectory in the physically meaningful phase space.

2.1.7 Singular Spectrum Analysis (SSA)

Geophysical time series will often be highly auto correlated and the delay coordinates will hence be highly correlated. SSA extends the method of delays by linearly transforming the delay coordinates into a coordinate system where the covariance matrix is diagonal. In this respect SSA is very similar to EOF analysis and Principal Component Analysis. Further, the method successively maximizes the variance explained by the components. In this new coordinate system the individual components of the lagged time series are linearly independent. Hence, it is often reasonable to assume that the components represent signals generated by different physical mechanisms. A recommendable introduction to SSA applied to geophysical time series can be found in Ghil *et al.* (2002).

A fundamental step in SSA is to choose the embedding dimension m. Takens' theorem states that a lag more than twice the attractor dimension will be enough to hold the attractor. However, usually we do not know the attractor dimension and we find that dimensionality measures from chaotic time series analysis are not really useful in the context of SSA as the time series usually have quite limited temporal coverage. Usually the embedding dimension is chosen on the basis of what periodicities are of interest. Ghil *et al.* (2002) advice: "*The choice of m is based on a trade-off between two considerations: quantity of information extracted versus the degree of statistical confidence in that information. The former requires as wide a window as possible, i.e., a large m, while the latter requires as many repetitions of the features of interest as possible, i.e., as large a ratio n/m as possible."* As a rule of thumb m is chosen so that $n/m>5$. Vautard *et al.* (1992) suggest that SSA is typically successful at analyzing periods in the range from $m/5$ to m. Variability on longer periods will usually be represented by a single component called the 'non-linear trend'.

In order to find the projection from the delay coordinate system to the system where the variation in the principal directions are linearly independent we must first estimate the covariance matrix (C) of the trajectory matrix X (where x and X are defined in the previous section). Usually the mean is removed from x prior to its mapping through H, as this tends to give more independent columns in X. C is then diagonalized using eigenvalue decomposition. We write

$$E^T C E = \Lambda \,, \tag{2}$$

where E is a $m \times m$ unitary matrix of eigenvectors, Λ is a diagonal matrix of eigenvalues sorted by magnitude, and ^{T} denotes a transpose. The eigenvectors (or the columns in E) can be interpreted as temporal patterns in x and are called the EOFs in parallel to the spatial patterns from EOF analysis (see also section 2.2.4). We can interpret these temporal patterns as the dynamical signature left behind by orbits close to ghost limit cycles. In a sense the EOFs describe a skeleton of the underlying attractor. We project X onto the basis spanned by E,

$$A = XE \,, \tag{3}$$

where the columns in A are called the principal components (PCs). Note how a column in A also can be calculated as the convolution of x with the corresponding eigenvector in E (in reverse order). The eigenvalues tells the amount of (co)variance captured by each PC. The leading EOFs (those with highest eigenvalues) will capture the strongest temporal patterns. Noise will be distributed among all the components. SSA will always return as many components as the embedding dimension, even if the temporal structure of the signal is very simple and can be captured completely by a few components. It is therefore important to assess which SSA components are significant. In Monte Carlo SSA (MC-SSA) we check if the amount of variance (i.e. Λ) is greater than what we would expect by chance from projecting red noise onto the EOFs (Ghil *et al.* 2002).

We can reconstruct the part of x from associated with a given EOFs. We write the ith Reconstructed Component (RC) as

$$R_i = \frac{1}{M_t} A_i * E_i , \tag{4}$$

where subscript i denotes the ith column, * denotes convolution, and M_t is the number points of overlap in the convolution at any given time. The sum of all the RCs give exactly x. We can also make a partial reconstruction where we discard e.g. noise components from the sum (Moore & Grinsted 2006[V]). The ith RC can also be calculated as $M_t^{-1} x * \hat{E}_i * E_i$, where ^ means in flipped in reverse order. In the central part of the time series $M_t = m$ and we can consider $m^{-1} \hat{E}_i * E_i$ as a Finite Impulse Response (FIR) filter that we are applying to x. This FIR filter will always be symmetric and hence have a linear phase response.

2.1.8 SSA Non-linear trend

"Proper smoothing of climate time series, particularly those exhibiting non-stationary behavior (e.g., substantial trends late in the series) is essential for placing recent trends in the context of past variability." (Mann 2004). In SSA, low-frequency variability with periodicities longer than the embedding dimension is usually captured by a single component. In the literature this component has been dubbed the nonlinear trend (Ghil et al. 2002). The RC representing the trend can be considered to be the output of applying a data adaptive low pass FIR filter to x. The advantage of using this SSA derived FIR filter rather than traditional low pass filters is that leading oscillatory components will be accounted for prior to the trend detection. Below I will develop a new method of treating the boundaries as well as a new method of obtaining confidence intervals for the non-linear trend. I will use annual 'Global' Sea Surface Temperature (SST) in the latitude band 60°S-60°N calculated from ERSSTv2 (Smith & Reynolds 2004) as an example.

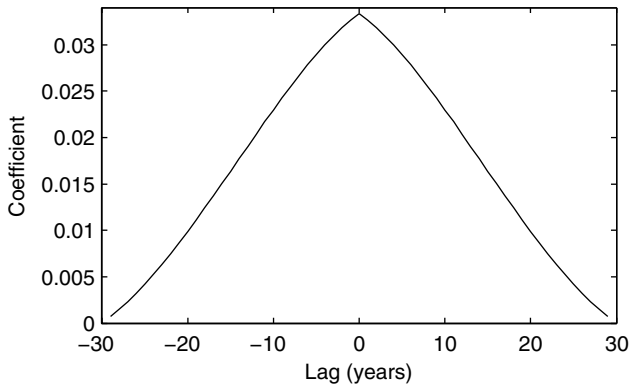

Fig. 1. Reconstructing FIR filter corresponding to the SSA (*m*=15) leading component of the global SST (60°S-60°N).

The FIR filter will reach beyond the boundaries of the time series, and it is important to consider which boundary conditions should be employed. Two useful boundary conditions are the minimum slope and the minimum roughness conditions (Mann 2004). The minimum slope condition minimizes the first derivative, and minimum roughness minimizes the second derivative at the boundary. Mann (2004) implements the minimum roughness condition by padding the series with the time series mirrored around the end point (both horizontally and vertically), and the minimum slope by mirroring horizontally. Here, I will use a variation of the minimum roughness criterion where the series is padded with a linear extrapolation based on the *m* preceding points.

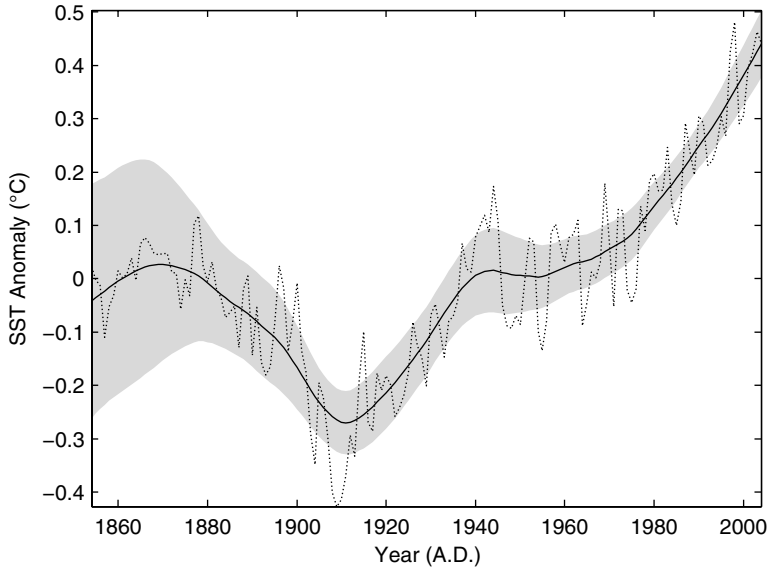

Fig. 2. The global SST anomaly (60°S-60°N) (dotted line). The SSA non linear trend (*m*=15, min. roughness) and its 2σ confidence interval is shown as a solid line and grey shading. The confidence interval is calculated from the standard errors reported for the ERSSTv2 data set.

We can estimate a confidence interval around the smoothed time series by considering the effect the FIR filter has on noise with the same characteristics (i.e. variance and colour) as the errors. In practice, this can easily be accomplished through Monte Carlo methods. The FIR filter is applied to a large surrogate set of noise series and the confidence interval is estimated from the smoothed noise distributions. We can also quantify the errors associated with the extrapolations beyond the boundary, by e.g. measuring the misfit when extrapolating an *m*-point linear trend inside the time series. This method of obtaining confidence intervals is also applicable to traditional low pass filters. In Fig. 2 I show the SSA non-linear trend and its confidence interval of the global SST.

2.2 Exploring linkages

Physical relationships between components of the climate system will be manifested in the time series we observe. Hence, we may attempt to gain insights into the underlying mechanisms by finding evidence for relationships in the observed time series. Traditionally, the similarity between time series has been measured through correlation coefficients. Similarity may, however, be caused by different things. Perhaps the similarity is a consequence of the time series being subject to the same external forcing. This is a case that occurs quite often when correlating climate series that span the industrial period. Almost all parts of the system have a clear trend due to anthropogenic global warming. Other times the similarity may be better explained by one series forcing the other. Estimated leads and lags between the signals recorded in the time series are valuable evidence for the mechanisms involved.

2.2.1 Frequency domain methods

Another tool that is often used to explore links is comparing the power spectra of the two series (e.g. Rigozo *et al.* 2002). However, the reasoning that a link should exist simply because of a similarity of a particular spectral peak is weak for several reasons. Most series have several spectral peaks it is therefore relatively likely that peaks would occur at the nearby frequencies. Secondly, a slight offset in the fundamental period would cause the oscillations to move in and out of phase. Therefore it is very important to assess whether the two series have a consistent phase relationship.

The similarity between 2 power spectra can be objectively assessed through Cross Spectral Density (CSD) estimates and the significance can be tested against red noise using Monte Carlo methods. The CSD of the time series X and Y is defined as the magnitude (complex modulus) of

$$C_{XY}(f) = F_X(f) \cdot F_Y^*(f), \tag{5}$$

where F is the Fourier transform, f is the frequency and * denotes a complex conjugate. The complex argument of C_{XY} can be interpreted as the average phase difference between the series. However, the CSD only tell how much common power there is on a given wavelength and does require a consistent phase relationship. The magnitude squared coherence (R^2) is a measure of the consistency of the phase relationship and is calculated as

$$R_{XY}^2(f) = \frac{\left|\sum_w C_{XY}(f)\right|^2}{\sum_w |F_X(f)|^2 \cdot \sum_w |F_Y(f)|^2}, \tag{6}$$

where the $\sum_w$ indicates that the terms should be summed over a series of windows. The coherence varies between zero and one, taking on the value 1 when the complex argument of C_{XY} is constant for all the windows. However, just as with the windowed Fourier transform there are several drawbacks due to the windowing involved (see section 2.1.4).

2.2.2 Time-Frequency domain methods

The ideas of the cross spectral density and the magnitude squared coherence has been applied in the time-frequency domain through continuous wavelet methods. The definition for the Cross Wavelet Transform (XWT) closely follows the definition for the Cross Spectral Density (Torrence & Compo 1998, Grinsted *et al.* 2004[II]). Assuming that a complex wavelet is used then the complex argument of the XWT can be thought of as the instantaneous relative phase at that wavelength. Parallel to the caveat with the CSD, peaks in XWT only indicate high coincident power and not a consistent phase relationship. Maraun & Kurths (2004) goes as far as stating "*The wavelet cross spectrum appears to be not suitable for significance testing the interrelation between two processes*". It is therefore useful to overlay plots of XWT with phase arrows, so that the phase relationship can be readily examined by eye. A significance test against an AR1 null hypothesis for the cross wavelet power can be found in Torrence & Compo (1998).

Wavelet Coherence (WTC) is the wavelet analogy of coherence in Fourier domain. The definition is very similar to eq. 5, with C_{XY}, F_X, and F_Y replaced by their wavelet counterparts and with the sums replaced by a smoothing operator (Torrence & Webster 1999). The significance of the WTC against red noise is done through Monte Carlo methods. However, we find that the significance level is close to independent of the noise colour (Grinsted *et al.* 2004[II]). This is because the expression for the WTC is normalized with respect to the local power under the smoothing operator. I have developed an open source wavelet coherence toolbox for Matlab, which is freely available on the web (http://www.pol.ac.uk/home/research/waveletcoherence/).

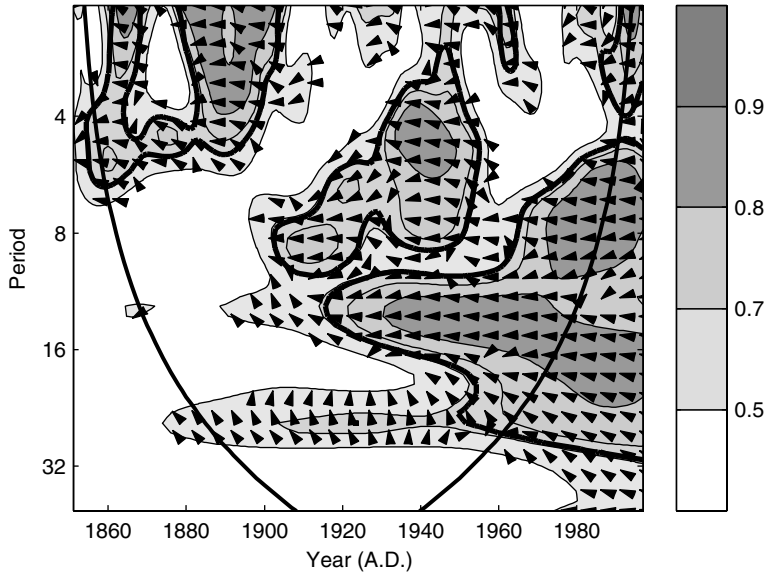

Fig. 3. Wavelet squared coherence between the standardized AO and BMI time series. The 5% significance level against red noise is shown as a thick contour. The relative phase relationship is shown as arrows (with in-phase pointing right, anti-phase pointing left, and BMI leading AO by 90º pointing straight down). The cone of influence (COI) where edge effects might distort the picture is shown as a thick black line. All significant sections show anti-phase behaviour.

An example of two physical systems that we expect to be linked from consideration of the climate system are the mean winter state of the arctic atmosphere and winter severity reflected by ice conditions. Here I will analyze winter AO (Thompson & Wallace 1998) and maximum annual ice extent in the Baltic Sea (BMI; Seinä *et al.* 2001) with special attention to the phase relationships between the series in the light of the expected causality links. Recently published results demonstrate that large-scale atmospheric circulation patterns in the Arctic and North Atlantic described by the AO or by the somewhat similar North Atlantic Oscillation teleconnections significantly control ice conditions in the Baltic Sea (Loewe & Koslowski 1998, Omstedt & Chen 2001, Jevrejeva & Moore 2001, Jevrejeva 2002).

The squared WTC of AO and BMI are shown in Fig. 3. There is strong coherence with clear anti-phase behaviour in almost all regions of time-frequency space. Oscillations in AO are manifested in the BMI on wavelengths varying from 2-20 years, suggesting that BMI passively mirrors AO. Regions with low coherence coincide with low wavelet power in the AO and are therefore expected. The reason for the low power in of AO pre-1900 could be because the associated pressure pattern is not capturing the actual location of the centres of action during the Little Ice Age.

2.2.3 Teleconnection patterns

In the 18th century Hans Egede Saabye, then a missionary in Greenland, wrote in his diary: "*In Greenland, all winters are severe, yet they are not alike. The Danes have noticed that when the winter in Denmark was severe, as we perceive it, the winter in Greenland in its manner was mild, and conversely.*" (Saabye 1942). This statement strongly suggests that what is now known as the North Atlantic Oscillation (NAO) was common knowledge at the time (see also Crantz 1765). In the book "The Kings Mirror" circa 1230 A.D., there is even some evidence that the Norse knew of this phenomenon (Stephenson *et al.* 2003). Such observations of systematic behaviour can give valuable insights into the mechanics of the climate system.

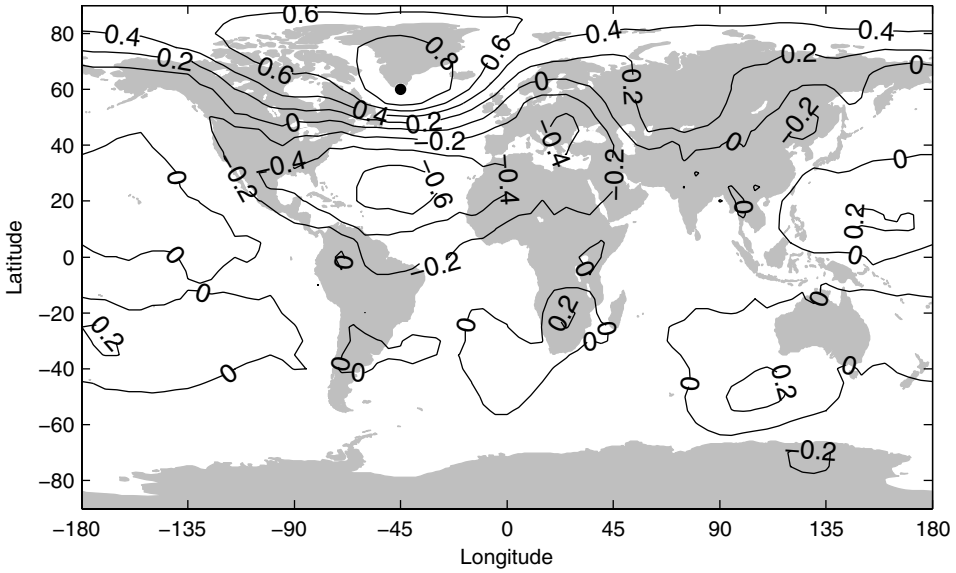

Fig. 4. South Greenland (marked with a black dot) Sea Level Pressure (SLP) teleconnection pattern. Prior to analysis the time series at each grid point has been linearly detrended. Notice the anti-correlation between the SLP in Greenland and that in Western Europe and the tropical North Atlantic.

Angström (1935) used 'teleconnection patterns' to examine the NAO see-saw. Teleconnection patterns are a quantitative method of visualizing the spatial structure of links between a gridded dataset and the observations at a given location. Traditionally the strength of the links is estimated through correlation coefficients. The term has since then been generalized so that it also encompasses correlation maps between two completely different time series. For example Bjerknes (1969) demonstrated links between a Southern Oscillation Index (SOI) derived from Sea Level Pressure (SLP) and tropical pacific sea surface temperature (SST). Based on his results he proposed a two-way coupling between ocean and atmosphere. The theory behind this coupling has since matured and is now known as the El Niño-Southern Oscillation (ENSO) (see Battisti &

Sarachik 1995 for a review). In Fig. 4 I have calculated the South Greenland teleconnection pattern in detrended SLP. The figure was made using the HADSLP2 dataset down-sampled to yearly resolution (Allan & Ansell 2006).

2.2.4 EOF analysis

Teleconnection patterns can reveal large-scale spatial climatic links. However, the climatic patterns can hardly be called fundamental as the exact structure will depend on the location of the comparison site. Empirical Orthogonal Function (EOF) analysis was developed by Lorentz (1956), as an objective method for finding the most common spatial patterns. Mathematically, the procedure is equivalent to Principal Component Analysis (PCA) which has its roots in Hotelling (1933). It is common within the geophysical community to use the term EOF for gridded data sets and PCA otherwise (e.g. Moore *et al.* 2005a).

We construct an $n \times m$ matrix (X) consisting of the values (x_{ij}) in the jth grid cell at the ith time instant. Below I will use the HADSLP2 data set as an example, and the X values are in this case the area weighted monthly anomalies of SLP. The ith row of X will be an m-dimensional vector in what I will call grid space. The objective of EOF analysis is to find a linear transformation from grid space into an orthogonal space so that there is zero covariance between the columns. We write

$$A = XE \,, \tag{7}$$

where E is the $n \times n$ matrix of eigenvectors in C sorted by their corresponding eigenvalues (λ_i) with the highest first. The variance explained by component(/column) number i of A is λ_i. Each y_{ij} will be a linear combination of the X values at the jth time instant with the coefficients ith row in E. For each component there is thus a set of coefficients to each grid cell. We can therefore make a map of these coefficients which we usually call the EOF pattern. The matrix E is called the eigenfunction matrix and in PCA terminology contains the loadings or coefficients (Sprott 2003).

It is common to use EOF analysis to create a reduced state space while minimizing the mean square residuals of the truncated representation. This can simply be done by eliminating the rows of E corresponding to the lowest eigenvalues. In practice C is often close to singular and a truncated version of E can be determined efficiently using singular value decomposition (Björnsson & Venegas 1997).

2.2.5 Instantaneous phase

Consider a time series generated by a simple harmonic oscillator (i.e. a simple sine wave). The space spanned by the time series and its numerical derivative (or alternatively a lagged version of the time series) can be considered a state space representation of the system and a trajectory in this space will form an ellipse. We can also describe the state using polar coordinates relative to the centre of this ellipse. The angle can then be

considered the instantaneous phase and the magnitude can be considered the oscillation strength or amplitude.

In geophysics we rarely find time series that are perfectly periodic. We can, however, expand the concept of instantaneous phase to signals that are quasi periodic. In this case we will be looking for a truncated representation of the true state space in 2 dimensions where the trajectory circulates around a central point. It is not necessary that the amplitude or the angular velocity is constant for the concept of instantaneous phase to be useful.

One way of isolating a quasi-periodic component is to convolute the time series with a wavelet. The centre frequency of the wavelet should be chosen so that it matches the characteristic frequency of the quasi periodic signal under investigation. It makes sense to use a complex wavelet where the complex argument directly can be considered the instantaneous phase. Another common method for extracting quasi periodic components is Singular Spectrum Analysis (SSA) which yields an orthogonal set of data adaptive filters in the time domain (see section 2.1.7). Both methods effectively band-pass filter the time series. It is important to consider how wide a pass band is appropriate for the signal. That is, the choice of wavelet and SSA lag should be considered carefully. Just as with choosing a wavelet in the wavelet transform this choice is based on a trade-off between frequency and time localization. The term 'instantaneous phase' implies that time localization is the most important, and the width of the pass band should therefore be chosen as large as possible but still restrictive enough that the filtered signal does not contain multiple quasi periodic components. In practice, I recommend examining the truncated state space trajectory to ensure that it evolves around a central point. The broad band Paul wavelet has better time localization than the Morlet (Torrence & Compo 1998) and is in many cases a good choice.

2.2.6 Phase coherence

We often come across cases where we would expect that the state of one system is related to that of another. E.g. one system could be forcing the other or the two systems could be responding to the same external forcing. The responding system can only react to the forcing as it happens and the responding system will normally lag the forcing. Hence, we would expect two time series from such systems to have a relative lag. The instantaneous phase difference of the signals is interesting as this may be interpreted as a lag. We define the phase coherence as angle strength (Zar 1999, Grinsted *et al.* 2004[II]) of the time series of phase differences (see Moore *et al.* 2006a[VI]). This can be thought of as the degree to which the signals are phase-locked. Testing the significance of the phase coherence can be done using Monte Carlo methods against any noise hypothesis. The circular mean of the relative phase angle series (Zar 1999, Grinsted *et al.* 2004[II]), can be translated into a time-lag if the angular velocities (or characteristic frequencies) are well defined.

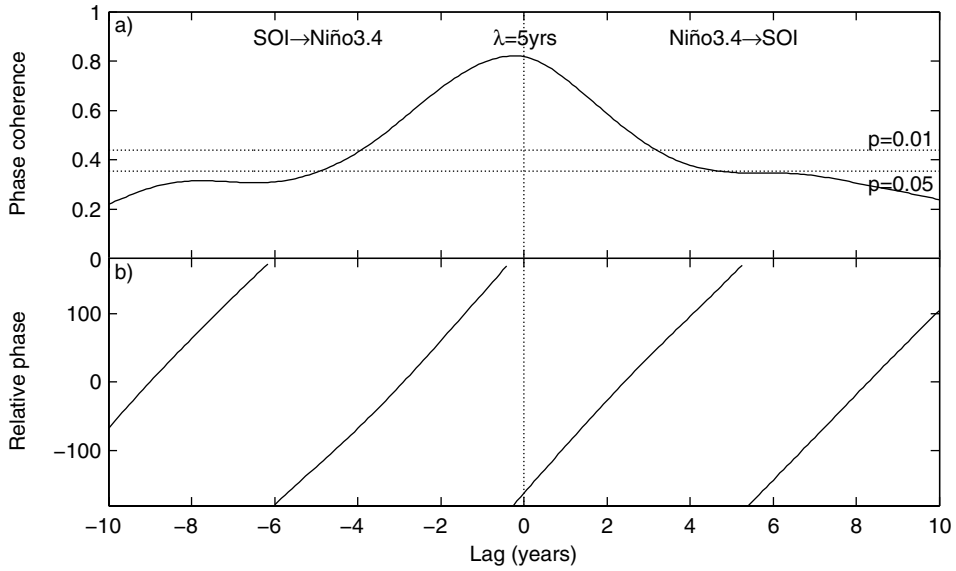

Fig. 5. a) Phase coherence between SOI and Niño3.4 over the 20th century for different lags. The instantaneous phase has been extracted using a Paul wavelet with a 5 year centre periodicity. Horizontal dotted lines indicate the significance estimated using Monte Carlo methods on surrogate series with the same Fourier power spectra as the input series. b) The mean relative phase between SOI and Niño3.4.

To illustrate how phase coherence can be utilized I will apply this technique on two El Niño-Southern Oscillation (ENSO) time series. Here, I use the monthly Southern Oscillation Index (SOI) (Ropelewski & Jones 1987), and the monthly Niño 3.4 SST index (Smith & Reynolds 2004), defined as the SST averaged over the eastern half of the tropical Pacific (5˚S–5˚N, 120˚–170˚W). Typical ENSO variability is in the 2-7 year band (e.g. Battisti & Sarachik 1995). I therefore derive the instantaneous phase by applying a complex Paul wavelet with 5 year centre periodicity to both series after removing the annual cycle. In Fig. 5a there is highest coherence for a lag of -3 months, indicating that SOI leads Niño3.4 by ~3 months as may be expected physically (Clarke *et al.* 2000, Jevrejeva *et al.* 2004[VI]). The relative phase of SOI and Niño 3.4 is -162° at zero lag (Fig. 5b), or 18° out of perfect anti-phase. At 5 year periodicity 18° also corresponds to a 3 months lead of SOI. Monte Carlo testing against white noise or red noise makes only slight difference to the significance levels in Fig. 5, with white noise significance levels being shifted down by 0.03 and white noise levels by 0.01. Hence, a red noise significance test is sufficiently robust.

2.3 Global sea level

Changes to Global Sea Level (GSL) will have a profound impact on human societies and coastal eco-systems (IPCC 2001a). The projected increase in GSL from 1990 to 2100 is

in the range from 0.08 m to 0.88 m (IPCC 2001a), with most of the uncertainty associated with future emission scenarios. The combination of a projected 40cm sea level rise and increase in population in the coastal zone in the period from 1990 to 2080 will put an additional 88-241 million people at risk from flooding, depending on the level of adaptive measures taken (IPCC 2001b). Besides increased flood risk, rising sea level also has many other socio-economic consequences such as salt water intrusions into fresh groundwater, and accelerated coastal erosion. Ecosystems that are vulnerable to sea level rise include mangrove forests, coral reefs and salt marshes.

2.3.1 Contributions to sea level rise

Sea level is determined by the total volume of water in the world oceans. Volume changes are driven by changes in both total mass and average density. Global warming is causing both to increase. Increases in the Global Oceanic Heat Content (GOHC) causes an associated thermal expansion of the world oceans. The largest non-oceanic water reservoirs (the ice sheets, glaciers, ground water, and permafrost) are all sensitive to warming. Changes in the amount of water stored in these reservoirs directly influences GSL. In Fig. 6 estimates of the different contributions to sea level rise (1910-1990) are shown.

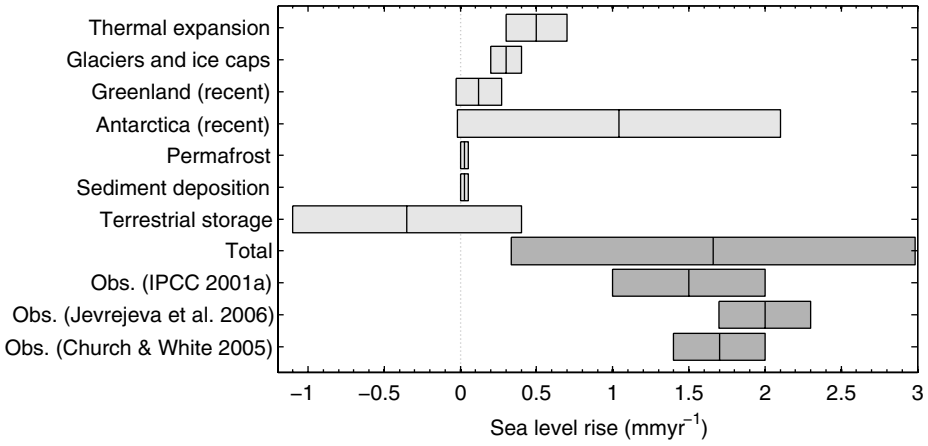

Fig. 6. Individual contributions to sea level rise from 1910-1990 (light gray) and the total of the components compared to observation based estimates of the GSL rise (dark gray). Boxes show estimates for the minimum and maximum values and centre-line does not necessarily indicate the best estimate (IPCC 2001a). Exceptions are the Greenland and Antarctic contributions which show best estimates for the recent (over a ~10 year period) mass balance and the 95% confidence interval (IPCC 2001a). The range of the total was calculated as the 95% confidence interval assuming that the component boxes indicate the 95% confidence interval. The Jevrejeva *et al.* (2006[VIII]), and Church & White (2005) estimates were calculated as the 1910-1990 linear trend of the respective GSL reconstructions and confidence intervals calculated as in Church & White (2005).

The recent contributions from ice sheets and glaciers in Fig. 6 were calculated by making a mass balance budget (IPCC 2001a). Direct measurements are usually very sparse and the estimated net balance of the large ice sheets rely on heavy extrapolation (Rignot & Thomas 2002). The modelled contributions from the ice sheets 1910-1990 are considerably lower than estimates of their recent mass balance (IPCC 2001a, Fig. 6). It is not clear if the reason for these differences is due to a recent acceleration in the contributions, model errors, or measurement extrapolation errors. An alternative method to estimate the mass balance is to weigh the ice sheets by measuring gravity changes from satellites. The GRACE project has done that since 2002 and the first estimates of the Antarctic and Greenland contributions are 0.4 ± 0.2 mm/yr (Velicogna & Wahr 2006) and 0.2 ± 0.1 mm/yr (Velicogna & Wahr 2005) respectively. These estimates for Greenland agrees with independent estimates over roughly the last decade (Krabill *et al.* 2004, Box *et al.* 2004, IPCC 2001a). It should be noted that GRACE has only been collecting data for a few years and the trends are not necessarily representative for the long term climatic trends. However, GRACE can be used to test the both mass balance models and the extrapolation methods used in traditional mass balance budget estimates. This hopefully leads to a reduction in the error bars on ice sheet contributions. Similarly, GRACE also shows promise in reducing the large error bars on the terrestrial storage term (Tapley *et al.* 2004).

Sea level rise is a relentless consequence of global warming. IPCC (2001a) states "*If greenhouse gas concentrations were stabilised, sea level would nonetheless continue to rise for hundreds of years. After 500 years, sea level rise from thermal expansion may have reached only half of its eventual level, which models suggest may lie within ranges of 0.5 to 2.0 m and 1 to 4 m for CO_2 levels of twice and four times pre-industrial, respectively.*" and continues "*Models project that a local annual-average warming of larger than 3°C sustained for millennia would lead to virtually a complete melting of the Greenland ice sheet.*" It is therefore worrying that recent studies indicate that the response time of the large ice sheets may be substantially faster than previously thought (Zwally *et al.* 2005, Cullen & Steffen 2001). Melting of the entire Greenland ice sheet corresponds to a sea level change of ~7 m and Antarctica would correspond to ~61 m allowing for isostatic rebound (IPCC 2001a).

2.3.2 Reconstructing GSL from tide gauges

Surprisingly, measuring sea level is not as easy as measuring the level of water in a bath tub. There are many difficulties and this leads to controversy when discussing recent accelerations in sea level (e.g. since the 1990s). It is also very difficult to establish what fraction of the present day rise may be attributable to simple volume changes in sea level and how much is due to an increase in ocean mass, similarly there is also dispute as to how important anthropogenic factors are and how significant are natural cycles of sea level. To resolve these issues we need to use the direct observational records of sea level. GCM modeling of sea level rise is presently not possible as the models do not have good hydrological cycle flux constraints. It is relatively little-known that the sea level rise scenarios produced by the IPCC are largely based on GCM projections of global ocean

heat content and parameterizations of mass flux from the land. Satellite altimetry now provides virtually real-time and global coverage (excluding high latitude regions – which are of course of great interest in mass flux to the oceans) of the present state of sea level, but the coverage extends back only to 1992. Beyond that we only can rely on the network of tide gauge stations, which suffer from two main limitations: being poorly distributed around the world, located at continental coastlines and on islands; and being attached to the land, which can move vertically. Paradoxically the sea level of the oceans given by satellite data are not immediately comparable with that measured by tide gauges as various coastal processes such as coastal wave propagations, storm surges, tectonic movement, coastal erosion, development, and floods can dramatically alter local coastal sea level measurements (IPCC 2001a).

Disturbances to the tide gauge or its platform can be accounted for by measuring the sea level relative to geodetic reference benchmarks. Such records are called Revised Local Reference (RLR) records and are suitable for reconstructing GSL. However, vertical land movement of RLR benchmarks complicates the use of tide gauge records for GSL reconstruction. In particular land is still rebounding due to the removal of the large ice load at the last deglaciation. E.g. regions that were under ice are now steadily emerging and other are compensating by submerging (Douglas 1995, Peltier 2001). Hence, we have to correct the RLR records for the ongoing Global Isostatic Adjustment (GIA) before they capture sea level. Any error in the GIA corrections will cause a corresponding error in the GSL trend. Most recent studies have relied on either models of post-glacial rebound or geological evidence for the GIA corrections. Geological evidence has the disadvantage that it measures past vertical land movement which is not necessarily the same as the present. The GIA models rely on assumptions of the Earths interior and a loading history. Any errors in these assumptions will create errors that are coherent on large spatial scales. Unfortunately this means that averaging many tide gauge records does not necessarily reduce the error from the GIA model. Other sources of vertical land movement such as tectonic activity (especially earth-quakes) and coastal subsidence in river deltas should also be taken into account. Most estimates of 20th century sea level rise specifically exclude records that may be disturbed by earth-quakes.

In Jevrejeva *et al.* (2005) we show a link between AO and European sea level, which is best explained by a redistribution of water driven by shifts in surface air pressure. There is no trend in SLP as the atmosphere is essentially conservative, but there are significant differences on decadal time scales between SLP at different positions on the earth's surface – primarily as a result of long period fluctuations in large scale atmospheric pressure systems like the El Niño-Southern Oscillation (ENSO) or Arctic Oscillation (AO). These can produce decadal signals amounting to 30% of the variance in regional tide gauge records (Jevrejeva *et al.* 2005). We may reduce the signal caused by air pressure anomalies from the tide gauge records prior to a reconstruction of GSL with an inverse barometer correction (e.g. Grinsted *et al.* 2006b[IV]).

There is no common reference level for the RLR records. The tide gauge records can therefore not simply be averaged, unless they span the same period. However, the trends for different records can directly be compared. E.g. Douglas (1997) calculated the linear trend of 24 RLR records from sites with small GIA corrections, and found trends of 1.8 ± 0.1 mm/yr. Another approach, which we have found useful, is to average the annual sea level rate of many records and then integrate this to get an average GSL curve.

3 Glaciological modelling

3.1 Ice core proxies

Glaciers and ice sheets form where the amount of snow which falls each year exceeds the amount which is lost through melt. As layer upon layer of snow accumulates, ancient snow gets buried. Hence, glaciers and ice sheets can be regarded as atmospheric sediment. Mixed within the snow there will be small amounts of impurities such as e.g. atmospheric aerosol, volcanic ash, and wind-blown soil dust. The snow layers are gradually transformed into solid ice as the load of the snow above increases and within it small pockets of air containing samples of the atmosphere at the time will be trapped. Deeper the ice layers will be getting thinner and spreading out as the load increases further. The ice flows under influence of gravity from the accumulation area to the area where there is net loss of ice (the ablation area) due to e.g. melting and calving of ice bergs.

Ice cores drilled in a glacier or an ice cap will contain progressively older layers of ice with depth. The deep ice cores from the ice sheets in Greenland and Antarctica can span hundreds of thousands of years, but the smaller ice caps of the Arctic mostly contain only Holocene ice and typically records span a few hundred years (Koerner 1997, Delmas 1992, Wolff 1990). The past precipitation preserved in the ice core holds many potential proxies of climate. One of the most well known is $\delta^{18}O$ which is the relative deviation of the isotopic ratio $^{18}O/^{16}O$ from the ratio in standard sea water (Dansgaard 1964). Water molecules containing the heavy isotope of oxygen (^{18}O) have a lower vapor pressure than those containing the light (^{18}O). This leads to a fractionation causing a change in $\delta^{18}O$ during evaporation and condensation. The realization that $\delta^{18}O$ in precipitation was a proxy for temperature spawned the first ice core drilling for paleoclimate purposes at Camp Century, Northwest Greenland (Dansgaard *et al.* 1969). Since then, $\delta^{18}O$ in precipitation has become a generally accepted proxy for condensation temperature in the atmosphere and is related to the surface temperature in modern snow (van Lipzig *et al.* 2002). However, the relationship between $\delta^{18}O$ and surface temperature changes under different climate regimes as it also is affected by changes in e.g. moisture source temperature, seasonality of precipitation and moisture transport path (Paterson 1994).

It is necessary to know the age of the ice layers in an ice core in order for it to be a useful record of past climate. In some cores the seasonal signal in $\delta^{18}O$ is well preserved and we can count the annual layers and in this way date the ice. However, often the seasonal signal is not very clear due to diffusion, low accumulation or percolating melt water. In these cases, we can model the thinning of the ice with depth and in this way obtain a modeled dating (Paterson 1994). The model can be constrained by dating horizons where we know the ice to be a certain age. E.g. the snow from 1963 has elevated levels of radioactivity due to atmospheric nuclear test carried out in preceding years.

The impurities in ice have many different sources which generally fall into these groups: marine, terrestrial, anthropogenic, biogenic, and volcanic. Ions are among the most commonly studied constituents in ice as they contain clues on the source of the air at the drill site. Some sources lead to very specific ion signatures. E.g. The only known source of methanesulfonate (MSA) is from di-methyl sulphate (DMS) emissions due to oceanic biogenic activity (Legrand & Mayewski 1997).

The air bubbles trapped in the ice allow us to measure past concentrations of atmospheric gases. Of particular interest are past concentrations of greenhouse gases such as carbon dioxide and methane. Using this method it has been found that post industrial levels of CO_2 and CH_4 are roughly 30% and 130% higher respectively than at any other time during the last 650000 years (Siegentaler *et al.* 2005, Spahni *et al.* 2005). One practical difficulty with the use of records extracted from the trapped gases is that the gases will be slightly younger than the surrounding ice. This is because the snow is permeable and the gases are ventilated until the ice becomes so dense that the pores within the firn close-off. The pore close-off age will vary from site to site due to differences in e.g. accumulation rate and temperature.

The seasonal difference between summer and winter is of broad environmental significance. Continental interiors have larger seasonal temperature variations than maritime areas and the annual temperature range is often used as a measure of continentality. Ice cores from the interiors of large ice sheets such as Greenland or Antarctica are probably not very sensitive to the location of the sea ice margin – which determines the distance to open water and hence influences continentality – as it is far away from the drilling site. However, an ice core from an island near the seasonal sea ice margin may reflect the much larger relative variations in distance to open water via a continentality index. In ice cores where the seasonal cycle in $\delta^{18}O$ is well preserved the amplitude is an obvious candidate as a proxy for continentality. Unfortunately the oxygen isotope record is often affected by diffusion on a scale comparable to the annual layer thickness.

Almost all ice cores in the Arctic outside of Greenland are influenced by seasonal melt. Melt water can refreeze on the surface, percolate into deeper layers or run off. If melt water refreezes in the surface layers then it has little impact on average ion concentrations and $\delta^{18}O$ values. Percolation and run off affects ions much more strongly than isotopes because most ions have a very strong affinity for the water phase and even small amounts of melt water will have high concentrations of ions (Davies *et al.* 1982). Percolation however only redistributes the ions in the snow pack whereas they are lost by run-off. Iizuka *et al.* (2002) used the preferential removal of ions from particular layers as an indicator for seasonal melt on Austfonna, Svalbard, and found empirically that the magnesium sodium ratio was the best melt proxy.

3.1.1 Svalbard

Svalbard is surrounded by the Arctic Ocean, Barents Sea and North Atlantic. It is located near the overturning point of the North Atlantic thermohaline circulation, a key component in the climate system (Broecker 1991). The thermohaline circulation brings warm waters from the south to the Arctic and is responsible for the relatively mild climate of the Svalbard archipelago considering its northern position. Svalbard is located at the southerly edge of the permanent Arctic sea ice and has open ocean to its west even during winter. Glaciers cover 60% of Svalbard and most of the glaciers in Svalbard are polythermal (a layer of cold-ice on top of the temperate ice layer), (Pälli 2003). Relatively little is known about the regional climatic conditions prior to 1911. However, records of Barents Sea ice extent since 1864 have been compiled from ship logbooks (Vinje 2001). The most prominent pattern is a decreasing trend in ice extent throughout the record.

Several ice cores have been drilled on Svalbard ice fields producing records less than 1000 years long. Groups from the former Soviet Union drilled two ice cores on Lomonosovfonna in 1976 (Gordiyenko *et al.* 1981, Vaikmaë 1990) and in 1982 (Zagorodnov *et al.* 1984) and five ice cores from other sites around Svalbard between 1975 and 1987 (Punning *et al.* 1980, Zagorodnov & Zotikov 1981, Vaikmaë *et al.* 1984, Kotlyakov 1985, Punning *et al.* 1985, Punning & Tyugu 1991, Tarussov 1992). The Japanese have also drilled several ice cores at other sites in Svalbard since 1987, (e.g., Goto-Azuma *et al.* 1995, Watanabe *et al.* 2001, Matoba *et al.* 2002). However, only a few of these cores have been studied in detail. The best studied core from Svalbard is the 1997 Lomonosovfonna core drilled and analyzed by a joint Dutch-Finnish-Norwegian-Swedish group (Isaksson *et al.* 2001).

3.1.2 The Lomonosovfonna 1997 ice core

In 1997 a 121 m long ice core was drilled (spanning about 800 years) on Lomonosovfonna (Isaksson *et al.* 2001), the highest ice field in Svalbard (78°51'53"N, 17°25'30"E, 1255 m a.s.l.). The site was chosen as published data from a previous, lower-elevation ice core on Lomonosovfonna drilled in 1976 indicated better preserved stratigraphy than from other sites on Svalbard (Gordiyenko *et al.* 1981). Total ice depth from radar sounding was 123 m, and the site is close to the highest point of the ice cap with roughly radial ice flow. Dating of the core was based on a layer thinning model tied with the known dates of prominent reference horizons (see Kekonen *et al.* 2005a for details).

Studies so far indicate that the Lomonosovfonna ice core, despite seasonal melt, contains a reliable record of isotope and chemical concentrations that can be successfully used in climate and environmental studies (e.g., Moore *et al.* 2005a, Isaksson *et al.* 2001). The soluble ion chemical record (Cl^-, NO_3^-, SO_4^{2-}, $CH_3SO_3^-$, NH_4^+, K^+, Ca^{2+}, Mg^{2+}, Na^+) in the ice core spans the last 800 years (Kekonen *et al.* 2005a) and shows clearly defined changes corresponding with different climatic periods and anthropogenic pollution. Isaksson *et al.* (2001) and Kekonen *et al.* (2002) reported increases in sulphate and nitrate

in the mid twentieth century. Although local sources of pollution have to be taken into account (Simões & Zagorodnov 2001), there are also clear anthropogenic signals from long-range transport to the Lomonosovfonna ice cap (Kekonen *et al.* 2002), probably from both Eurasia and also from North America. Moore *et al.* (2006c[XIII]) made a sulphate inventory of the different sources of sulphate and found Western Europe to be the dominant anthropogenic source. Vehviläinen *et al.* (2002) found PAH compounds in the core and they concluded that these come from long-range sources. There is evidence that $\delta^{18}O$ is a good proxy for surface air temperature at the drill site: the rise in $\delta^{18}O$ from 1900 to 1920 that mirrors the rise in temperature seen in the instrumental record from Svalbard (Isaksson *et al.* 2003), consistency with the borehole temperature profile (van de Wal *et al.* 2002), and well preserved annual cycles (Pohjola *et al.* 2002b). Isaksson *et al.* (2003) suggested that the twentieth century was the warmest during the past 600 years based on $\delta^{18}O$ record from both the Lomonosovfonna and also the Austfonna ice cores. O'Dwyer *et al.* (2000) discussed methanesulfonic acid variations in terms of Barents Sea conditions. The annual accumulation has been calculated back to 1715A.D. by Pohjola *et al.* (2002b). The borehole temperature profile is modeled by Van de Wal *et al.* (2002) and shows that the nineteenth century was about 2°–3°C cooler than the twentieth century. Melting in the Lomonosovfonna ice core was studied in detail by Pohjola *et al.* (2002a) and showed that nitrate and sulphate are most easily percolated, while ammonium and oxygen isotopes are virtually unaffected. About 80% of calcium in the core is of non sea salt origin, and its covariation with sulphur has been interpreted in terms of a terrestrial source by Kekonen *et al.* (2005a). The clear volcanic peak following the 1783 Laki eruption was discussed in detail in Kekonen *et al.* (2005b).

3.2 Ice flow modelling

The modelling of ice flow can be used for many different purposes. Flow models may be used to study the response of glaciers and ice sheets to changes in e.g. mass balance or temperature (e.g. Näslund *et al.* 2000). In the context of ice cores, flow models are generally used to derive the relationship between age and depth (e.g. Dansgaard & Johnsen 1969). In some cases we may have observational data that severely constrains the output of the flow model. In these cases we can use inversion methods to infer what the model parameters and forcings must have been. E.g. we may have observed record of glacier length fluctuations. This approach has been successfully applied to infer the geothermal heat flux and past mass balance from ice core dating horizons (Grinsted & Dahl-Jensen 2002).

Simple flow models based on the continuity equation with few internal degrees of freedom (e.g. Dansgaard & Johnsen 1969) are generally the preferred method for obtaining age-depth relationships. Ice has a highly non-linear flow law where the effective viscosity is dependent on local stresses, temperature, water content, impurities, grain size, and ice fabric. For these reasons the physics of the ice mass are generally greatly simplified in numerical simulations. A summary of various models of varying complexity can be found in Pattyn (2002). In recent years there has been some progress towards solving the full stokes equations of the flow (Le Meur *et al.* 2006), even

including ice fabric development (Gillet-Chaulet *et al.* 2004). However, most modelling approaches need information on all the factors influencing the effective viscosity. Usually this is parameterized through flow law parameters such as the so-called 'flow exponent', 'enhancement factor', and temperature dependent ice rheological parameters (Paterson 1994). These parameters are generally only valid for a particular flow regime and are specific to the area of interest (Paterson 1994).

3.2.1 Antarctic blue ice areas

Blue ice areas (BIAs) are characterized by having exposed ice at the surface due to a negative surface mass balance. Of special interest, are blue ice areas where very localized conditions lead to islands of ablation surrounded by accumulation areas (Bintanja 1999). Many Antarctic BIAs are important stranding surfaces for large numbers of meteorites (Whillans & Cassidy 1983). The age of the surface ice has been determined by radiogenic and meteorite exposure dating to be typically between 10 thousand to 200 thousand years, though some meteorites have terrestrial ages of more than 2 million years (Bintanja 1999, Harvey *et al.* 1998). In high altitude BIAs melting does not occur and the areas should contain ancient ice at the surface in essentially pristine state. The flow of ice leads under steady state conditions to a continuous progression of isochrones on the surface (see Fig. 7), and we can take a 'horizontal ice core' directly from the surface. This valuable source of paleoclimatic data has largely not been utilized to date, largely because of difficulties in dating the ice. Most BIAs are found in the proximity of mountain ranges and nunataks which complicate flow modelling considerably (Bintanja 1999).

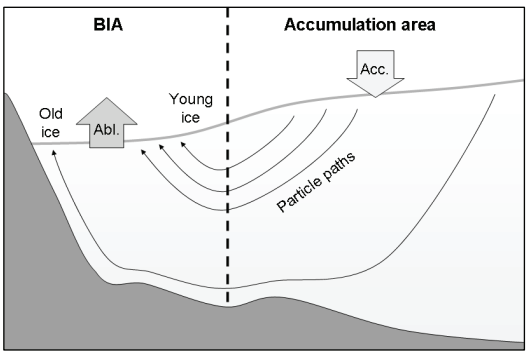

Fig. 7. Schematic of a blue ice area. Dashed line show the equilibrium line.

Naruse & Hashimoto (1982) used a simple flow model based on the continuity equation (Nye 1952) to date the Yamato Mountains BIA. Internal flow velocities are calculated from estimates of surface velocities, mass balance, and ice thickness. This type of model has proved to be very useful in dating vertical ice cores. However, Azuma *et al.* (1985) argue that the assumptions in this model are unrealistic in mountainous regions, and refine the model to take horizontal divergence into account. Surface velocities are inferred from continuity considerations and the fact that the horizontal velocity must be

zero where the ice meets the mountains (similarly to the model by Whillans & Cassidy 1983).

4 Objectives of the thesis

Glaciological research in the Arctic Centre focuses on ice cores, Antarctic blue ice areas, sea level, and large scale climate variability. The work in this thesis touches upon all of these subjects and is thus broad in scope. However, my own contribution is clearly defined as the collaborators either are chemists or geophysicists rather than modellers. The main aims of the thesis were:

1. to utilize the ancient ice in Antarctic BIAs for paleoclimatic reconstruction. The main obstacle is obtaining a reliable dating of the ice. In the present work a new ice flow model suitable for BIA dating is presented.
1. to make a new GSL reconstruction which is independent of recent satellite observations and assess the relative importance of mass and density contributions to sea level rise.
2. to extract environmental signals from the Lomonosovfonna ice core and assess whether the environmental signals in the ion records are preserved despite seasonal melt.
3. to examine large scale climatic links between the Tropics and the Arctic using advanced time series techniques.

5 Results

5.1 Dating Antarctic blue ice areas (Paper I)

We present a new simple flow model suitable for dating Antarctic BIAs (Grinsted *et al.* 2003[I]). Contrary to the models by Naruse & Hashimoto (1982) and Azuma *et al.* (1985) the new model is not based on the theoretical flow law for ice (Glen 1955), but rather an empirical fit to the horizontal velocity profile. The model has a single parameter that allows softening of ice with depth to be taken into account. The model is forced by observed surface velocities, mass balance, and ice thickness (similarly to Naruse & Hashimoto 1982). Any horizontal divergence is accounted for implicitly. The advantage of this model approach is that it is highly constrained by available observations. The model assumes steady state. However, as long as the geometry is constant we can prescribe a history of mass balance and surface velocity changes. This is possible because we calculate particle back trajectories which ensure that the absolute age is known as we follow a particle.

The model is applied to two very different BIAs which we characterize as 'closed type' and 'open type'. The 'closed' and 'open' refers to whether the flow is forced to terminate at a mountain or whether the flow continues through the BIA into another accumulation area. In the open type Allan Hills, Near Western Ice Field (77°S 159°E 2000 m asl), we can match the age inferred from meteorite finds by lowering both accumulation rates and surface velocities during the last glacial. The model has also been successfully applied on the largest BIA in Antarctica with flow lines as long as 200 km (Moore *et al.* 2006b).

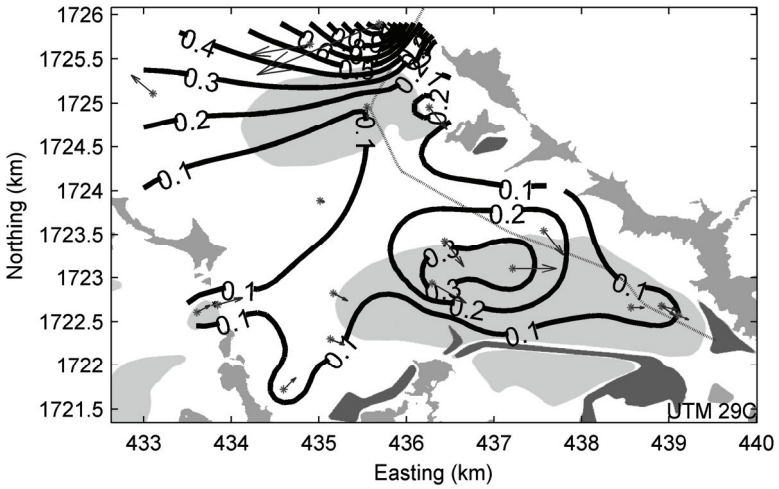

Fig. 8. Velocity map in Scharffenbergbotnen. Nunataks are marked in gray, moraines as dark gray, and blue ice as light gray. Stars with arrows show location of stakes and measured velocities. Contours show gridded surface velocities map based on the stake velocities (m/yr). Dotted line show the flow line used in the modeling.

The main BIA in Scharffenbergbotnen (74ºS, 11ºW, 1200 m asl) is a closed type Blue Ice Area as the flow is forced to terminate in the end of the valley (Grinsted *et al.* 2003[I]). In steady state ice flow is only just balanced by net ablation as there is no outflow from the valley. Hence, ice in the innermost part of the valley should be very old, analogous to the situation near the bed in a vertical ice core. The steady state scenario is modeled in Grinsted *et al.* (2003[I]) and show ages greater than 100,000 years. However, the ^{14}C dating of the SBB01 ice core from the innermost part of the main BIA indicate an age of only 10,500±600 years (van der Kemp *et al.* 2002), which is less than the time needed to travel along the surface from the equilibrium line using present day surface velocities (**Error! Reference source not found.**). Therefore, SBB can not have been in steady state throughout the Holocene. Here, I explore the possibility that SBB may have been an accumulation area during the Last Glacial Maximum (LGM) and the consequences for the dating. I assume that prior to 20 kyr BP the entire valley had an accumulation rate of 0.2 myr^{-1}. To balance this accumulation I assume a general outflow from the valley, with zero surface velocity in the innermost part of the valley (x=0 km) linearly increasing to 1 myr^{-1} at valley entrance (x=5 km). The mass balance and the surface velocity are prescribed to linearly change with time to match the present day observations. A comparison of the modelled surface ages with the ^{14}C ages is shown in Fig. 9. Based on this evidence alone it seems plausible that the BIA may have been smaller or even an accumulation area in the past. To examine the past flow regime under different conditions we plan to apply a full 3d thermo-mechanical finite element model of the area (as used by Le Meur *et al.* 2004).

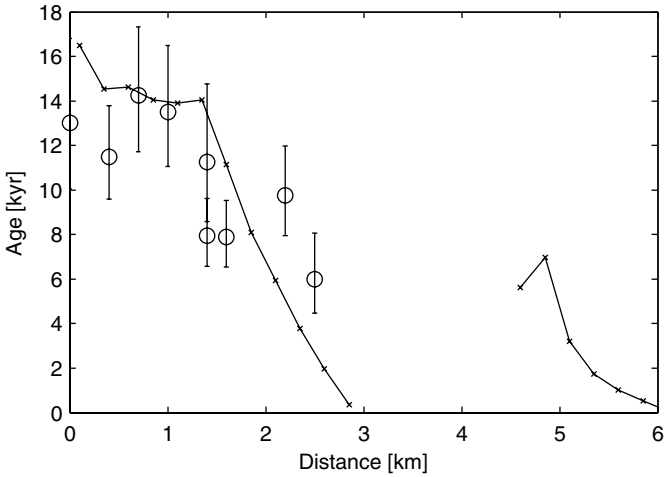

Fig. 9. Modeled surface age of Scharffenbergbotnen BIA along the flow line (see Error! Reference source not found.**) assuming that the area was an accumulation area in the past. Circles show ^{14}C ages (van Roijen 1996) with errorbars calculated from the distance to the flow line. These errors were estimated by plotting the relative difference between two ^{14}C ages against their distance and fitting a straight line.**

5.2 Wavelet coherence (Paper II, Paper VI)

In Grinsted *et al.* (2004[II]) we present the cross wavelet transform (XWT) and wavelet coherence (WTC) and show their application to geophysical time series. A Monte Carlo statistical significance test for WTC against red-noise has been developed. We find that the significance level for the WTC is largely independent of the noise colour, which may imply that a theoretical white noise test can be used. We further show how circular means and circular standard deviations can be used to quantify the relative phase relationship between the series. The methods are illustrated by the relationship between the AO and the BMI and we show that the BMI passively mirrors the atmospheric forcing (i.e. the AO).

To accompany the Grinsted *et al.* (2004[II]) paper, I have developed an open source wavelet coherence toolbox for Matlab, which is freely available on the web (http://www.pol.ac.uk/home/research/waveletcoherence/). We are actively maintaining this software package and also providing support for people using it.

The Quasi Biennial Oscillation (QBO) is a very regular oscillation in the stratosphere with a period of ~28 months. The QBO is conventionally defined as the zonal average of the 30mb zonal wind at the equator. The oscillation propagates to the entire planet with a 3 month lag between pole and equator (Baldwin *et al.* 2001). AO also has a significant spectral peak at roughly the same period and it has therefore been suggested that QBO drives AO on these wavelengths. In Moore *et al.* (2006a[VI]) we find virtually no wavelet coherence between QBO and AO which casts this hypothesis into doubt.

5.3 Lomonosovfonna Melt and Continentality (Paper III)

Chemical records from ice cores that suffer seasonal melting have a reputation of being poor sources of information for paleoclimate reconstructions, (Koerner 1997). However, advances in both analytical and mathematical techniques suggests that certain ice cores preserve reliable records, that can be extracted with confidence, at least on decadal scales (Goto-Azuma *et al.* 2002, Kekonen *et al.* 2005a, Pohjola *et al.* 2002a) – but doubts remain in their interpretation at higher resolution.

In Moore *et al.* (2005a) we show that the signals in Lomonosovfonna ion record are primarily of environmental origin and that the melt signal caused by melt is mainly explained by a shift in the mean concentrations. We compare ion composition between bubbly ice layers and clear ice (clear ice is indicative of refrozen melt water) using principal component analysis. Only the first principal component (PC) shows significant differences between the two groups. When we compare the ion composition between different climatic periods we find significant differences in the first 4 PCs.

Many studies have found that particular ions are preferentially washed out of the ice during seasonal melt (e.g. Davies *et al.* 1982, Iizuka *et al.* 2002). In Grinsted *et al.* (2006a[III]) we build a model for the chemical fractionation during melt. Based on this model we obtain a proxy for melt intensity based on the logarithmic ratio between two ions with the same principal source but different elution rates. We use two ion pairs (Na^+/Mg^{2+} and Cl^-/K^+) to obtain two independent melt proxies and show that their records agree qualitatively. In addition to summer temperature, the melt proxies also appears to reflect sea ice extent, likely as a result of sodium chloride fractionation in the oceanic sea ice margin source area that is dependent on winter temperatures.

The amplitude of the annual signal in $\delta^{18}O$ (*A*) is an obvious candidate for a continentality proxy, since $\delta^{18}O$ on Lomonosovfonna is a proxy for surface air temperature (Isaksson *et al.* 2001, van de Wal *et al.* 2002) and the annual cycle is well preserved (Pohjola *et al.* 2002b). However, melt and firn diffusion processes alter the deposited signal which complicates the interpretation of the amplitudes. With modelling and through correlations with instrumental temperature range we show that the amplitude record can be used as a continentality proxy provided that it is smoothed sufficiently (Grinsted *et al.* 2006a[III]).

The melt proxies, the $\delta^{18}O$, and the continentality proxy tell a consistent story of a colder and more continental climate with larger sea ice extent during the Little Ice Age in Svalbard (Grinsted *et al.* 2006a[III]). Perhaps the most surprising finding is that continentality decreased around 1870, 20–30 years before the rise in temperatures indicated by the $\delta^{18}O$ profile. The melt record indicates that summers were warmer in the Medieval Warm Period than during the 1990s – but maybe similar to post-2000 summers.

5.4 Sea level (Paper IV & VIII)

Producing a GSL curve with valid confidence intervals from the observational data base is not a trivial job. We have developed a new ‘virtual station’ method to overcome geographical bias, so that stations close to each other are weighted much less than

isolated ones, and which can quantify the uncertainties due to the representativeness of the stations used (Jevrejeva *et al.* 2006, Grinsted *et al.* 2006b[IV]).

As there is no common reference level for the tide gauge data, we examine the rate of change in sea level rather than sea level itself. Our approach for creating a GSL curve is therefore to integrate the rate of change in GSL (dGSL), which we obtain by making a geographically weighted average (see below) of the sea level rates from individual tide gauge stations. Prior to analysis modelled GIA corrections were applied to the tide gauge records.

We assign each station to one of 13 regions. We then recursively collapse the two closest stations within a region (by averaging their records) into a new virtual station half-way between them until only one station remains. This last remaining virtual station represents the average for the entire region. This ensures that isolated tide gauge records are given more weight. Whenever a virtual station is created the uncertainty due representativity can be calculated by looking at the deviation from the mean of the source stations over the period of common overlap (Jevrejeva *et al.* 2006). Finally, the GSL is calculated as the integrated average of the regional sea level rates excluding the Baltic region (Fig. 10).

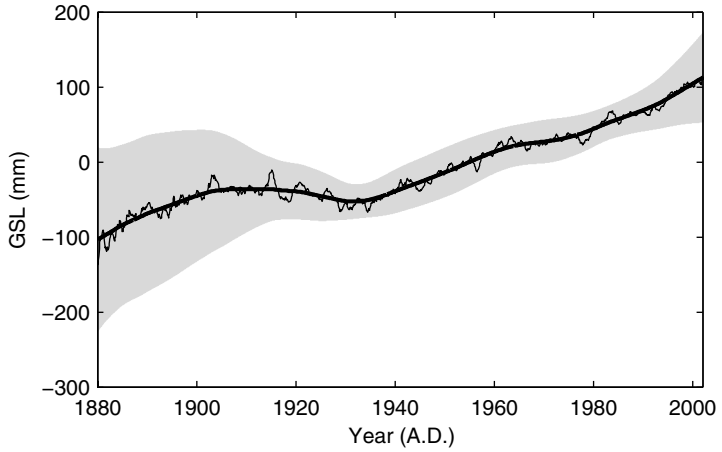

Fig. 10. Global sea level relative to the 20th century mean, calculated using the virtual station method (thin solid line) and its SSA non-linear trend with 10 year lag (thick line). Grey band shows the 95% confidence interval of the trend (a jack-knife estimate).

It has previously been noted that there are drops in global sea level (GSL) following some major volcanic eruptions (Church *et al.* 2004, Church & White 2006). However, observational evidence has not been convincing as there is substantial variability in the global sea level record on periods similar to those at which we expect volcanoes to have an impact (Jevrejeva *et al.* 2005). In Grinsted *et al.* (2006b[IV]) we quantify the impact of volcanic eruptions by averaging the virtual station GSL around 5 major volcanic eruptions. Surprisingly, we find that the initial response to a volcanic eruption is a significant rise in sea level of 9 mm in the first year after the eruption. This is followed by a drop of 7 mm in the period 2-3 years after the eruption relative to pre-eruption sea level.

Neither the drop nor especially the rise in GSL can be explained by models of lower oceanic heat content (Hansen *et al.* 2002, Church *et al.* 2005). We suggest that the largest volcanic impact is a transient disturbance of the water cycle, comparable to the impact of a large El Niño-La Niña cycle, amounting to about 5% of global land precipitation.

5.5 Noise reduction in Ground Penetrating Radar (Paper V)

Ground Penetrating Radar (GPR) is a commonly used tool in glaciology. It is frequently used for finding the total ice thickness, the depth of the water table, and for following internal isochrones (e.g. Sinisalo *et al.* 2003). In glaciological research, there are frequently prohibitive logistical difficulties in returning to a particular glacier to collect additional data that may aid interpretation. Therefore it is worth going to more trouble than would be the case in a commercial survey, to extract the maximum glaciological information from existing radar data.

In Moore & Grinsted (2006^{V}) we apply SSA for noise reduction. We combine this noise reduction with an envelope detection scheme followed by horizontal stacking of the radar traces. Our methods show a dramatic improvement in visual quality of a low signal to noise ratio GPR data set compared with traditional methods.

5.6 ENSO-Arctic links (Paper VII)

Jevrejeva *et al.* (2003) found what appeared to be a common ~14 year signal in both the AO and the SOI using singular spectrum analysis. In Jevrejeva *et al.* (2004^{VI}) we isolate the 14 year signal from 4 different Arctic series and 4 different ENSO series, and they all appear to be phase locked. We find that SOI is leading the Arctic series by roughly 2 years. This result is confirmed by wavelet coherence.

We develop a new method to track how the 14 year signal isolated from SOI propagates around the world in gridded sea surface temperatures. The phase coherence and the average relative phase between SST in a grid cell and the isolated signal are calculated. In this way we plot regions of significant coherence and the relative lag within these regions. The observed pattern in coherence and phase lags can be explained by equatorial coupled wave propagation in the Pacific Ocean followed by Kelvin boundary wave propagation along the western margins of the Americas and by poleward-propagation of atmospheric angular momentum (Jevrejeva *et al.* 2004^{VI}). The method of mapping the phase coherence and mean relative phase can be considered a 'phase-aware teleconnection' pattern.

5.7 Sunspots and climate (Paper VI)

There is considerable dispute as to the strength of the sun-climate link (Tsiropoula 2003, Laut 2003). Many proxy climatic time series exhibit significant power in the 11-14 year

band, which several authors have been tempted to ascribe to solar sunspot cycles (e.g. Rigozo *et al.* 2002).

In Moore *et al.* (2006a) we examine the plausibility of the argument that solar cycles are significant factors in climate on multi-year and decadal timescales. The lagged phase coherence between sunspot numbers and major climate indices (SOI, Niño3.4, and AO) at the 11 year period shows no signs of sunspots being a driving mechanism. We therefore conclude that there is no simple causative relationship between sunspot numbers (and hence solar insolation) and multi-year to decadal signals in the large circulation patterns that define in large planet's climate. In Fig. 11 the phase-aware teleconnection pattern between sunspot numbers and global SST is shown. The lack of coherence and random phase orientations confirm the results of Moore *et al.* (2006a[VI]).

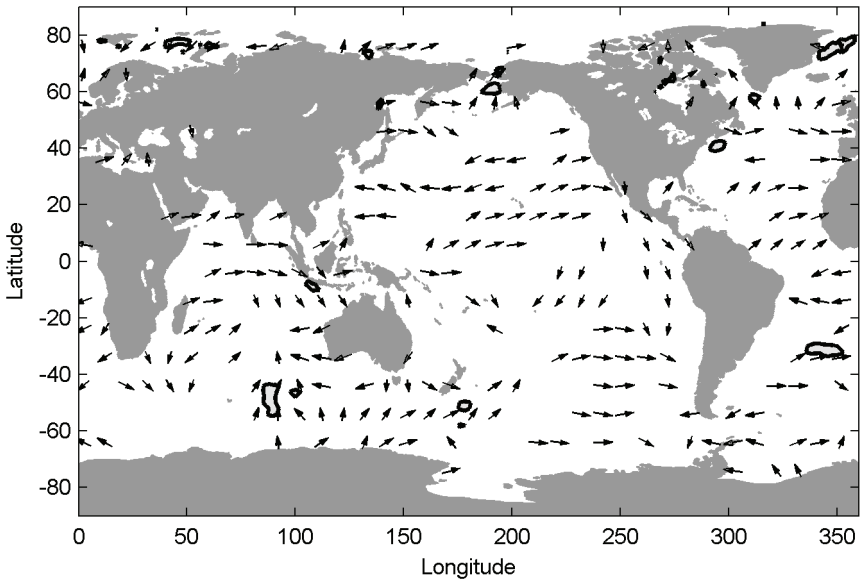

Fig. 11. Lack of pattern in phase-aware teleconnection between SST (Smith & Reynolds 2004) and sunspot numbers over the 20th century using a Paul wavelet with 11 year centre periodicity. Regions of significant coherence are shown with a thick black contour and light grey shading. Arrows indicate the average phase relationship (pointing right: in-phase; left: anti-phase; down: sunspots lagging by 90°). For clarity phase arrows are not plotted where the phase coherence is below 0.2.

References

ACIA (2004) Arctic Climate Impact Assessment (ACIA), 2004. Impacts of a Warming Arctic.

Allan RJ & Ansell TJ (2006) A new globally complete monthly historical mean sea level pressure data set (HadSLP2) 1850-2004. J Clim (Accepted).

Allen MR & Smith LA (1996) Monte Carlo SSA: Detecting irregular oscillations in the presence of coloured noise. J Clim 9: 3373–3404.

Angström A (1935) Teleconnections of climate changes in present time. Geografiska Annaler 17: 242-258.

Azuma M, Nakawo N, Higashi A& Nishio F (1985) Flow pattern near Massif A in the Yamato bare ice field estimated from the structures and the mechanical properties of a shallow ice core. Mem NIPR Spec Iss 39: 173-183.

Baldwin MP, Gray LJ, Dunkerton TJ, Hamilton K, Haynes PH, Randel WJ, Holton JR, Alexander MJ, Hirota I, Horinouchi T, Jones DBA, Kinnerslay JS, Marquardt C, Sato K & Tarahashi M (2001) The Quasi-Biennial Oscillation. Rev Geophys 39: 170-229.

Battisti & Sarachik (1995) Understanding and predicting ENSO. Rev Geophys 33: 1367-76.

Bintanja R (1999) On the glaciological, meteorological, and climatological significance of Antarctic blue ice areas. Rev Geophys 37: 337-359.

Bjerknes J (1969) Atmospheric teleconnections from the equatorial Pacific. Mon Wea Rev 97: 163-172.

Björnsson & Venegas (1997) A Manual for EOF and SVD Analyses of Climatic Data. CCGCR Report 97-1.

Bolzan JF & Pohjola VA (2000) Reconstruction of the undiffused seasonal oxygen isotope signal in central Greenland ice cores. J Geophys Res 105(C9): 22095-22106. doi: 10.1029/2000JC000258.

Box JE, Bromwich DH & Bai L (2004) Greenland ice sheet surface mass balance 1991 – 2000: Application of Polar MM5 mesoscale model and in situ data. J Geophys Res 109: D16105. doi: 10.1029/2003JD004451.

Broecker WS (1991) The great ocean conveyor. Oceanography 4(2): 79-89.

Church JA, White NJ, Coleman R, Lambeck K & Mitrovica JX (2004) Estimates of the regional distribution of sea-level rise over the 1950 to 2000 period. J Clim 17: 2609–2625.

Church JA, White NJ & Arblaster JM (2005) Significant decadal-scale impact of volcanic eruptions on sea level and ocean heat content. Nature 438. doi: 10.1038.nature04237.

Church JA & White NJ (2006) A 20th century acceleration in global sea-level rise. Geophys Res Lett 33: L01602. doi: 10.1029/2005GL024826.

Clarke AJ, Wang J & Van Gorder (2000) A simple warm-pool displacement ENSO model. J Phys Oceanogr 30: 1679-1691. Corrigendum JPO 30: 3271.

Crantz D (1765) The history of Greenland: including an Account of the Mission Carried on by the United Brethren in that Country, 2 volumes, xi, 359 pp, vi, 323 pp., Longman, Hurst, Rees, Orme and Brown, 1820, London.

Cullen N & Steffen K (2001) Unstable near-surface boundary conditions in summer on top of the Greenland ice sheet. Geophys Res Lett 28(23): 4491-4494.

Dansgaard W (1964) Stable isotopes in precipitation. Tellus 16: 436-468.

Dansgaard W & Johnsen SJ (1969) A flow model and a timescale for the ice core from Camp Century, Greenland. J Glaciol 8(53): 215-223.

Delmas R (1992) Environmental information from ice cores. Rev Geophys 30: 1-21.

Domine F, Sparapani R, Ianniello A & Beine HJ (2004) The origin of sea salt in snow on Arctic sea ice and in coastal regions. Atmos Chem Phys 4: 2259–2271.

Douglas BC (1995) Global Sea Level Change: Determination and Interpretation. Rev Geophys (Supplement): 1425-1432.

Douglas BC (1997) Global Sea Rise: A Redetermination. Surveys in Geophysics 18(2): 279-292.

Foufoula-Georgiou E & Kumar P (eds) (1995) Wavelets in Geophysics. Academic Press: 373.

Gershenfeld N (1999) The nature of mathematical modelling. Cambridge University Press, New York, NY.

Ghil M *et al.* (2002) Advanced spectral methods for climatic time series. Rev Geophys 40(1): 1003. doi: 10.1029/2000RG000092.

Gillet-Chaulet F, Gagliardini O, Meyssonnier J, Zwinger / & Ruokolainen J (2006) Flow-induced anisotropy in polar ice and related ice-sheet flow modelling. J Non-Newtonian Fluid Mech 134: 33-43.

Glen JW (1955) The creep of polycrystalline ice. Proceeding of the Royal Society A228: 513-38.

Gordiyenko FG, Kotlyakov VM, Punning Y-KM & Vaikmaë R (1981) Study of a 200-m core from the Lomonosov ice plateau on Spitsbergen and the paleoclimatic implications. Polar Geogr Geol 5(4): 242–251.

Goto-Azuma K, Kohshima S, Kameda T, Takahashi S, Watanabe O, Fujii Y & Hagen J (1995) An ice-core chemistry record from Snøfjellafonna, northwestern Spitsbergen. Ann Glaciol 21: 213-218.

Goto-Azuma K, Koerner RM & Fisher DA (2002) An ice-core record over the last two centuries from Penny Ice Cap, Baffin Island, Canada. Ann Glaciol 35: 29– 35.

Grinsted A & Dahl-Jensen D (2002) A Monte Carlo-tuned model of the flow in the NorthGRIP area. Ann Glaciol 35: 527-530.

Grinsted A, Moore J, Spikes VB & Sinisalo A (2003) Dating Antarctic blue ice areas using a novel ice flow model. Geophys Res Lett 30(19). doi: 10.1029/2003GL017957.

Grinsted A, Moore JC & Jevrejeva S (2004) Application of the cross wavelet transform and wavelet coherence to geophysical time series. Nonlin Process Geophys 11: 561-566. (http://www.pol.ac.uk/home/research/waveletcoherence/)

Grinsted A, Moore JC, Pohjola V, Martma T & Isaksson E (2006a), Svalbard summer melting, continentality, and sea ice extent from the Lomonosovfonna ice core. J Geophys Res 111: D07110. doi: 10.1029/2005JD006494.

Grinsted A., Moore JC & Jevrejeva S (2006b) Observational evidence for volcanic impact on sea level and the global water cycle. (Manuscript in review)

Dansgaard W, Johnsen SJ, Moller J &Langway CC Jr (1969) One thousand centuries of climatic record from Camp Century on the Greenland ice sheet. Science 166: 377-381

Harvey RP, Dunbar NW, Macintosh WC, Esser RP, Nishiizumi K, Taylor S & Caffee MW (1998) Meteoric event recorded in Antarctic ice. Geology 26(7): 607--610.

Herzfeld UC & Holmlund P (1990) Geostatistics in glaciology: Implications of a study of SBB, Dronning Maud Land, East Antarctic. Ann Glaciol 14: 107-110.

Hilborn Robert C (2000) Chaos and Nonlinear Dynamics, Oxford University Press. 2nd ed.

Hotelling H (1933) Analysis of a complex of statistical variables into principal components. J Educ Psych 24: 417-520.

Iizuka Y, Igarashi M, Kamiyama K, Motoyama H & Watanabe O (2002) Ratios of Mg2+/Na+ in snowpack and an ice core at Austfonna ice cap, Svalbard, as an indicator of seasonal melting. J Glaciol 48(162): 452–460.

IPCC (2001a) Climate Change 2001: The Scientific Basis. A Contribution of Working Group I to the Third Assessment Report of the Intergovernmental Panel on Climate Change. [Houghton JT, Ding Y, Griggs DJ, Noguer M, van der Linden PJ, Dai X, Maskell K & Johnson CA (eds)] Cambridge University Press, Cambridge, United Kingdom and New York, NY, USA.

IPCC (2001b) Climate Change 2001: Impacts, Adaptation, and Vulnerability: Contribution of Working Group II to the Third Assessment Report of the Intergovernmental Panel on Climate Change. [McCarthy JJ, Canziani OF, Leary NA, Dokken DJ &White KS (eds)] Cambridge University Press, Cambridge, United Kingdom and New York, NY, USA.

Isaksson E, Pohjola V, Jauhiainen T, Moore J, Pinglot J-F, Vaikmäe R, van de Wal RSW, Hagen J-O, Ivask J, Karlöf L, Martma T, Meijer HAJ, Mulvaney R, Thomassen MPA & Van den Broeke M (2001) A new ice core record from Lomonosovfonna, Svalbard: viewing the data between 1920-1997 in relation to present climate and environmental conditions. J Glaciol 47(157): 335-345.

Isaksson E, Hermanson M, Hicks S, Igarashi M, Kamiyama K, Moore JC, Motoyama H, Muir D, Pohjola V, Vaikmäe R, van de Wal RSW & Watanabe O (2003) Ice cores from Svalbard – Useful archives of past climate and pollution history. Phys Chem Earth 28: 1217-1228.

Jevrejeva S & Moore JC (2001) Singular Spectrum Analysis of Baltic Sea ice conditions and large-scale atmospheric patterns since 1708. Geophys Res Lett 28: 4503-4506.

Jevrejeva S (2002) Association between the ice conditions in the Baltic Sea and the North Atlantic Oscillation. Nordic Hydrol 33: 319-330.

Jevrejeva S, Moore JC & Grinsted A (2003) Influence of the Arctic Oscillation and El Niño-Southern Oscillation (ENSO) on ice conditions in the Baltic Sea: The wavelet approach. J Geophys Res 108(D21): 4677. doi: 10.1029/2003JD003417.

Jevrejeva S, Moore JC & Grinsted A (2004) Oceanic and atmospheric transport of multi-year ENSO signatures to the polar regions. Geophys Res Lett 31: L24210. doi: 10.1029/2004GL020871

Jevrejeva S, Moore JC, Woodworth PL & Grinsted A (2005) Influence of large-scale atmospheric circulation on European sea level: results based on the wavelet transform method. Tellus 57A: 183–193.

Jevrejeva S, Grinsted A, Moore JC & Holgate S (2006) Nonlinear trends and multiyear cycles in sea level records. J Geophys Res 111: C09012. doi: 10.1029/2005JC003229.

Johnsen SJ, Clausen H, Cuffey K, Hoffmann G, Schwander J & Creyts T (2000) Diffusion of stable isotopes in polar firn and ice: the isotope effect in firn diffusion. Physics of Ice Core Records, Sapporo, Hokkaido University Press: 121-140.

Jones PD & Mann ME (2004) Climate over past millennia. Rev Geophys 42: RG2002. doi: 10.1029/2003RG000143.

Kantz H & Schreiber T (2004) Nonlinear Time Series Analysis. Cambridge University Press, Cambridge, 2nd ed.

Kekonen, T, Moore J, Mulvaney R, Isaksson E, Pohjola V & van de Wal RSW (2002) An 800 year record of nitrate from the Lomonosovfonna ice core, Svalbard. Ann Glaciol 35: 261-265.

Kekonen T, Moore J, Perämäki P, Mulvaney R, Isaksson E, Pohjola V & van de Wal RSW (2005a) The 800 year long ion record from the Lomonosovfonna (Svalbard) ice core. J Geophys Res 110: D07304. doi: 10.1029/2004JD005223.

Kekonen T, Moore JC, Perämäki P & Martma T (2005b) The Icelandic Laki volcanic tephra layer in the Lomonosovfonna ice core, Svalbard. Polar Research 24(1-2): 33-40.

Koerner RM (1997) Some comments on climatic reconstructions from ice cores drilled in areas of high melt. J Glaciol 43(143): 90-97. (Erratum: 43(144): 375-376.)

Kotlyakov VM (1985) Glyatsiologiya Shpitsbergena (Glaciology of Spitsbergen). Nauka, Moscow.

Koutsoyiannis D (2005) Uncertainty, entropy, scaling and hydrological stochastics, 1, Marginal distributional properties of hydrological processes and state scaling. Hydrological Sciences Journal 50(3): 381-404.

Krabill W *et al.* (2004) Greenland Ice Sheet: Increased coastal thinning. Geophys Res Lett 31: L24402. doi: 10.1029/2004GL021533.

Laut P (2003) Solar activity and terrestrial climate: an analysis of some purported correlations. J Atmos Sol Terr Phys 65: 801– 812.

Legrand M & Mayewski P (1997) Glaciochemistry of polar ice cores: a review. Rev Geophys 35: 219-243.

Le Meur E, Gagliardini O, Zwinger T, Ruokolainen J (2004) Glacier flow modelling: a comparison of the Shallow Ice Approximation and the full-Stokes equation. C R Physique 5: 709-722.

Loewe P & Koslowski G (1998) The Western Baltic Sea ice season in terms of a mass-related severity index 1879-1992, II Spectral characteristics and associations with NAO, QBO and solar cycle. Tellus 50A: 219-241.

Lorentz EN (1956) Empirical orthogonal function and statistical weather prediction, Science Report 1. Statistical Forecast Project, Department of meteorology, MIT (NTIS AD 110268).

Lorenz EN (1963) Deterministic non-periodic flow. J Atmos Sci 20: 130-141.

Mann ME (2004) On smoothing potentially nonstationary climate time series. Geophys Res Lett 31: L07214. doi: 10.1029/2004GL019569.

Maraun D & Kurths J (2004) Cross Wavelet Analysis. Significance Testing and Pitfalls. Nonlin Proc Geoph 11(4): 505-514.

Matoba S, Narita H, Motoyama H, Kamiyama K & Watanabe O (2002) Ice core chemistry of Vestfonna Ice Cap in Svalbard, Norway. J Geophys Res 107: 4721-4727.

Moberg A *et al.* (2005) Highly variable Northern Hemisphere temperatures reconstructed from low- and high-resolution proxy data. Nature 433: 613-617.

Moore JC, Grinsted A, Kekonen T & Pohjola V (2005a) Separation of melting and environmental signals in an ice core with seasonal melt. Geophys Res Lett 32: L10501. doi: 10.1029/2005GL023039.

Moore JC, Grinsted A, Jevrejeva S (2005b) New Tools for Analyzing Time Series Relationships and Trends. EOS 86(24).

Moore & Grinsted (2006) Singular spectrum analysis and envelope detection: methods of enhancing the utility of ground penetrating radar data. J Glaciol 52(176): 159-163(5).

Moore J, Grinsted A & Jevrejeva S (2006a) Is there evidence for sunspot forcing of climate at multi-year and decadal periods? Geophys Res Lett 33: L17705. doi: 10.1029/2006GL026501.

Moore JC, Nishio F, Fujita S, Narita H, Pasteur E, Grinsted A, Sinisalo A& Maeno N (2006b) Interpreting ancient ice in a shallow ice core from the South Yamato (Antarctica) blue ice area using flow modeling and compositional matching to deep ice cores. J Geophys Res 111. doi: 10.1029/2005JD006343.

Moore J, Kekonen T, Grinsted A & Isaksson E (2006c) Sulfate source inventories from a Svalbard ice core record spanning the Industrial Revolution. J Geophys Res 111: D15307. doi: 10.1029/2005JD006453.

Naruse R & Hashimoto M (1982) Internal flow lines in the ice sheet upstream of the Yamato Mountains, East Antarctica. Mem NIPR spec Iss 24: 201-203.

Näslund JO, Fastook JL & Holmlund P (2000) Numerical modelling of the ice sheet in western Dronning Maud Land, East Antarctica: impacts of present, past and future climates. J Glaciol 46: 54-66.

Omstedt A & Chen D (2001) Influence of atmospheric circulation on the maximum ice extent in the Baltic Sea. J Geophys Res 106: 4493-4500.

Paterson WSB (1994) The Physics of Glaciers. 3rd ed., Oxford, Elsevier.

Pattyn F (2002) Transient glacier response with a higher-order numerical ice-flow model. J Glaciol 48: 467-477.

Peltier WR (2001) Global glacial isostatic adjustment and modern instrumental records of relative sea level history. In: Douglas BC, Kearney MS & Leatherman SP (eds) Sea Level Rise. Academic Press.

Pfeffer WT & Humphrey NF (1998) Formation of ice layers by infiltration and refreezing of meltwater. Ann Glaciol 26: 83-91.

Pohjola VA, Moore JC, Isaksson E, Jauhiainen T, van de Wal RSW, Martma T, Meijer HAJ & Vaikmäe R (2002a) Effect of periodic melting on geochemical and isotopic signals in an ice core from Lomonosovfonna, Svalbard. J Geophys Res 107(D4): 4036. doi: 10.1029/2000JD000149.

Pohjola VA, Martma T, Meijer HAJ, Moore JC, Isaksson E, Vaikmäe R & van de Wal RSW (2002b) Reconstruction of 300 years annual accumulation rates based on the record of stable isotopes of water from Lomonosovfonna, Svalbard. Ann Glaciol 35: 57-62.

Punning Y-MK, Vaikmaë RA, Kotlyakov VM & Gordiyenko FG (1980) Izotopno-kislorodnyye issledovaniya kerna s ledorazdela lednikov Grënf'ord I Frit'of (o. Zapadnyy Shpisbergen (Isotope-oxygen investigations of ice core from the ice-divide of the Gronfjordbreen and Fridtjovbreen (Spitsbergen)). Mater Glyatsiol Issled 37: 173–177.

Punning Y-MK, Martma TA, Tyugu KE, Vaikmaë RA, Pourchet M & Pinglot F (1985) Stratifikatsiya lednikovogo kerna s Zapadnogo ledyanogo polya na Severo-Vostochnoy Zemle (Stratification of ice core from Vestfonna, Nordaustlandet). Mater Glyatsiol Issled 52: 202–205. (translation Polar Geogr. Geol., 10(1), 39–43, 1986.)

Punning Y-MK & Tyugu KR (1991) Raspredeleniya khimicheskikih elementov v lednikovykh kernakh s Severo-Vostochnoy Zemli (The distribution of chemical elements in the glacier cores from Nordaustlandet). Mater Glyatsiol Issled 72: 170– 176.

Pälli A (2003) Polythermal glacier studies in Svalbard determined by ground-penetrating radar. Ph.D. Thesis, University of Oulu, A 406.

Rigozo NR, Nordemann DJR, Echer E, Zanandrea A & Gonzalez WD (2002) Solar variability effects studied by tree-ring data wavelet analysis. Advances in Space Research 29: 1985-1988.

Ruelle D & Takens F (1971) On the nature of turbulence. Communications of Mathematical Physics 20: 167-192.

Saabye HE (1942) Brudstykker af en Dagbog holden i Grønland I Aarene 1770-1778, Medd Grønland. ed. Osterman H, pp. 45 and 103.

Seinä A, Grönvall H, Kalliosaari S & Vainio J (2001). Ice seasons 1996-2000 in Finnish sea areas / Jäätalvet 1996-2000 Suomen merialueilla, Meri, Report Series of the Finnish Institute of Marine Research, 43.

Siegenthaler U, Stocker TF, Monnin E, Luthi D, Schwander J, Stauffer B, Raynaud D, Barnola JM, Fischer H, Masson-Delmotte V, Jouzel J (2005) Stable Carbon Cycle–Climate Relationship During the Late Pleistocene. Science 310(5752): 1313-7.

Sinisalo A, Grinsted A, Moore JC, Kärkäs E Petterson R (2003) Snow accumulation studies in Antarctica with ground penetrating radar using 50, 100 and 800 MHz antenna frequencies. Annals of Glaciology 37: 194-198.

Sinisalo A, Grinsted A & Moore J (2004) Dynamics of the Scharffenbergbotnen blue-ice area, Dronning Maud Land, Antarctica. Ann Glaciol 39.

Smith TM & Reynolds RW (2004) Improved Extended Reconstruction of SST (1854-1997). J Clim 17: 2466-2477.

Spahni R, Chappellaz J, Stocker TF, Loulergue L, Hausammann G, Kawamura K, Fluckiger J, Schwander J, Raynaud D, Masson-Delmotte V & Jouzel J (2005) Atmospheric methane and nitrous oxide of the Late Pleistocene from Antarctic ice cores. Science 310(5752): 1317-21.

Sprott JC (2003) Chaos and Time-Series Analysis. Oxford University Press.

Stephenson DB, Wanner H, Bronnimann S & Luterbacher J (2003) The history of scientific research on the North Atlantic Oscillation. The North Atlantic Oscillation: Climatic Significance and Environmental Impact. Geophys Monogr 134: 37-50.

Takens F (1981) Detecting strange attractors in turbulence. In: Rand DA & Young L-S (eds) Lect. Not. in Math., vol. 898, Dynamical Systems and Turbulence, Springer-Verlag, New York: 366–381.

Tarussov A (1992) The Arctic from Svalbard to Severnaya Zemlya: Climatic reconstructions from ice cores. In: Bradley RS & Jones PD (eds)Climate Since A.D. 1500. Routledge, Boca Raton, Fla: 505–516.

Thompson DWJ & Wallace JM (1998) The Arctic Oscillation signature in the winter geopotential height and temperature fields. Geophys. Res Lett 25: 1297–1300.

Torrence & Compo (1998) A practical guide to wavelet analysis. Bull Am Meteorol Soc 79: 61-78.

Torrence C & Webster P (1999) Interdecadal Changes in the ESNO-Monsoon System. J Clim 12: 2679-2690.

Tsiropoula G (2003) Signatures of solar activity variability in meteorological parameters. J Atmos Sol Terr Phys 65: 469-482.

Vaikmäe R (1990) Isotope variations in the temperate glaciers of the Eurasian Arctic. Nuclear Geophys 4: 4-55.

van de Wal RSW, Mulvaney R, Isaksson E, Moore JC, Pinglot J-F, Pohjola V & Thomassen MPA (2002) Reconstruction of the historical temperature trend from measurements in a medium-length bore hole on the Lomonosovfonna Plateau, Svalbard. Ann Glaciol 35: 371-378.

van der Kemp W, Alderliesten C, van der Borg K, de Jong AFM, Lamers RAN, Oerlemans J, Thomassen M & van der Wal RSW (2002) In situ produced 14C by cosmic ray muons in ablating Antarctic ice. Tellus 45B: 186-192.

van Lipzig NPM, van Meijgaard E & Oerlemans J (2002) The effect of temporal variations in the surface mass balance and temperature-inversion strength on the interpretation of ice core signals. J Glaciol 48(163): 611-621.

van Roijen JJ (1996) Determination of ages and specific mass balances from 14C measurements on Antarctic surface ice. Ph.D. thesis, Universiteit Utrecht, Faculteit Natuur- en Sterrenkunde, Utrecht.

Vautard R, Yiou P & Ghil M (1992) Singular spectrum analysis: a toolkit for short noisy chaotic signals. Physica D 58: 95-126.

Velicogna I &. Wahr J (2006) Measurements of time-variable gravity show mass loss in Antarctica. Science 311(5768): 1754-1756.

Watanabe O, Motoyama H, Igarashi M, Kamiyama K, Matoba S, Goto-Azuma K, Narita H & Kameda T (2001) Studies on climatic and environmental changes during the last hundred years using ice cores from various sites in Nordaustlandet, Svalbard. Mem Natl Inst Polar Res Spec Issue 54: 227-242.

Whillans IM & Cassidy WA (1983) Catch a falling star; meteorites and old ice. Science 222: 55-57.

Wolff E (1990) Signals of atmospheric pollution in polar snow and ice. Antarctic Sci 2: 189-205.

Zagorodnov VS & Zotikov IA (1981) Kernovoye bureniye na Shpitsbergene (Ice core drilling on Spitsbergen). Mater Glyatsiol Issled 40: 157–163.

Zagorodnov VS, Samoylov OY, Raykovskiy YV, Tarusov AV, Kuznetsov MN & Sazonov AV (1984) Glubinnoye stroyeniye lednikovogo plao Lomonosova na o. Zap. Shpitsbergen (Depth structure of the Lomonosov ice plateau, Spitsbergen). Mater Glyatsiol Issled 50: 119–126.

Zar JH (1999) Biostatistical Analysis. Prentice hall, New Jersey.

Zwally HJ, Abdalati W, Herring T, Larson K, Saba J & Steffen K (2002) Surface Melt-Induced Acceleration of Greenland Ice-Sheet Flow. Science 297: 218-222.

Original papers

The following papers comprise the work in this thesis:

I Grinsted A, Moore J, Spikes VB & Sinisalo A (2003) Dating Antarctic blue ice areas using a novel ice flow model. Geophys Res Lett 30(19). doi:10.1029/2003GL017957.

II Grinsted A, Moore JC & Jevrejeva S (2004) Application of the cross wavelet transform and wavelet coherence to geophysical time series. Nonlin Process Geophys 11: 561-566. (http://www.pol.ac.uk/home/research/waveletcoherence/).

III Grinsted A, Moore JC, Pohjola V, Martma T & Isaksson E (2006a) Svalbard summer melting, continentality, and sea ice extent from the Lomonosovfonna ice core. J Geophys Res 111: D07110. doi:10.1029/2005JD006494.

IV Grinsted A, Moore JC & Jevrejeva S (2006b) Observational evidence for volcanic impact on sea level and the global water cycle. (Manuscript).

V Moore & Grinsted (2006) Singular spectrum analysis and envelope detection: methods of enhancing the utility of ground penetrating radar data. J Glaciol 52(176): 159-163(5).

VI Moore J, Grinsted A & Jevrejeva S (2006a) Is there evidence for sunspot forcing of climate at multi-year and decadal periods? Geophys Res Lett 33: L17705. doi:10.1029/2006GL026501.

VII Jevrejeva S, Moore JC & Grinsted A (2004) Oceanic and atmospheric transport of multi-year ENSO signatures to the polar regions. Geophys Res Lett 31: L24210. doi:10.1029/2004GL020871.

VIII Jevrejeva S, Grinsted A, Moore JC & Holgate S (2006c) Nonlinear trends and multiyear cycles in sea level records. J Geophys Res 111: C09012. doi:10.1029/2005JC003229.

Original publications are not included in the electronic version of the dissertation.

I

GEOPHYSICAL RESEARCH LETTERS, VOL. 30, NO. 19, 2005, doi:10.1029/2003GL017957, 2003

Dating Antarctic blue ice areas using a novel ice flow model

Aslak Grinsted,[1,2] John Moore,[1] Vandy Blue Spikes,[3] and Anna Sinisalo[1,2]

Received 13 June 2003; accepted 8 September 2003; published 11 October 2003.

[1] We present a new type of flow model suitable for Antarctic blue ice areas, with application to dating ice for paleoclimate purposes. The volume conserving model uses field data for surface velocities, mass balance and ice thickness along a flow line, with parameterized variation of ice rheology with depth to produce particle trajectories and isochrones. The model is tested on the contrasting Allan Hills Near Western Ice Field and the Scharffenbergbotnen blue ice fields in Antarctica by comparing predicted ages with ages inferred from meteorites and ^{14}C data. During the glacial periods, ice surface velocities at the Allan Hills must have been 25% less, and accumulation rates 50% less than present day values in order to match meteorite ages. In contrast, Scharffenbergbotnen velocities have probably been fairly constant over time due to the atypical valley where it resides. *INDEX TERMS:* 1827 Hydrology: Glaciology (1863); 1863 Hydrology: Snow and ice (1827); 3210 Mathematical Geophysics: Modeling; 9310 Information Related to Geographic Region: Antarctica. **Citation:** Grinsted, A., J. Moore, V. B. Spikes, and A. Sinisalo, Dating Antarctic blue ice areas using a novel ice flow model, *Geophys. Res. Lett.*, *30*(19), 2005, doi:10.1029/2003GL017957, 2003.

1. Introduction

[2] Blue ice areas (BIAs) are characterized by having exposed ice at the surface due to a negative surface mass balance. Of special interest, are blue ice areas where very localized conditions lead to islands of ablation surrounded by accumulation areas. Many Antarctic BIAs are important stranding surfaces for large numbers of meteorites [*Whillans and Cassidy*, 1983]. The age of the surface ice has been determined by radiogenic and meteorite exposure dating to be typically between 10 thousand to 200 thousand years, though some meteorites have terrestrial ages of more than 2 million years [*Bintanja*, 1999; *Harvey et al.*, 1998]. In high altitude BIAs melting does not occur and the areas should contain ancient ice at the surface in essentially pristine state. This valuable source of paleoclimatic data has not been utilized to date, largely because of difficulties in dating the ice. In this paper we present a modeling approach that requires limited, and usually available input data that can be used in BIAs that have rather complicated flow regimes - as in fact do many of them.

[3] For the purposes of modeling, a useful classification is in terms of whether the ice flow is forced to terminate because of outcropping nunataks (closed type), or whether the flow is free (open type). The closed type must have very old surface ice closest to the nunatak where horizontal ice velocity goes to zero, while the open type will have relatively young surface ice as velocities never go to zero.

[4] First we introduce the flow line model, and then use it to date surface ice on a typical open BIA in West Antarctica and a typical closed BIA in East Antarctica. Modeled ages are compared with radiogenic and meteorite exposure ages, and the effects of changing climate on the ice flow regimes examined.

2. Model

[5] A full three dimensional model is always the best approach for ice sheet modeling, however, the necessary input field data are generally unavailable, or limited in temporal coverage. It is much more practical to use a flow line approach where sparse field data can be most easily incorporated into the model. Traditional flow line models have either been based on the shallow ice approximation [e.g., *Paterson*, 1994] or the full stress equilibrium equations [e.g., *Pattyn*, 2002]. The shallow ice type models have problems in areas such as Scharffenbergbotnen where the flow is not always down slope, bedrock relief is large or the flow is constrained by valley sides. Models based on the full stress equilibrium equations are very good for predicting how the ice reacts to mass balance perturbations. However, these models are not fully constrained to the observed data. Attempts to model flow in specific BIAs have also used approaches based on parameterized ice thickness and divergence terms [*Whillans and Cassidy*, 1983; *Azuma et al.*, 1985; *van Roijen*, 1996]. In this paper we introduce a simple model based on volume conservation and force it with the observed surface velocity, ice thickness and mass balance.

[6] We choose x to be the distance along the flow line, z as the water equivalent height above the bed and y is perpendicular to the flow. The model is formulated using a vertically scaled coordinate $\zeta = z/H$, where H is the water equivalent ice thickness. The velocity components of x, y, z and ζ are U, V, W and ω. The horizontal velocity can be written as

$$U(\zeta) = f(\zeta)U_s \quad \text{and} \quad V(\zeta) = 0,$$

where subscript 's' denote the value at the surface. In this paper we assume that ice is frozen at the bed. Empirically we find a reliable approximation is

$$f(\zeta) = \frac{\tanh(k\zeta)}{\tanh(k)}.$$

The value of f, and hence k should reflect the softening of the ice with depth. The rheological behavior of ice depends on its crystal fabric, impurity content and temperature. In

[1]Arctic Centre, University of Lapland, Rovaniemi, Finland.
[2]Department of Geophysics, University of Oulu, Oulu, Finland.
[3]Department of Earth Sciences and the Climate Change Institute, University of Maine, Orono, Maine, USA.

0094-8276/03/2003GL017957$05.00

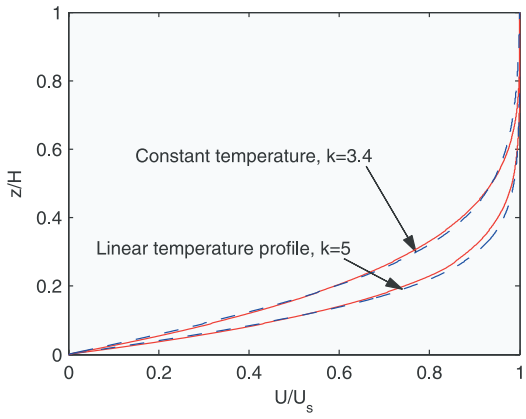

Figure 1. Normalized plot of height above bed against ice velocity. Blue dashed curves are profiles found using the model f, red curves are found using the shallow ice approximation using flow parameters based on the compilation of *Paterson* [1994]. The model f can approximate a wide range of velocity profiles through an appropriate choice of k. The linear temperature profile is for a surface temperature of −30°C and bed temperature of −10°C. We chose $k = 5$ to model both BIAs in the paper.

Antarctica changes due to impurities and crystal fabrics seem much less important than those caused by the temperature profile within the ice sheet [*Paterson*, 1994]. The steady state temperature profile in an ice sheet is linear at the equilibrium line, and as we are dealing with slow flow on each side of the equilibrium line a linear profile is reasonable for the whole flow line (Figure 1). Therefore, we write

$$\frac{\partial U}{\partial x} = f(\zeta)\frac{\partial U_s}{\partial x} \quad \text{and} \quad \frac{\partial V}{\partial y} = f(\zeta)\frac{\partial V_s}{\partial y}.$$

From volume conservation of an ice column we get

$$\frac{\partial U_s}{\partial x} + \frac{\partial V_s}{\partial y} = \frac{1}{f_m}\cdot\left(\frac{\partial U_m}{\partial x} + \frac{\partial V_m}{\partial y}\right) = \frac{b}{f_m H},$$

where b is the mass balance and subscript 'm' denote a mean over the entire ice column. The continuity equation assuming incompressibility is written

$$\frac{\partial U}{\partial x} + \frac{\partial V}{\partial y} + \frac{\partial W}{\partial z} = 0 \Rightarrow \frac{\partial W}{\partial z} = -\left(\frac{\partial U_s}{\partial x} + \frac{\partial V_s}{\partial y}\right)\cdot f(\zeta).$$

Hence

$$\omega(\zeta) = -\left(\frac{\partial U_s}{\partial x} + \frac{\partial V_s}{\partial y}\right)\cdot\int_0^\zeta f(\zeta')d\zeta'$$

$$= \frac{\frac{\partial U_s}{\partial x} + \frac{\partial V_s}{\partial y}}{-k\tanh(k)}\left(\log\left(\frac{1+e^{-2k\zeta}}{2}\right) + k\zeta\right).$$

As input data b, H and U_s are prescribed as functions of x. A Lagrangian integration scheme is then used to calculate particle back trajectories and thus the dating.

[7] This new volume conservation approach with a simple yet realistic velocity profile makes use of all the data typically available. Since the model is so simple, there is basically no room for tuning. We now apply the model to two different BIAs.

3. Allan Hills, Near Western Ice Field (NWIF)

[8] The Allan Hills NWIF (77°S 159°E 2000 m asl) flow line starts on a typical snow accumulation area, passes through the BIA and then continues through downstream snowfields. The flow line, surface velocities, surface elevations and mass balance data (Figure 2) were found from a survey network which was established in 1997 and resurveyed ~2 years later. Ice thickness comes from *Desisle and Sievers* [1991]. Flow is essentially parallel, with little divergence.

[9] Figure 2 shows the particle paths and isochrones along the flow line. It is remarkable that all the surface ice in the BIA was originally deposited within a few km of the equilibrium line. None of the surface ice has been within 150 m of the bedrock. Sensitivity tests with doubled and halved accumulation rates show little difference in surface ages and origin of the ice, whereas changing the surface velocities have a much larger impact.

[10] The modeled maximum age of surface ice is approximately 60 thousand years, using present day mass balance and velocities (Figure 3). For comparison, the maximum terrestrial age of meteorites found on the NWIF is 180 ± 20 thousand years (Kunihiko Nishiizumi, unpublished data). This suggests that accumulation rates and surface velocities have been significantly lower in the past. Deep ice cores and boreholes suggest that surface temperatures

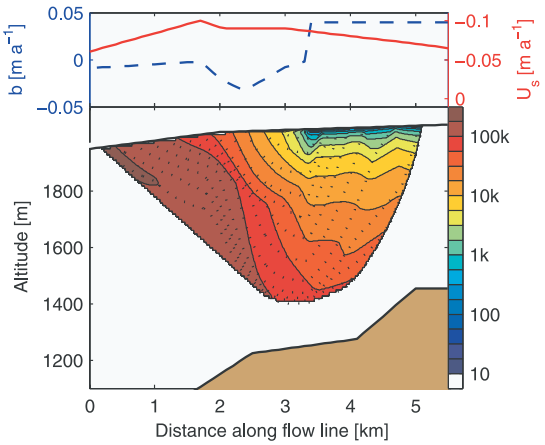

Figure 2. Top: Present day mass balance (dashed blue) and surface velocity (red) along the NWIF flow line. Bottom: Particle paths (dotted lines) and isochrones (colored contours) for the NWIF flow line with accumulation rates 50% and surface velocity 25% of present day values from 11500−115000 and before 125000 years BP.

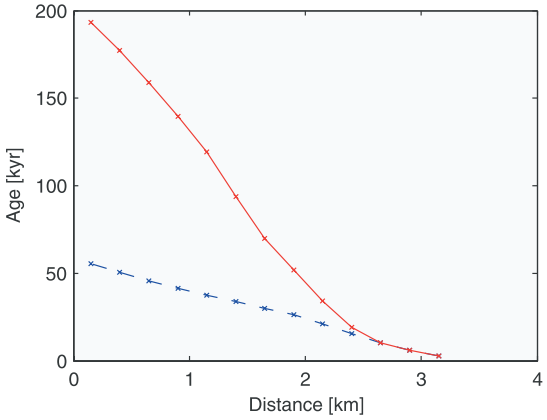

Figure 3. Comparison of surface ages along the NWIF flow line. The dashed blue curve assumes present day accumulation rates and surface velocities (from Figure 2), solid red uses reduced values in the glacial period.

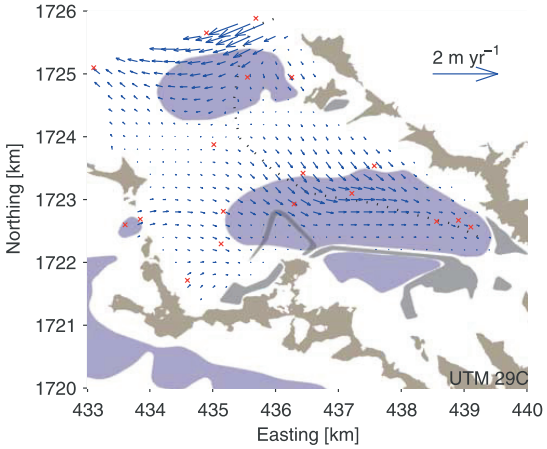

Figure 4. SBB gridded velocity data based on stake measurements (X). The flow line (dotted), the visible extent of BIAs (blue), moraines (grey) and nunataks (brown) are marked.

were about 10–15°C cooler than present, and accumulation rates were about 50% lower during glacial times in Antarctica [*Paterson*, 1994]. Equilibration times for the ice sheet to respond to changes in climate are only in the order of a few thousands of years [*Näslund et al.*, 2000], and a reduction in temperature of the ice sheet by 10°C increases its stiffness by about 3.5 times [*Paterson*, 1994]. Slight changes in ice thickness could result in different surface slopes and thus velocities. As shown in Figure 3 the maximum age of the surface ice changes from about 60 thousand years, using the model with present day velocities and mass balance, to 190 thousand years, by reducing accumulation rates by half and ice velocities to 25% during the glacial periods. Ablation rates are assumed to be constant, which is justified by the similarity between the ablation rates at both BIAs modeled here, despite large differences in surface temperature.

4. Heimefrontfjella, Scharffenbergbotnen (SBB)

[11] SBB (74°S, 11°W, 1200 m asl) is the best-studied blue ice area in Antarctica from a glaciological point of view. The flow line (Figure 4) was picked from gridded surface velocity data [*Sinisalo et al.*, 2003; *van Roijen*, 1996]. Mass balance data (Figure 5) comes from stake observations [*Sinisalo et al.*, 2003], ^{14}C measurements [*van Roijen*, 1996] and radar internal reflections, surface topography from *Sinisalo et al.* [2003] and ice thickness from [*Herzfeld and Holmlund*, 1990].

[12] In contrast to earlier modeling of flow in SBB [*van Roijen*, 1996], it is clear that the ice does not originate from an ice divide at the entrance to the valley (Figure 4), but some comes with the main ice flux from the plateau. The main influx enters through the northern entrance of the valley, with only minor inflows via the shallow and narrow southwestern portal and the eastern end. It is obvious that the valley is most atypical in terms of its low accumulation rate (on the snow covered areas), and very low ice velocities. Wind turbulence inhibits snow accumulation, and since it is a closed BIA, ice flow only just balances net ablation.

[13] The flow line passes over a bedrock high that is an extension of the exposed nunataks along the northeastern side of the valley. Much of the flow from the higher elevation accumulation area does not flow into the valley, but passes across the valley entrance and then to the northwest. The ice that enters the valley diverges as the flow line turns south, and slows considerably. The flow of ice into the valley is regulated by the extent of the divergence, which is heavily influenced by the ice sheet mass balance. During periods of ice sheet thickening (as modeled after the end of the glacial period [*Näslund et al.*,

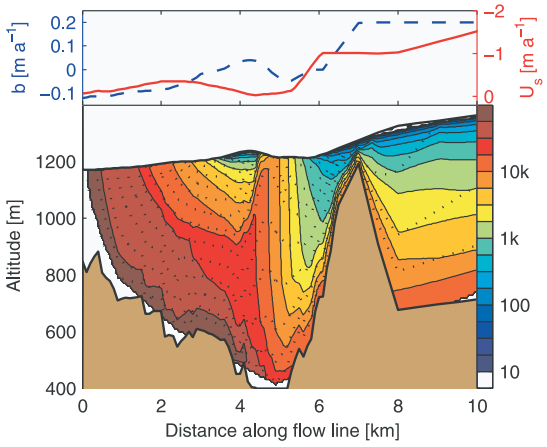

Figure 5. Top: Mass balance (dashed blue) and surface velocity (red) for the SBB flow line. Bottom: Particle paths (dotted lines) and isochrones (colored contours) for the SBB flow line.

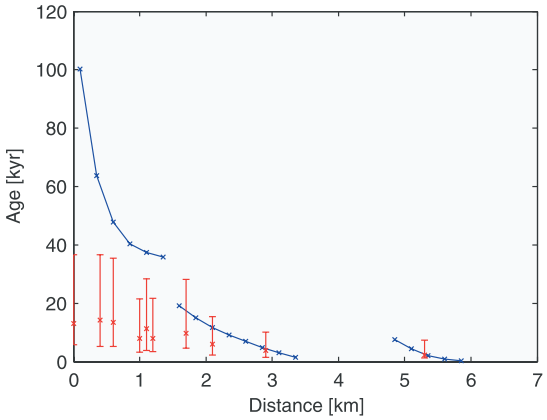

Figure 6. Comparison of surface ages along the SBB flow line (blue line) with ^{14}C ages (converted to calendar years with 1σ error bars, marked in red). The rightmost section of the blue line represent the surface ice in the small BIA, middle section ice in the main BIA originating from the accumulation area inside the valley and the left section ice originating from outside the valley.

2000; *van Roijen*, 1996]), more ice flows into the valley, thereby raising the surface, and eventually inhibiting ice inflow. During periods of thinning, less ice flows into the valley until ablation of the BIA lowers the surface, thereby compensating for reduced influx. In this way the ice velocity inside the valley is not strongly determined by the ice rheology variations caused by changing climate, though the ice flow and accumulation rate outside the valley must be instep with widespread changes. Therefore, in our model, the mass balance and surface velocity fields are left unchanged over time.

[14] Figure 5 shows the particle paths and isochrones along the flow line. Ice from the first 500 m of the flow line (>50 thousand years old) originates from more than 10 km away. The northern small BIA (Figure 4) contains relatively young ice as it is an open-type BIA, and accumulation rates and velocities outside the valley [*Näslund et al.*, 2000] are much higher than within it (Figure 5). The small accumulation area inside the valley supplies ice that is up to 20 thousand years old to the main BIA. The particle paths of the oldest ice nearly reach the bedrock. However, they never come closer than 11 m. It is unclear whether this is close enough to the bed for the ice chronology to have been disturbed. Results from deep ice cores in Greenland [*Taylor et al.*, 1993] suggest that the bottom-most layers are mixed on scales of at least 10 cm.

[15] The most striking result is the discrepancy between the model ages and the ^{14}C ages (Figure 6). Old model ages are an inevitable result of velocities going to zero at the end of the valley. The only way to produce ages comparable to the ^{14}C ages is to make the whole valley an accumulation area in the recent past (∼8000 years BP). However, this leads to an essentially constant surface age for the BIA, which is in conflict with observations of dipping radar layers and visible surface bands. This discrepancy may be because of unaccounted ^{14}C processes such as in situ production by muons [*van der Kemp et al.*, 2002] or CO_2 release from organic compounds [*Colussi and Hoffmann*, 2003]. However, a young age could explain the lack of meteorite finds on this BIA.

5. Conclusion

[16] The flow model has the advantage of being both flexible and simple, allowing realistic particle trajectories to be calculated at arbitrary resolution. The model makes use of input velocity, thickness and mass balance data in a self-consistent way. One significant advantage of using measured surface velocities is that the details of the ice rheology do not need to be considered, beyond estimation of the k parameter. In practice, it is never possible to know the real variations in rheology along a flow line, so this approach is as good as attempting to model rheology directly.

[17] The model does assume volume conservation - i.e. that the ice thickness does not change with time - this is easy to modify if there is a good reason to suppose that ice thickness has changed. However, consideration of at least the SBB example of a closed type BIA suggests that thickness variations over time are very small. The model does accommodate temporally variable surface velocity and mass balance.

[18] Results for NWIF BIA show that open type areas can contain ice as old as 200 thousand years, which is actually comparable with the oldest ice in SBB. The oldest ice from SBB may be disturbed due to flowing within 11 m of the bedrock, so a better climate record may be available from NWIF and open-type ice fields in general. However, the flow in open-type ice fields is more sensitive to climate change, thus making them harder to date. In contrast to many assumptions regarding accumulation areas for BIAs, the two examples presented here have small local catchments. Short flowlines makes paleoclimate interpretations of records from the BIAs much easier.

[19] **Acknowledgments.** Funding was provided by Thule Institute and Finnish Academy through FINNARP. Fieldwork at AH was performed by Ian Whillans and VBS and funded by the United States National Science Foundation.

References

Azuma, M., N. Nakawo, A. Higashi, and F. Nishio, Flow pattern near Massif A in the Yamato bare ice field estimated from the structures and the mechanical properties of a shallow ice core, *Mem. NIPR, Spec. Iss.*, *39*, 173–183, 1985.

Bintanja, R., On the glaciological, meteorological, and climatological significance of Antarctic blue ice areas, *Rev. Geophys.*, *37*, 337–359, 1999.

Colussi, A. J., and M. R. Hoffmann, In situ photolysis of deep ice core contaminants by Çerenkov radiation of cosmic origin, *Geophys. Res. Lett.*, *30*(4), 1195, doi:10.1029/2002GL016112, 2003.

Desisle, G., and J. Sievers, Sub-ice topography and meteorite finds near the Allan Hills and the Near Western Ice Field, Victoria Land, Antarctica, *J. Geophys. Res.*, *96*, 15,577–15,587, 1991.

Harvey, R. P., N. W. Dunbar, W. C. Macintosh, R. P. Esser, K. Nishiizumi, S. Taylor, and M. W. Caffee, Meteoric event recorded in Antarctic ice, *Geology*, *26*(7), 607–610, 1998.

Herzfeld, U. C., and P. Holmlund, Geostatistics in glaciology: Implications of a study of SBB, Dronning Maud Land, East Antarctic, *Ann. Glaciol.*, *14*, 107–110, 1990.

Näslund, J. O., J. L. Fastook, and P. Holmlund, Numerical modelling of the ice sheet in western Dronning Maud Land, East Antarctica: Impacts of present, past and future climates, *J. Glaciol.*, *46*, 54–66, 2000.

Paterson, W. S. B., *The Physics of Glaciers*, 3rd edn, Butterworth-Heinemann, Woburn, Mass., 1994.

Pattyn, F., Transient glacier response with a higher-order numerical ice-flow model, *J. Glaciol.*, *48*, 467–477, 2002.

Sinisalo, A., J. C. Moore, R. V. D. Wal, R. Bintanja, and S. Jonsson, A 14-year mass balance record of a blue ice are in Antarctica, *Ann. Glaciol.*, *37*, in press, 2003.

Taylor, K. C., C. U. Hammer, R. B. Alley, H. B. Clausen, D. Dahl-Jensen, A. J. Gow, N. S. Gundestrup, J. Kipfstuhl, J. C. Moore, and E. D. Waddington, Ice flow and the climate record at Summit, Greenland, *Nature*, *366*, 549–552, 1993.

van der Kemp, W., C. Alderliesten, K. van der Borg, A. F. M. de Jong, R. A. N. Lamers, J. Oerlemans, M. Thomassen, and R. S. W. van der Wal, In situ produced ^{14}C by cosmic ray muons in ablating Antarctic ice, *Tellus*, *45B*, 186–192, 2002.

van Roijen, J. J., Determination of ages and specific mass balances from ^{14}C measurements on Antarctic surface ice, Ph.D. thesis, Faculty of Physics and Astronomy, Utrecht Univ., Utrecht, 1996.

Whillans, I. M., and W. A. Cassidy, Catch a falling star; meteorites and old ice, *Science*, *222*, 55–57, 1983.

A. Grinsted, J. Moore, and A. Sinisalo, Arctic Centre, University of Lapland, P.O. Box 122, FIN-96101 Rovaniemi, Finland. (ag@glaciology.net)

V. B. Spikes, Department of Earth Sciences and the Climate Change Institute, University of Maine, Orono, ME 04469-5790, USA.

II

Nonlinear Processes in Geophysics (2004) 11: 561–566
SRef-ID: 1607-7946/npg/2004-11-561

Nonlinear Processes in Geophysics

Application of the cross wavelet transform and wavelet coherence to geophysical time series

A. Grinsted[1], **J. C. Moore**[1], **and S. Jevrejeva**[2]

[1]Arctic Centre, University of Lapland, Rovaniemi, Finland
[2]Proudman Oceanographic Laboratory, Birkenhead, UK

Received: 11 June 2004 – Revised: 19 October 2004 – Accepted: 16 November 2004 – Published: 18 November 2004

Part of Special Issue "Nonlinear analysis of multivariate geoscientific data – advanced methods, theory and application"

Abstract. Many scientists have made use of the wavelet method in analyzing time series, often using popular free software. However, at present there are no similar easy to use wavelet packages for analyzing two time series together. We discuss the cross wavelet transform and wavelet coherence for examining relationships in time frequency space between two time series. We demonstrate how phase angle statistics can be used to gain confidence in causal relationships and test mechanistic models of physical relationships between the time series. As an example of typical data where such analyses have proven useful, we apply the methods to the Arctic Oscillation index and the Baltic maximum sea ice extent record. Monte Carlo methods are used to assess the statistical significance against red noise backgrounds. A software package has been developed that allows users to perform the cross wavelet transform and wavelet coherence (http://www.pol.ac.uk/home/research/waveletcoherence/).

1 Introduction

Geophysical time series are often generated by complex systems of which we know little. Predictable behavior in such systems, such as trends and periodicities, is therefore of great interest. Most traditional mathematical methods that examine periodicities in the frequency domain, such as Fourier analysis, have implicitly assumed that the underlying processes are stationary in time. However, wavelet transforms expand time series into time frequency space and can therefore find localized intermittent periodicities. There are two classes of wavelet transforms; the Continuous Wavelet Transform (CWT) and its discrete counterpart (DWT). The DWT is a compact representation of the data and is particularly useful for noise reduction and data compression whereas the CWT is better for feature extraction purposes. As we are interested in extracting low s/n ratio signals in time series we discuss only CWT in this paper. While CWT is a common tool for analyzing localized intermittent oscillations in a time series, it is very often desirable to examine two time series together that may be expected to be linked in some way. In particular, to examine whether regions in time frequency space with large common power have a consistent phase relationship and therefore are suggestive of causality between the time series. Many geophysical time series are not Normally distributed and we suggest methods of applying the CWT to such time series. From two CWTs we construct the Cross Wavelet Transform (XWT) which will expose their common power and relative phase in time-frequency space. We will further define a measure of Wavelet Coherence (WTC) between two CWT, which can find significant coherence even though the common power is low, and show how confidence levels against red noise backgrounds are calculated.

We will present the basic CWT theory before we move on to XWT and WTC. New developments such as quantifying the phase relationship and calculating the WTC significance level will be treated more fully. When using the methods on time series it is important to have solid mechanistic foundations on which to base any relationships found, and we caution against using the methods in a "scatter-gun" approach (particularly if the time series probability density functions are modified). To illustrate how the various methods are used we apply them to two data sets from meteorology and glaciology. Finally, we will provide links to a MatLab software package.

Correspondence to: A. Grinsted
(ag@glaciology.net)

2 Data

An example of two physical effects that we expect to be linked from consideration of the climate system are the mean winter state of the arctic atmosphere and winter severity reflected by ice conditions.

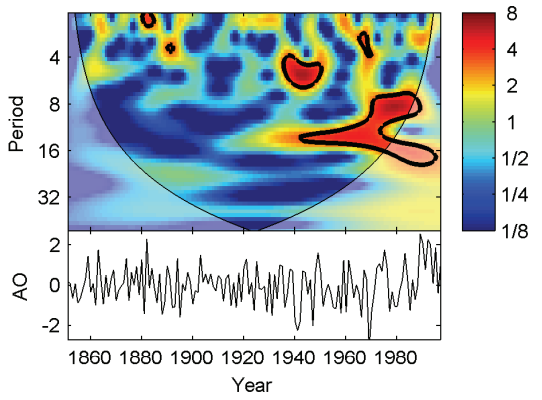

Fig. 1. The standardized time series of winter (DJF) AO (bottom) and its continuous wavelet power spectrum (top). The thick black contour designates the 5% significance level against red noise and the cone of influence (COI) where edge effects might distort the picture is shown as a lighter shade. The standardized AO series has an AR1 coefficient of 0.02.

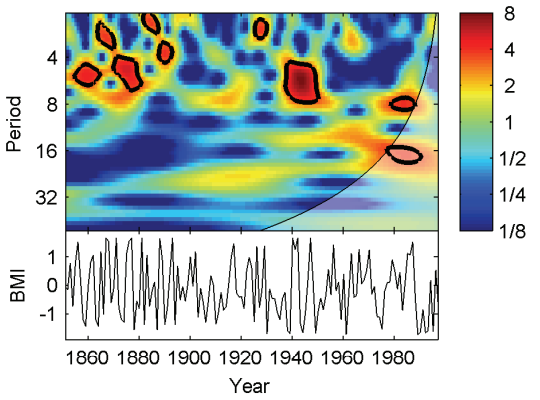

Fig. 2. The standardized BMI percentile time series (bottom) and its continuous wavelet power (top). The thick contour designates the 5% significance level against red noise and the cone of influence (COI) where edge effects might distort the picture is shown as a lighter shade. The standardized BMI percentile series has an AR1 coefficient of 0.08.

The Arctic Oscillation (AO) is a key aspect of climate variability in the Northern Hemisphere. The AO is defined as the leading empirical orthogonal function (EOF) of Northern Hemisphere sea level pressure anomalies pole ward of 20°N (Thompson and Wallace, 1998), and characterized by an exchange of atmospheric mass between the Arctic and middle latitudes. The Baltic Sea is a transition zone between the North Atlantic region and the continental area of Eurasia, leading to large inter-annual variability of ice conditions. The Baltic Sea is partly covered by ice every winter season, the maximum annual ice extent varies between 10–100% of the sea area, the length of ice season is 4–7 months, and the maximum annual thickness of ice is 50–120 cm (Jevrejeva, 2001; Seinä et al., 2001). Recently published results demonstrate that large-scale atmospheric circulation patterns in the Arctic and North Atlantic described by the AO or by the somewhat similar North Atlantic Oscillation teleconnections significantly control ice conditions in the Baltic Sea (Loewe and Koslowski, 1998; Omstedt and Chen, 2001; Jevrejeva and Moore, 2001; Jevrejeva, 2002).

In this paper, we examine the connection between winter AO and Baltic Sea ice extent and especially explore the phase relationships between the series in the light of the expected causality links. Ice conditions are represented by the time series of maximum annual ice extent in the Baltic Sea (BMI) for the period 1720–2000 (Seinä et al., 2001). We use the winter AO index (December–February 1851–1997) of Thompson and Wallace (1998).

Many statistical tests assume that the probability density function (pdf) is close to Normal. Our experience with CWTs of geophysical time series shows that series far from normally distributed produces rather unreliable and less significant results. Occasionally it can therefore be a good idea to transform the pdf of the time series. However, we caution against rashly changing the pdf. The BMI index is bi-modally distributed with maximum probabilities around 70 000 km^2 and 420 000 km^2. A simple periodic oscillation between these two modes will almost have the shape of a square wave. The power of a square wave leaks into frequency bands outside the fundamental period. We therefore transform the BMI index into a record of percentiles (in terms of its cumulative distribution function) and thus forcing the pdf to be rectangular. This has the effect of narrowing the bandwidth of intermittent oscillations. We standardize (zero mean, unit standard deviation) both time series and will refer to the standardized versions as simply AO and BMI. The time series of the AO and BMI time series are shown in Figs. 1 and 2.

3 Methods

3.1 The Continuous Wavelet Transform (CWT)

A wavelet is a function with zero mean and that is localized in both frequency and time. We can characterize a wavelet by how localized it is in time (Δt) and frequency ($\Delta\omega$ or the bandwidth). The classical version of the Heisenberg uncertainty principle tells us that there is always a tradeoff between localization in time and frequency. Without properly defining Δt and $\Delta\omega$, we will note that there is a limit to how small the uncertainty product $\Delta t{\cdot}\Delta\omega$ can be. One particular wavelet, the Morlet, is defined as

$$\psi_0(\eta) = \pi^{-1/4} e^{i\omega_0\eta} e^{-\frac{1}{2}\eta^2} . \quad (1)$$

where ω_0 is dimensionless frequency and η is dimensionless time. When using wavelets for feature extraction purposes

the Morlet wavelet (with ω_0=6) is a good choice, since it provides a good balance between time and frequency localization. We therefore restrict our further treatment to this wavelet, although the methods we present are generally applicable (see, e.g. Foufoula-Georgiou, 1995).

The idea behind the CWT is to apply the wavelet as a band-pass filter to the time series. The wavelet is stretched in time by varying its scale (s), so that η=s·t, and normalizing it to have unit energy. For the Morlet wavelet (with ω_0=6) the Fourier period (λ_{wt}) is almost equal to the scale (λ_{wt}=1.03 s). The CWT of a time series (x_n, n=1,...,N) with uniform time steps δt, is defined as the convolution of x_n with the scaled and normalized wavelet. We write

$$W_n^X(s) = \sqrt{\tfrac{\delta t}{s}} \sum_{n'=1}^{N} x_{n'} \psi_0 \left[\left(n' - n\right) \tfrac{\delta t}{s} \right]. \quad (2)$$

In practice it is faster to implement the convolution in Fourier space (see details in Torrence and Compo, 1998). We define the wavelet power as $|W_n^X(s)|^2$. The complex argument of $W_n^X(s)$ can be interpreted as the local phase.

The CWT has edge artifacts because the wavelet is not completely localized in time. It is therefore useful to introduce a Cone of Influence (COI) in which edge effects can not be ignored. Here we take the COI as the area in which the wavelet power caused by a discontinuity at the edge has dropped to e^{-2} of the value at the edge.

The statistical significance of wavelet power can be assessed relative to the null hypotheses that the signal is generated by a stationary process with a given background power spectrum (P_k). Many geophysical time series have distinctive red noise characteristics that can be modeled very well by a first order autoregressive (AR1) process. The Fourier power spectrum of an AR1 process with lag-1 autocorrelation α (estimated from the observed time series e.g. Allen and Smith, 1996) is given by

$$P_k = \frac{1-\alpha^2}{\left|1-\alpha e^{-2i\pi k}\right|^2}, \quad (3)$$

where k is the Fourier frequency index.

The wavelet transform can be thought of as a consecutive series of band-pass filters applied to the time series where the wavelet scale is linearly related to the characteristic period of the filter (λ_{wt}). Hence, for a stationary process with the power spectrum P_k the variance at a given wavelet scale, by invocation of the Fourier convolution theorem, is simply the variance in the corresponding band of P_k. If P_k is sufficiently smooth then we can approximate the variance at a given scale simply with P_k using the conversion k^{-1}=λ_{wt}. Torrence and Compo (1998) use Monte Carlo methods to show that this approximation is very good for the AR1 spectrum. They then show that the probability that the wavelet power, of a process with a given power spectrum (P_k), being greater than p is

$$D\left(\frac{\left|W_n^X(s)\right|^2}{\sigma_X^2} < p\right) = \frac{1}{2} P_k \chi_\nu^2(p), \quad (4)$$

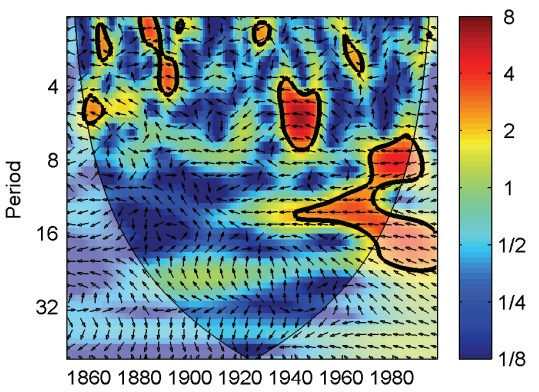

Fig. 3. Cross wavelet transform of the standardized AO and BMI time series. The 5% significance level against red noise is shown as a thick contour. The relative phase relationship is shown as arrows (with in-phase pointing right, anti-phase pointing left, and BMI leading AO by 90° pointing straight down).

where ν is equal to 1 for real and 2 for complex wavelets.

The CWT of the AO and BMI are shown in Figs. 1 and 2 respectively. There are clearly common features in the wavelet power of the two time series such as the significant peak in the ~5 year band around 1940. Both series also have high power in the 2–7 year band in the period from 1860–1900, though for AO the power is not above the 5% significance level. However, the similarity between the portrayed patterns in this period is quite low and it is therefore hard to tell if it is merely a coincidence. The cross wavelet transform helps in this regard.

3.2 The cross wavelet transform

The cross wavelet transform (XWT) of two time series x_n and y_n is defined as W^{XY}=$W^X W^{Y*}$, where * denotes complex conjugation. We further define the cross wavelet power as $|W^{XY}|$. The complex argument arg(W^{xy}) can be interpreted as the local relative phase between x_n and y_n in time frequency space. The theoretical distribution of the cross wavelet power of two time series with background power spectra P_k^X and P_k^Y is given in Torrence and Compo (1998) as

$$D\left(\frac{\left|W_n^X(s) W_n^{Y*}(s)\right|}{\sigma_X \sigma_Y} < p\right) = \frac{Z_\nu(p)}{\nu} \sqrt{P_k^X P_k^Y}, \quad (5)$$

where $Z_\nu(p)$ is the confidence level associated with the probability p for a pdf defined by the square root of the product of two χ^2 distributions. For example the 5% significance level marked in Fig. 3 is calculated using Z_2(95%)=3.999.

The XWT of AO and BMI is shown in Fig. 4. Here we notice that the common features we found by eye from the individual wavelet transforms stand out as being significant at the 5% level. We also note that there also is significant common power in the ~10–16 year band from 1940–1980.

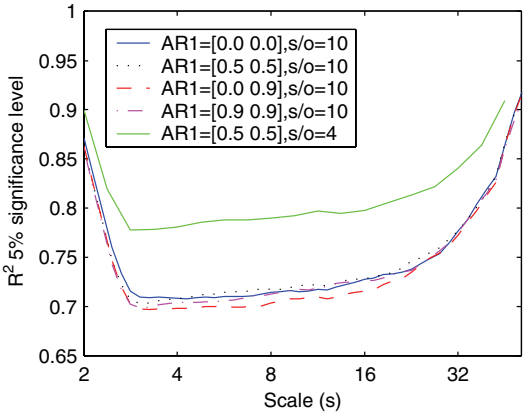

Fig. 4. Wavelet coherence 5% significance level determined using Monte Carlo generated noise (with 10 000 surrogate data set pairs). The legend shows the 2 AR1 coefficients of the surrogate data sets and the numbers of scales per octave (s/o) used in calculating the scale smoothing. The color of the noise has little impact on the significance level, whereas the specifics of the smoothing have a large impact. The large values at either end of the spectrum are due to the scale smoothing operator reaching the scale boundaries.

For there to be a simple cause and effect relationship between the phenomena recorded in the time series we would expect that the oscillations are phase locked. So, it is comforting that the XWT show that AO and BMI are in anti phase in all the sectors with significant common power. Since AO and BMI are in anti-phase across all scales, we conclude that BMI to a large extent simply mirrors the AO. Outside the areas with significant power the phase relationship is also predominantly anti phase. We therefore speculate that there is a stronger link between AO and BMI than that implied by the cross wavelet power.

3.3 Cross wavelet phase angle

As we are interested in the phase difference between the components of the two time series we need to estimate the mean and confidence interval of the phase difference. We use the circular mean of the phase over regions with higher than 5% statistical significance that are outside the COI to quantify the phase relationship. This is a useful and general method for calculating the mean phase. The circular mean of a set of angles (a_i, i=1...n) is defined as (e.g. Zar, 1999)

$$a_m = \arg(X, Y) \text{ with } X = \sum_{i=1}^{n} \cos(a_i) \text{ and } Y = \sum_{i=1}^{n} \sin(a_i), \quad (6)$$

It is difficult to calculate the confidence interval of the mean angle reliably since the phase angles are not independent. The number of angles used in the calculation can be set arbitrarily high simply by increasing the scale resolution. However, it is interesting to know the scatter of angles around the mean. For this we define the circular standard deviation as

$$s = \sqrt{-2\ln(R/n)}, \quad (7)$$

where $R=\sqrt{(X^2+Y^2)}$. The circular standard deviation is analogous to the linear standard deviation in that it varies from zero to infinity. It gives similar results to the linear standard deviation when the angles are distributed closely around the mean angle. In some cases there might be reasons for calculating the mean phase angle for each scale, and then the phase angle can be quantified as a number of years.

The XWT phase angle within the 5% significant regions and outside the COI has the mean phase –176±12° (where ± designates the circular standard deviation). This basically confirms the conclusion that AO and BMI are in anti-phase. Note that the time series already have a 3 month lag since the ice extent is greatest in April. A 3 month lag is consistent with the mechanism of stratospheric forcing of the troposphere (Baldwin et al., 2001; Jevrejeva et al., 2003). The observation that the phase angles are constant across all scales argues for a constant time lag due to the physical mechanism of signal propagation from the AO to the ice extent. The deviation from completely anti-phase suggests that AO leads BMI slightly, however, the circular standard deviation is too large to make any firm conclusion.

3.4 Wavelet coherence

Cross wavelet power reveals areas with high common power. Another useful measure is how coherent the cross wavelet transform is in time frequency space. Following Torrence and Webster (1998) we define the wavelet coherence of two time series as

$$R_n^2(s) = \frac{\left|S\left(s^{-1}W_n^{XY}(s)\right)\right|^2}{S\left(s^{-1}\left|W_n^X(s)\right|^2\right)\cdot S\left(s^{-1}\left|W_n^Y(s)\right|^2\right)}, \quad (8)$$

where S is a smoothing operator. Notice that this definition closely resembles that of a traditional correlation coefficient, and it is useful to think of the wavelet coherence as a localized correlation coefficient in time frequency space. We write the smoothing operator S as

$$S(W) = S_{scale}(S_{time}(W_n(s))), \quad (9)$$

where S_{scale} denotes smoothing along the wavelet scale axis and S_{time} smoothing in time. It is natural to design the smoothing operator so that it has a similar footprint as the wavelet used. For the Morlet wavelet a suitable smoothing operator is given by Torrence and Webster (1998)

$$S_{time}(W)|_s = \left(W_n(s) * c_1^{\frac{-t^2}{2s^2}}\right)\Big|_s,$$
$$S_{time}(W)|_s = \left(W_n(s) * c_2\Pi(0.6\,s)\right)\Big|_n, \quad (10)$$

where c_1 and c_2 are normalization constants and Π is the rectangle function. The factor of 0.6 is the empirically determined scale decorrelation length for the Morlet wavelet (Torrence and Compo, 1998). In practice both convolutions are

done discretely and therefore the normalization coefficients are determined numerically.

The statistical significance level of the wavelet coherence is estimated using Monte Carlo methods. We generate a large ensemble of surrogate data set pairs with the same AR1 coefficients as the input datasets. For each pair we calculate the wavelet coherence. We then estimate the significance level for each scale using only values outside the COI. Empirical testing shows that the AR1 coefficients have little impact on the significance level. The specifics of the smoothing operator, however, have a large impact. For example the resolution chosen when calculating the scale smoothing has a major influence on the significance level (see Fig. 4). The Monte Carlo estimation of the significance level requires of the order of 1000 surrogate data set pairs. The number of scales per octave should be high enough to capture the rectangle shape of the scale smoothing operator while minimizing computing time. Empirically we find 10 scales per octave to be satisfactory.

The squared WTC of AO and BMI is shown in Fig. 5. Compared with the XWT a larger section stands out as being significant and all these areas show an anti-phase relationship between AO and BMI. The area of a time frequency plot above the 5% significance level is not a reliable indication of causality. Even if the scales were appropriately weighed for the averaging, it is possible for two series to be perfectly correlated at one specific scale while the area of significant correlation is much less than 5%. However, the significant region of Fig. 5 is so extensive that it is very unlikely that this is simply by chance. Oscillations in AO are manifested in the BMI on wavelengths varying from 2–20 years, suggesting that BMI passively mirrors AO. Regions with low coherence coincide with low wavelet power in the AO and are therefore expected. Possibly because the EOF that AO represents is not really capturing the actual location of the centers of action during the Little Ice Age. As with the XWT, we can calculate the mean phase angle of the significant regions. The mean phase angle over the regions with significant wavelet coherence and outside the COI is 174±15°.

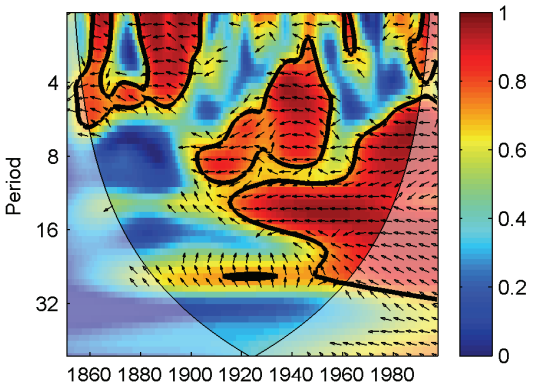

Fig. 5. Squared wavelet coherence between the standardized AO and BMI time series. The 5% significance level against red noise is shown as a thick contour. All significant sections show anti-phase behavior.

4 Summary

The CWT expands a time series into a time frequency space where oscillations can be seen in a highly intuitive way. The Morlet wavelet (with ω_0=6) is a good choice when using wavelets for feature extraction purposes, because it is reasonably localized in both time and frequency. From the CWTs of two time series one can construct the XWT. The XWT exposes regions with high common power and further reveals information about the phase relationship. If the two series are physically related we would expect a consistent or slowly varying phase lag that can be tested against mechanistic models of the physical process. WTC can be thought of as the local correlation between two CWTs. In this way locally phase locked behavior is uncovered. The more desirable features of the WTC come at the price of being slightly less localized in time frequency space. The significance level of the WTC has to be determined using Monte Carlo methods.

4.1 Practical tips

Cross wavelet analysis and wavelet coherence are powerful methods for testing proposed linkages between two time series.

- Check the histograms of the time series to ensure that they are not too far from normally distributed. Consider transforming the time series, if the pdf's of the time series are far from Gaussian. When choosing a transformation, it is preferable to choose an analytic transformation such as taking the logarithm if the data is log-normally distributed. In other cases the simple "percentile" transformation we used for the BMI might be useful. An advantage of using that particular transformation is that it does not have any outliers.

- Consider what the expectations are for the outcome of the analysis given the proposed linking mechanism. We caution against blindly applying these methods to randomly chosen data sets. Like other statistical tests some data set sets will display highly statistically significant links simply by chance.

- When a wavelet has been chosen the CWTs of both time series are calculated. We suggest a scale resolution of 10 scales per octave and use of the Morlet wavelet unless there are good grounds to do otherwise. For geophysical time series an AR1 red noise assumption is often suitable and Eqs. (3) and (4) can be used to calculate the significance level of the wavelet power. Remember to take special care not to misinterpret results inside the COI.

– From the two CWTs the XWT is calculated. The XWT exposes regions with high common power and further reveals information about the phase relationship. If the two series are physically related we would expect a consistent or slowly varying phase lag that can be tested against mechanistic models of the physical process. The circular mean of the phase angles can be used to quantify the phase relationship.

– Also, from two CWTs the WTC can be calculated which can be thought of as the local correlation between the time series in time frequency space. Where XWT unveils high common power, WTC finds locally phase locked behavior. The more desirable features of the WTC come at the price of being slightly less localized in time frequency space. The significance level of the WTC has to be determined using Monte Carlo methods.

A MatLab software package by the authors for performing XWT and WTC can be found at http://www.pol.ac.uk/home/research/waveletcoherence/.

Acknowledgements. Financial assistance was provided by the Thule Institute. Some of our software includes code originally written by C. Torrence and G. Compo that is available at: http://paos.colorado.edu/research/wavelets/ and by E. Breitenberger of the University of Alaska which were adapted from the freeware SSA-MTM Toolkit: http://www.atmos.ucla.edu/tcd/ssa.

Edited by: M. Thiel
Reviewed by: two referees

References

Allen, M. R. and Smith, L. A.: Monte Carlo SSA: Detecting irregular oscillations in the presence of coloured noise, J. Clim., 9, 3373–3404, 1996.

Baldwin, M. P., Gray, L. J., Dunkerton, T. J., Hamilton, K., Haynes, P. H., Randel, W. J., Holton, J. R., Alexander, M. J., Hirota, I., Horinouchi, T., Jones, D. B. A., Kinnerslay, J. S., Marquardt, C., Sato, K., and Tarahashi, M.: The Quasi-Biennial Oscillation, Rev. Geophys., 39, 170–229, 2001.

Foufoula-Georgiou, E. and Kumar, P.: Wavelets in Geophysics, Academic Press, 373, 1995.

Jevrejeva, S. and Moore, J. C.: Singular Spectrum Analysis of Baltic Sea ice conditions and large-scale atmospheric patterns since 1708, Geophys. Res. Lett., 28, 4503–4507, 2001.

Jevrejeva, S.: Association between the ice conditions in the Baltic Sea and the North Atlantic Oscillation, Nordic Hydrol., 33, 319–330, 2002.

Jevrejeva, S., Moore, J. C., and Grinsted, A.: Influence of the Arctic Oscillation and El Ninō-Southern Oscillation (ENSO) on ice conditions in the Baltic Sea: The wavelet approach, J. Geophys. Res., 108(D21), 4677, doi:10.1029/2003JD003417, 2003.

Loewe, P. and Koslowski, G. : The Western Baltic Sea ice season in terms of a mass-related severity index 1879–1992, II Spectral characteristics and associations with NAO, QBO and solar cycle, Tellus, 50A, 219–241, 1998.

Omstedt, A. and Chen, D.: Influence of atmospheric circulation on the maximum ice extent in the Baltic Sea, J. Geophys. Res., Vol. 106, 4493–4500, 2001.

Seinä, A., Grönvall, H., Kalliosaari, S., and Vainio, J.: Ice seasons 1996–2000 in Finnish sea areas / Jäätalvet 1996–2000 Suomen merialueilla, Meri, Report Series of the Finnish Institute of Marine Research, 43, 2001.

Thompson, D. W. J. and Wallace, J. M.: The Arctic Oscillation signature in the winter geopotential height and temperature fields, Geophys. Res. Lett., 25, 1297–1300, 1998.

Torrence, C. and Compo, G. P.: A practical guide to wavelet analysis, Bull. Am. Meteorol. Soc., 79, 61–78, 1998.

Torrence, C. and Webster, P.: Interdecadal Changes in the ESNO-Monsoon System, J. Clim., 12, 2679–2690, 1999.

Zar, J. H.: Biostatistical Analysis, Prentice hall, New Jersey, 1999.

III

JOURNAL OF GEOPHYSICAL RESEARCH, VOL. 111, D07110, doi:10.1029/2005JD006494, 2006

Svalbard summer melting, continentality, and sea ice extent from the Lomonosovfonna ice core

Aslak Grinsted,[1,2] John C. Moore,[1] Veijo Pohjola,[3] Tõnu Martma,[4] and Elisabeth Isaksson[5]

Received 13 July 2005; revised 25 October 2005; accepted 18 January 2006; published 14 April 2006.

[1] We develop a continentality proxy (1600–1930) based on amplitudes of the annual signal in oxygen isotopes in an ice core. We show via modeling that by using 5 and 15 year average amplitudes the effects of diffusion and varying layer thickness can be minimized, such that amplitudes then reflect real seasonal changes in $\delta^{18}O$ under the influence of melt. A model of chemical fractionation in ice based on differing elution rates for pairs of ions is developed as a proxy for summer melt (1130–1990). The best pairs are sodium with magnesium and potassium with chloride. The continentality and melt proxies are validated against twentieth-century instrumental records and longer historical climate proxies. In addition to summer temperature, the melt proxy also appears to reflect sea ice extent, likely as a result of sodium chloride fractionation in the oceanic sea ice margin source area that is dependent on winter temperatures. We show that the climate history they depict is consistent with what we see from isotopic paleothermometry. Continentality was greatest during the Little Ice Age but decreased around 1870, 20–30 years before the rise in temperatures indicated by the $\delta^{18}O$ profile. The degree of summer melt was significantly larger during the period 1130–1300 than in the 1990s.

Citation: Grinsted, A., J. C. Moore, V. Pohjola, T. Martma, and E. Isaksson (2006), Svalbard summer melting, continentality, and sea ice extent from the Lomonosovfonna ice core, *J. Geophys. Res.*, *111*, D07110, doi:10.1029/2005JD006494.

1. Introduction

[2] Ice cores hold many potential proxies of climate. The difficulty is usually to assign a proxy to a particular climatic variable [*Jones and Mann*, 2004]. One of the most well known is $\delta^{18}O$, which is the deviation of the isotopic ratio between H_2O^{18} to H_2O^{16} from the ratio in standard seawater [*Dansgaard*, 1964]. In precipitation $\delta^{18}O$ is generally accepted as being a proxy for condensation temperature in the atmosphere and is related to the surface temperature in modern snow [*van Lipzig et al.*, 2002].

[3] However, the relationship between $\delta^{18}O$ and surface temperature changes under different climate regimes as it is affected by changes in moisture source temperature, seasonality of precipitation and moisture transport path. In addition to mean temperature, the seasonal difference between summer and winter is of broad environmental significance. Continental interiors have larger seasonal temperature variations than maritime areas and the annual temperature range is often used as a measure of continentality. Ice cores from the interiors of large ice sheets such as Greenland or Antarctica are probably not very sensitive to the location of the sea ice margin, which determines the distance to open water and hence influences continentality, as it is far away from the drilling site. However, an ice core from an island near the seasonal sea ice margin may reflect the much larger relative variations in distance to open water via a continentality index. In ice cores where the seasonal cycle in $\delta^{18}O$ is well preserved the amplitude is an obvious candidate as a proxy for continentality. Unfortunately the oxygen isotope record is often affected by diffusion on a scale comparable to the annual layer thickness. It is relatively common to back diffuse the isotopic profile to amplify the annual cycle for layer counting purposes [*Bolzan and Pohjola*, 2000]. However, the reconstructed amplitude from back diffusion is very sensitive to small errors [*Johnsen et al.*, 2000] and, in sites with seasonal melt, back diffusion is problematic as it is expected that diffusion acts very unevenly.

[4] Stratigraphic melt index (SMI) is defined as the weight fraction of clear bubble-free ice. SMI has been used as a proxy for summer temperature on Canadian ice caps [e.g., *Koerner*, 1997]. However, in Greenland, *Pfeffer and Humphrey* [1998] suggest that melt layers not only reflect warm summer conditions but also the temperature gradient experienced by the snowpack during the preceding months. Therefore, under some conditions, SMI is also affected by the seasonal temperature range, or continentality, and accumulation rate.

[5] Almost all ice cores in the Arctic outside of Greenland are influenced by seasonal melt. Meltwater can refreeze on the surface, percolate into deeper layers or run off. If meltwater refreezes in the surface layers, then it has little impact on average ion concentrations and $\delta^{18}O$ values.

[1] Arctic Centre, University of Lapland, Rovaniemi, Finland.
[2] Department of Geophysics, University of Oulu, Oulu, Finland.
[3] Department of Earth Sciences, Uppsala University, Uppsala, Sweden.
[4] Institute of Geology, Tallinn University of Technology, Tallinn, Estonia.
[5] Norwegian Polar Institute, Tromsø, Norway.

0148-0227/06/2005JD006494$09.00

Percolation and runoff affects ions much more strongly than isotopes because most ions have a very strong affinity for the water phase and even small amounts of meltwater will have high concentrations of ions [*Davies et al.*, 1982]. Percolation however only redistributes the ions in the snowpack whereas they are lost by runoff. *Iizuka et al.* [2002] use the preferential removal of ions from particular layers as an indicator for seasonal melt on Austfonna, Svalbard, and find empirically that the magnesium sodium ratio was the best melt proxy.

[6] In 1997 we drilled a 121-m-long ice core (spanning about 800 years) on Lomonosovfonna [*Isaksson et al.*, 2001], the highest ice field in Svalbard (78°51′53″N, 17°25′30″E, 1255 m above sea level (asl)). Total ice depth from radar sounding was 123 m, and the site is close to the highest point of the ice cap with roughly radial ice flow. Dating of the core was based on a layer-thinning model tied with the known dates of prominent reference horizons (see *Kekonen et al.* [2005] for details). There is evidence that $\delta^{18}O$ is a good proxy for surface air temperature at the drill site: the rise in $\delta^{18}O$ from 1900 to 1920 that mirrors the rise in temperature seen in the instrumental record from Svalbard [*Isaksson et al.*, 2003], consistency with the borehole temperature profile [*van de Wal et al.*, 2002], and well-preserved annual cycles [*Pohjola et al.*, 2002b]. The current annual temperature range is from 0°C to about −40°C, though temperatures within the firn pack tend to be much warmer, approaching −3°C at 15 m depth [*van de Wal et al.*, 2002].

[7] The soluble ion chemical record in the ice core spans the last 800 years [*Kekonen et al.*, 2005] and shows clearly defined changes corresponding with different climatic periods and anthropogenic pollution. For the Lomonosovfonna core the impact of percolation is much less significant than the impact of changes in precipitation chemistry [*Moore et al.*, 2005]. All ions except ammonium have anomalously low concentrations in the oldest ice of the core. This is interpreted as loss of ions in the original snowpack caused by warm conditions prior to about 1300 [*Kekonen et al.*, 2005]. SMI for the core shows no relationship with oxygen isotopes [*Pohjola et al.*, 2002a], and thus we cannot interpret SMI as a proxy for summer temperature at the site.

[8] In this paper we develop the theoretical basis for both continentality and melt proxies and apply them to the chemical [*Kekonen et al.*, 2005] and the oxygen isotope records [*Isaksson et al.*, 2003] from the Lomonosovfonna ice core. We test the ice core proxies against instrumental temperature and historical sea ice extent over the last 150 years and then use the ice core proxies to derive climatic variables back to 1130. While summer temperature proxies are common, such as tree ring width chronologies, we will show that we have proxies of both summer melting and annual temperature range, both of which seem to be influenced by regional sea ice extent.

2. Data

[9] The oxygen isotopic record ($\delta^{18}O$) has been measured at 5 cm resolution [*Isaksson et al.*, 2003]. The concentration of ions (Cl^-, NO_3^-, SO_4^{2-}, $CH_3SO_3^-$, NH_4^+, K^+, Ca^{2+}, Mg^{2+}, Na^+) has been measured in 5 cm samples taken at 10 cm intervals along the whole core. Sample recovery and analysis are discussed by *Kekonen et al.* [2005, and references therein]. SMI has been measured at 5 mm resolution in the top 80 m (1707–1997 A.D.) of the core by visually classifying into firn, bubbly ice, diffuse ice and clear ice and assigning a melt percentage to each category [*Pohjola et al.*, 2002a].

[10] We will compare our ice core proxies to local historical temperatures and also to Barents Sea ice extent since this is a major driving force of regional climate [*Isaksson et al.*, 2003, 2005a, 2005b]. Svalbard Airport reconstructed temperature, from 80km south west of the drill site, is the closest instrumental historical record. This is a composite record from sites near Longyearbyen and has monthly mean temperatures since 1911 [*Nordli et al.*, 1996]. We extract winter (T_{DJF}), summer (T_{JJA}) and yearly mean temperatures (T_m) as well as yearly temperature range (ΔT). Records of Barents sea ice extent have been compiled from ship logbooks [*Vinje*, 2001]. April sea ice extent for the eastern and western Barents Sea (B_e and B_w, respectively) covers the period from 1864 to 1999, with few gaps most notably in the WWII years. We have left the missing years out of correlations with other records.

3. Methods

3.1. Continentality From $\delta^{18}O$

3.1.1. Factors Contributing to $\delta^{18}O$ Amplitudes

[11] The amplitude of the annual signal in $\delta^{18}O$ (A) is an obvious candidate for a continentality proxy, since $\delta^{18}O$ on Lomonosovfonna is a proxy for surface air temperature [*Isaksson et al.*, 2001; *van de Wal et al.*, 2002] and the annual cycle is well preserved [*Pohjola et al.*, 2002b]. However, there are complicating factors in using the measured amplitudes. Meltwater percolation redistributes isotopes, effectively reducing the annual amplitudes. Further, the amplitudes decay with depth because of isotopic diffusion [*Johnsen et al.*, 2000].

[12] Diffusion acts so as to smooth out steep gradients in the signal, so thin layers with a given initial amplitude of $\delta^{18}O$ are smoothed faster than thick layers with the same initial amplitude. Therefore one could argue that A is a proxy for accumulation rate rather than for continentality. In the firn layer (top 30 m on Lomonosovfonna) diffusion is very fast because of vapor transport, and therefore amplitudes decay rapidly in this layer. Solid ice diffusion is a much slower process than firn diffusion. The modeled amplitudes would change only about 5% between the bottom of the firn layer (defined as the depth were pores are closed off from the atmosphere) and AD1600 (using diffusion rates from *Johnsen et al.* [2000]), and so solid ice diffusion can be ignored. Thin ice layers formed during melt/refreeze events will act as vapor barriers and limit firn diffusion. To ensure we are below the effect of vapor transport, we restrict ourselves to the record below 30 m. That means we can reasonably assume that there is very little trend in the characteristic diffusion length scale in this part of the core, though there will be local variability (e.g., due to ice layers).

[13] Previous studies on Lomonosovfonna have found that percolation lengths are generally shorter than the annual layer thickness [*Pohjola et al.*, 2002a] except during the warmest years (such as post-1990) where percolation length

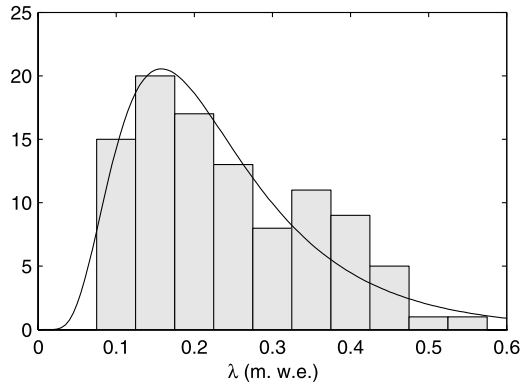

Figure 1. Histogram of layer thickness from 25 to 37 m (i.e., near pore close off) and the lognormal fit used in the modeling.

appear to be 2–8 annual layers [*Kekonen et al.*, 2005]. From snow pit studies carried out in May 2002 on Lomonosovfonna we find that the annual isotopic range prior to melt is approximately 10‰. We consider now the scenario where a fraction of the summer snowmelts, percolates and then refreezes in the winter snow. Prior to melt we assume that $\delta^{18}O_{summer} = -10‰$ and $\delta^{18}O_{winter} = -20‰$. Isotopic fractionation is observed to occur during freezing of ice, where an isotopic gradient will form in the ice layer because the first ice that forms will be relatively enriched in $H_2^{18}O$ because of Rayleigh fractionation [e.g., *Hubbard and Sharp*, 1993]. The ice will be ~3‰ heavier than the water it freezes from. The same effect is not seen during melting and the meltwater has the same isotopic content as the summer snow ($\delta^{18}O_{water} = -10‰$) because the ice in individual crystals is effectively unmixed. The refrozen meltwater will therefore have average $\delta^{18}O$ of −10‰ with the heaviest fraction having −7‰. However, it will have been mixed with a fraction of winter snow. In the case where the refrozen layer composition originates from one third meltwater and two thirds winter snow (equivalent to ~50% SMI) the resulting layer will have mean $\delta^{18}O_{refrozen} = -16.7‰$ with the heaviest being −15.7‰. The net effect is that the annual isotopic range will have been reduced from 10‰ to ~6‰ because of percolation, which compares well with the isotopic values in the upper firn pack on Lomonosovfonna [*Pohjola et al.*, 2002a]. However, thin ice layers will not cause any significant smoothing and could even inhibit firn diffusion. For this reason we may expect that the amplitudes respond nonlinearly to SMI. Surface melt will generally dampen the signal whereas limited melt inhibits smoothing by firn diffusion. Observational data (Figure 4) will be discussed later.

3.1.2. Accumulation Rate Effects on Amplitudes

[14] Rather than attempting the difficult back diffusion problem, which is sensitive to small errors in diffusion length, we argue that a statistical mean over several years will minimize the integrated effects of diffusion. That is, we will assume that adequate time smoothing will give a record that is close to proportional to the annual amplitude in freshly precipitated snow (A_0). To test this assumption, we will apply a mathematical diffusion model to an artificial record of amplitudes with realistically distributed layer thickness. From this we will give an estimate of how much of the total variance in A is due to diffusion processes and so how much smoothing is needed. We define σ as the characteristic diffusion length scale [*Johnsen et al.*, 2000]. The observed layer thickness (λ) has a wide distribution (Figure 1), varying by a factor of 5 or more, while variations in σ due to ice layers are, we argue, much smaller; we will return to this point later. The ratio λ/σ, which measures the annual layer scale to the diffusion length scale, will be dominated by changes in λ and we will assume a constant σ in the development that follows.

[15] The net effect of diffusion is equivalent to convoluting the deposited signal with a Gaussian filter having a standard deviation σ (which is also the diffusion length), [*Johnsen et al.*, 2000]. Using the Fourier convolution theorem, the power spectral density of the isotopic profile is then

$$P(F) = P_0(F)e^{-(2\pi F\sigma)^2}, \tag{1}$$

where F is the frequency and P_0 is the spectral density of the initial deposited $\delta^{18}O$ profile, which is, however, compressed by layer thinning with depth due to ice flow. We will estimate P_0 from the near surface layers and then estimate σ by fitting equation (1) to the measured P from a section of the profile just below pore close off. If we assume that the isotopes are deposited with a red noise (AR1) background spectrum with lag-1 autocorrelation α, we can write

$$P_{surf}(F) = 2Vdz\frac{1-\alpha^2}{|1-\alpha e^{-2i\pi Fdz}|^2}, \tag{2}$$

where dz is the sampling resolution and V is the variance of the deposited signal [*Torrence and Compo*, 1998]. We will use water equivalent (w.e.) depth units to minimize layer thinning with depth, and therefore be less sensitive to precise determination of pore close off depth. We estimate the deposited signal to have $\alpha = 0.85$ from the top 4 m w.e. of the core, sampled at a resolution of 0.03 m w.e. At depth, the background spectrum will have been both whitened because of compression and reddened because of diffusion. We assume that P_0 is proportional to P_{surf} with the frequency axis stretched to account for thinner layers at depth. We can then write $P_0(F) = cP_{surf}(rF)$, where r accounts for spectrum whitening and c represents the difference in isotopic variance between the present and at depth. We determine the diffusion length by fitting equation (1) (with an additional white measurement noise term) to the observed power spectrum using the maximum entropy method [*Chen*, 1988]. The measurement noise is estimated to have a standard deviation of 0.06‰ from the high-frequency variability of the oldest and most diffused ice. This is consistent with an estimated measurement precision of ±0.1‰ based on analysis of replica samples. In Figure 2 the diffusion length has been determined through minimizing the mean absolute deviation of the theoretical spectrum to the observed in a moving window and has then been decompressed to pore close off level. The variation in diffusion length observed in

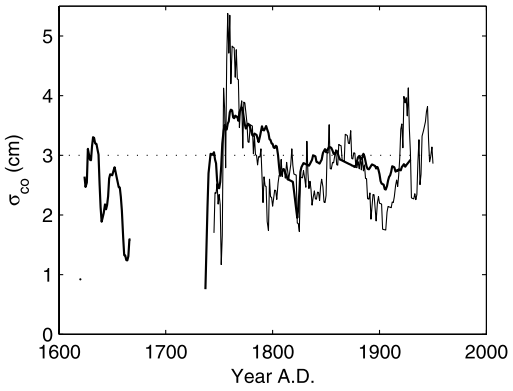

Figure 2. Best fitting diffusion length decompressed to pore close-off level, obtained by minimizing the mean absolute deviation between the theoretical power spectrum (equation (1)) and the low-order maximum entropy power spectrum estimated in 15 year (thin line) and 60 year (thick line) windows. The curve based on 15 year windows is cut off at 1740 because there are too few samples in the window to accurately estimate the power spectrum. Similarly, the gap near 1700 is due to discontinuous sampling. The variability in σ_{co} increases back in time as the number of samples in the window decreases and as compression makes it problematic to resolve the diffusion length with the given sampling resolution. This suggests that the variability reflects fitting uncertainty rather than a climate signal.

Figure 2 increases back in time and does not correlate with SMI nor is there any hint of a nonlinear relationship in a scatterplot. Therefore the variation is more likely caused by uncertainties in the estimated spectrum due to too few samples in the short window or because compression makes it harder to resolve the diffusion length with the given sampling resolution, rather than actual variations in diffusion length. The fact that there is practically no trend in the diffusion length provides justification for the assumption that solid ice diffusion can be ignored.

[16] As a consequence of equation (1), the amplitude of the annual signal can be written as

$$A = A_0 e^{-2\left(\pi\frac{\sigma}{\lambda}\right)^2}, \tag{3}$$

where A_0 is the initial amplitude and λ is the compressed layer thickness. Measured λ [*Pohjola et al.*, 2002b] is close to lognormally distributed (Figure 1). The $\log_{10}(\lambda)$ has mean -0.67 and standard deviation 0.22 at pore close off. Using these statistics, we generate a long surrogate time series of λ and calculate how a diffusion length $\sigma = 0.030$ m w.e. affects the amplitudes. The result can be seen in Figure 3. At 30 m depth, A has on average decayed to 61% of the deposited A_0, but its distribution is very wide. Table 1 shows that 5% of the layers will have decayed to less than 13% of the initial value, while another 5% of layers only decayed by 7%. However, taking 15 year moving averages of A tightens the distribution significantly (Figure 3). The proportion of variance (W) in A due to variation in λ can be estimated as

$$W = \frac{\overline{A}^2 \mathrm{var}\left(e^{-2\left(\pi\frac{\sigma}{\lambda}\right)^2}\right)}{\mathrm{var}(A)}, \tag{4}$$

where $\overline{A}$ is the mean value of A around pore close off. Using the variances from Table 1, we find that with 5 and 15 year moving averages only 11% and 7% of the total variance in A is due to variations in λ, so we can say that A is nearly proportional to A_0. That is, adequate time smoothing will give a statistically representative sampling of both thin and thick layers. In a similar fashion we determine that a 25% change in σ causes a $\sim$10% change in amplitudes. Our hypothesis is therefore that smoothed A on Lomonosovfonna reflects real seasonal changes in $\delta^{18}O$ influenced by melt rather than changes in accumulation rate or diffusion length. We will test this hypothesis in the results section.

3.1.3. Amplitude Reconstruction

[17] To derive the annual amplitudes record, we first upsampled the isotope record to 10 samples per year, and then high-pass filtered it with a cutoff wavelength of 3 years. The amplitude was then measured as the range in a window 1 year wide from the modeled timescale [*Kekonen et al.*, 2005]. This processing can be carried out beyond the limits of layer counting because measuring the amplitude is substantially easier than counting the layers. Even if this procedure misses a peak and picks the one from a neighboring year, the amplitude will still be a reasonable estimate. We tested our results by varying the window length and the high-pass-filtering method, and found them to be robust.

[18] The amplitudes decay as the yearly layer thickness is compressed by ice flow, eventually to a thickness comparable with the 5 cm sampling resolution of $\delta^{18}O$. The effect of the sampling is equivalent to convoluting the "true"

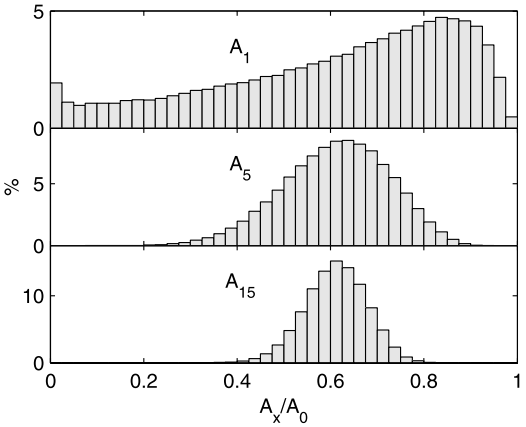

Figure 3. (top) Histogram of modeled annual amplitudes at pore close off relative to deposited amplitudes assuming a diffusion length of 3.0 cm w.e. (middle and bottom) Using 5 and 15 year moving averages (middle and bottom) tightens and normalizes the distribution significantly.

Table 1. Percentiles and Variance of Modeled Annual Isotopic Amplitudes (Equation (3)) After Firn Diffusion Relative to Their Deposited Amplitudes Assuming That the Layer Thickness is Lognormally Distributed[a]

	Percentile			
	5%	50%	95%	Variance
A/A_0	0.12	0.67	0.93	0.066
A_5/A_0	0.42	0.62	0.78	0.013
A_{15}/A_0	0.51	0.62	0.72	0.005

[a] A_5 and A_{15} denote 5 and 15 year moving averages, respectively.

signal with a rectangle function. Hence, using the Fourier convolution theorem, we correct the amplitudes by applying

$$A_{corrected} = \frac{A_{measured}}{\mathrm{sinc}\left(\pi \frac{\Delta z}{\lambda}\right)} \quad (5)$$

where Δz is the width of a sample and λ is the local wavelength of the annual signal. At 1700 the correction factor is 1.3, while at 1600 the factor we apply is 1.6. Somewhat arbitrarily, we decide that beyond 1600 the errors in the correction factor are too big to extract a meaningful signal.

3.2. Chemical Washout Index

[19] Many studies have found that particular ions are preferentially washed out of the ice during seasonal melt [e.g., *Davies et al.*, 1982; *Iizuka et al.*, 2002]. However, details of specific ion elution rates depend on the incorporation of ions in the ice during grain growth and so are certainly affected by processes that occur prior to the onset of melting [*Cragin et al.*, 1996]. While microphysical processes governing the removal of ions are poorly understood, it is reasonable to assume that the ions are removed fractionally as the melt progresses, and so we can write

$$\frac{\partial C}{\partial W} = -a \cdot C \text{ and } C(0) = C_p \Leftrightarrow C(W) = C_p \cdot e^{-aW}, \quad (6)$$

where W is a dimensionless washout index, C is the concentration of a chemical species, a is a species-specific dimensionless washout rate and C_p is the species initial concentration in the fresh snow. Here we have implicitly assumed that the reservoir volume for the ions is constant; that is, the increase in concentration due to a reduced volume caused by runoff is negligible, which is different from the situation in a seasonal snowpack.

[20] Some chemical ions have the same principle source. For example, both Na^+ and Mg^{2+} are mainly of sea salt origin in Svalbard snow [*Virkkunen*, 2004; *Iizuka et al.*, 2002], and so their concentrations are often taken to be linearly dependent. If we define X and Y to be the concentrations of two such chemical species, then $X_p = k_{xy}Y_p$, where X_p and Y_p are the concentrations of X and Y prior to melt, and k_{XY} is their ratio in fresh snow. From equation (6) it is clear that the logarithmic ratio of the concentrations after washout is linear in W.

$$\log\left(\frac{X}{Y}\right) = \log\left(\frac{X_p \cdot e^{-a_X W}}{Y_p \cdot e^{-a_Y W}}\right) = \log(k_{XY}) + (a_Y - a_X)W. \quad (7)$$

[21] Hence we can derive a washout index provided that the washout rates a_X and a_Y differ significantly. Note that equation (7) holds even for a finite reservoir that is depleted during the melt season, as happens with significant runoff. *Iizuka et al.* [2002] show that there are high correlations (>0.95) between the concentrations of Na^+, Cl^-, K^+ and Mg^{2+} in Svalbard dry snow from Austfonna. *Virkkunen* [2004] find similar results from Lomonosovfonna, indicating that these ions have the same (marine) source for Svalbard, justifying the use of equation (7). However, all these correlations break down in wet snow, except that between Na^+ and Cl^-. Hence the washout rates for Na^+, K^+ and Mg^{2+} must differ widely, whereas they are the similar for Na^+ and Cl^-. In particular, *Iizuka et al.* [2002] find that Mg^{2+} is washed out more efficiently than Na^+ ($a_{Mg} > a_{Na}$). Because of these differences in washout rates, we can construct two independent chemical melt indices W_{NaMg} and W_{ClK} based on $\log(Na^+/Mg^{2+})$ and $\log(Cl^-/K^+)$. We consider W_{NaMg} to be superior to W_{ClK} since relative measurement errors in K^+ are much larger than in Mg^{2+} [*Kekonen et al.*, 2002] and further K^+ has a tendency to have large peaks that are seemingly unrelated to other ions in high-resolution pit data [*Iizuka et al.*, 2002]. Using seawater ratios in μgL^{-1}, we get $k_{NaMg} = 8.3$ and $k_{ClK} = 49$. To avoid difficulties with percolation between layers [*Pohjola et al.*, 2002a; *Moore et al.*, 2005], we use 15 year mean concentrations. To compare W_{NaMg} and W_{ClK}, we scale the dimensionless indices by their mean values over the twentieth century.

4. Results

[22] We test the new indices by comparison with the instrumental record and proxy data. *Isaksson et al.* [2005b] compare the $\delta^{18}O$ profile with meteorological records from around the Barents Sea with Vardø on the Norwegian coast having the best correlation. However, the Vardø temperature record is longer than that from Longyearbyen, and therefore it is expected that it will correlate better simply because it covers the large increase in temperatures at the end of the Little Ice Age (LIA). Over the period of common overlap (1911–1997), $\delta^{18}O$ correlate better with Longyearbyen than Vardø temperatures. Therefore our interpretation is that Longyearbyen temperatures are more representative of the conditions on Lomonosovfonna than those from Vardø.

[23] Correlation coefficients between 5 year moving averages of ice core data and the historical records are shown in Table 2. As expected isotopes ($\delta^{18}O$) correlate significantly with Longyearbyen temperatures (T_m, T_{DJF}, T_{JJA}). To avoid the problems with firn diffusion completely, we should discard the continentality record above pore close off (e.g., younger than 1930). However, to test A against instrumental records we need a bigger overlap and so, as a compromise, we choose to truncate A at 1970 (15.6 m depth) by when most of the firn diffusion already has taken place. The more continental the climate conditions, the greater the temperature range with winter temperatures changing the most. So, as expected, the continentality proxy (A) correlates with temperature range (ΔT), while $\delta^{18}O$ anticorrelates (Table 2). On longer timescales we find that A is also highly anticorrelated with $\delta^{18}O$ (Table 3). This is consistent with the interpretation of $\delta^{18}O$ as a temperature proxy and A as a continentality proxy. We find no clear relationship between A and SMI (Figure 4) and we

Table 2. Significant Correlation Coefficients ($p < 0.05$) Between Ice Core Data and Historical Records for Their Overlapping Periods[a]

	$\delta^{18}O$	A	SMI	W_{NaMg}	W_{ClK}
T_m	0.47	−0.38			
T_{JJA}	0.52				
T_{DJF}	0.53	−0.48			
ΔT	−0.34	0.57			
B_w	−0.65		−0.22	−0.28	−0.60
B_e	−0.34		−0.34	−0.50	−0.32

[a]All records have been smoothed using 5 year moving averages, so as to make the results insensitive to dating errors. Ice core parameters: A, continentality; SMI, stratigraphic melt index; W_{xy}, chemical washout indices. Historical parameters: T, Longyearbyen temperature (mean, summer, winter, annual range); B, April sea ice extent in the western and eastern Barents Sea.

therefore conclude that melt is not a major contributor to the variability in *A*.

[24] Linear regression gives $T_m = 1.12\ \delta^{18}O + 11.5$ ($R^2 = 0.22$) and $\Delta T = 3.3\ A + 19.5$ ($R^2 = 0.32$), and both of these regressions are significant at the 95% level. However, *van de Wal et al.* [2002] analyzed the borehole temperature profile finding that temperatures in the nineteenth century were 2.4°C colder than the twentieth century, this compares with a 0.8 ‰ difference in $\delta^{18}O$ [*Isaksson et al.*, 2003] between the nineteenth and twentieth centuries. This indicates that the above regression underestimates the sensitivity of $\delta^{18}O$ on temperature, which is to be expected considering that the historical records used in the regression only cover the relatively warm twentieth-century period [*von Storch et al.*, 2004].

[25] The SMI does not correlate significantly with temperatures. We find that the full records of SMI and $\delta^{18}O$ are significantly anticorrelated (Table 3). Thus, if we believe $\delta^{18}O$ to be a temperature proxy, it does not seem plausible to consider SMI a summer temperature proxy. The alternative explanation of SMI as a continentality index can also be rejected since there is no significant correlation with *A* (Table 3 and Figure 4). Perhaps the SMI, for this ice core, is a composite signal that requires a more sophisticated treatment of percolation effects.

[26] Perhaps surprisingly, there is no significant correlation between washout indices and any temperature series (Table 2). However, there are significant correlations with $\delta^{18}O$. These can be explained by the local differences in conditions. The summit of Lomonosovfonna is inland and 1250 m asl, whereas Longyearbyen is within a fjord at sea level. In summer, warm days often produce foggy conditions near sea level, and sunny conditions at higher elevations, therefore we expect that the washout indices are recording local summer melt.

Table 3. Significant Correlation Coefficients ($p < 0.05$) for Lomonosovfonna Ice Core Data[a]

	$\delta^{18}O$	A	SMI	W_{NaMg}	W_{ClK}
$\delta^{18}O$		−0.66	−0.48	0.60	0.51
A	−0.59			−0.46	−0.46
SMI	−0.48			−0.16	−0.12
W_{NaMg}	0.60	−0.43	−0.16		0.73
W_{ClK}	0.51	−0.36	−0.12	0.73	

[a]Parameters are as in Table 2. All records have been smoothed using 15 year moving averages.

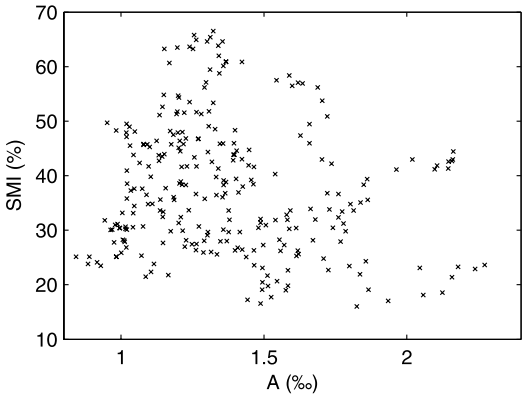

Figure 4. Scatterplot of annual amplitudes (A) against stratigraphic melt index (SMI) using 15 year moving averages (1700–1970). There is no simple relationship between melt and amplitudes. Scatter increases when using 5 year averages.

[27] It is noticeable that both washout indices have negative values throughout extensive periods (Figure 5). If, as seems reasonable, runoff is the only postdepositional process that can change 15 year averages of these ion ratios and given that runoff would act to make the indices more positive, negative values can only be explained by changing the ionic ratios of the precipitation. Either additional sources account for the excess Mg^{2+} and K^+ or fractionation processes deplete Na^+ and Cl^- relative to Mg^{2+} and K^+. Since there are simultaneous excesses of both Mg^{2+} and K^+ an additional source contributing to both ions, such as terrestrial dust (though it would need to be relatively depleted in Na^+), would produce changes in both washout rates. However, Table 2 shows that the washout rates are significantly inversely correlated with sea ice extent in the Barents Sea, which points toward fractionation processes as the most likely explanation. *Rankin et al.* [2002] proposed fractionation by frost flowers on sea ice to explain low ratios of SO_4^{2-} in Antarctic ice, but such depletion cannot be seen in the Arctic data because of the large magnitude of non-sea-salt SO_4^{2-} sources. However, the same mechanism could also remove NaCl from source aerosol. When winter temperatures drop below the NaCl eutectic (−22°C), frost flowers will be relatively enriched in ions that remain liquid at low temperatures, including Mg^{2+} and K^+. Direct evidence of depleted Na^+/Mg^{2+} and Na^+/K^+ ratios on sea ice have been found by *Domine et al.* [2004], though they suggest that an additional terrestrial source of K^+ and Mg^{2+} is involved. Two independent effects influence the ionic ratios: increased runoff raises the ratios, while increased sea ice lowers them. Thus low washout indices indicate a cold climate with relatively more sea ice. Consistently, we find that W_{NaMg} and W_{ClK} correlate with $\delta^{18}O$ and anticorrelate with *A* (Table 3).

5. Discussion

[28] The Lomonosovfonna $\delta^{18}O$ record indicates that the LIA in Svalbard ended around 1900 (Figure 5). The start of

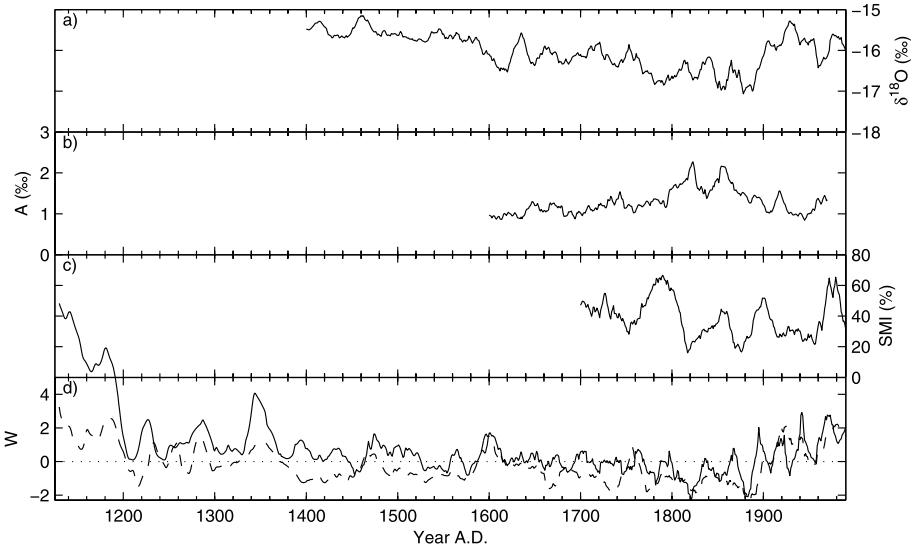

Figure 5. Fifteen-year moving averages of Lomonosovfonna ice core data. (a) Oxygen isotopes, (b) continentality proxy (A), (c) stratigraphic melt indices (SMI), and (d) washout indices (solid line is W_{NaMg}, and dashed line is W_{ClK}).

the LIA is less easy to define as there seems to be a gradual descent into colder climatic conditions. However, by 1600 a clear signature of the LIA is seen in the isotopes and chemistry [*Isaksson et al.*, 2003; *Kekonen et al.*, 2005], probably indicating that the sea ice margin had advanced close enough to Svalbard to affect local climate. Continentality and washout indices show more gradual changes. The coldest and most continental period seen in the core is the nineteenth century. For comparison, most western North American proxies also show the nineteenth century as the coldest period, whereas in European proxies the coldest period occurs between 1600 and 1700 [*Jones and Mann*, 2004]. Under the reasonable assumption that sea salt ions have the same source throughout the record, negative washout indices during the period from 1700 to 1900 are indicative of greater sea ice extent in the Barents Sea.

[29] The continentality proxy (A) peaks at 1860 and declines rapidly thereafter. This suggests that a change in climate was already setting in by 1870 and temperatures and sea ice extent lagged the continentality change by 30 years. However, continentality is most affected by winter temperatures, while sea ice extent is at a maximum in spring. Thus we suggest that winter temperatures rose several decades before spring and summer temperatures.

[30] In the oldest part of the core (1130–1200), the washout indices are more than 4 times as high as those seen during the last century, indicating a high degree of runoff. Since 1997 we have performed regular snow pit studies [*Virkkunen*, 2004], and the very warm 2001 summer resulted in similar loss of ions and washout ratios as the earliest part of the core. This suggests that the Medieval Warm Period [*Jones and Mann*, 2004] in Svalbard summer conditions were as warm (or warmer) as present-day, consistent with the Northern Hemisphere temperature reconstruction of *Moberg et al.* [2005].

6. Conclusion

[31] We hope that this paper inspires interest in using Arctic ice cores from smaller ice caps for reconstruction of Late Holocene environmental history on a regional scale. We have developed proxies for the washout intensity (W_{NaMg} and W_{ClK}) based on the ion ratios of sea salt ions (Na^+, Cl^-, Mg^{2+} and K^+) and continentality (A) based on annual amplitudes of $\delta^{18}O$. The washout indices can provide a valuable constraint on whether ion data truly represents precipitation chemistry or if runoff has affected the record. For Lomonosovfonna we find that sea ice extent also affects the washout indices, most likely because NaCl is fractionated relative to other salts in the source area. Luckily the sign of this fractionation is such that W_{NaMg} and W_{ClK} still can be thought of as proxies for summer temperatures. Washout indices confirm results from earlier studies [*Kekonen et al.*, 2005] showing that the ion chemistry in the earliest part of the core (before 1200) was dominated by washout of ions. We find that washout intensities are more than 4 times higher than the average over the last century.

[32] Annual amplitudes in $\delta^{18}O$ are affected by melt and diffusion in a nontrivial and likely nonlinear manner. In the case of Lomonosovfonna, the $\delta^{18}O$ record is subject to melt and percolation and therefore presumably also to highly anisotropic diffusion in the firn. Despite this, we show that amplitudes below the level of strongly active firn diffusion are a good proxy for continentality at Lomonosovfonna, if sufficiently smoothed. However, further studies on other cores are needed before amplitudes generally can be con-

sidered to be a proven proxy for continentality. The crucial step is to smooth the amplitude record sufficiently so that each value represents a statistical mean over several years minimizing variations in annual layer thickness. An important assumption is that the trends in diffusion length and accumulation rate are small compared with the width of the layer thickness distribution. If such trends are significant, their contribution to the total variation in A may be estimated using a straightforward modification of the model presented in this paper. Under some conditions one may argue that continentality is constant (e.g., Central Greenland over the Holocene) and A might be used to infer changes in diffusion length.

[33] On Lomonosovfonna we find that the end of the LIA is very well defined in $\delta^{18}O$ and agrees with the earliest rise in washout indices (W_{NaMg}, W_{ClK}) around 1880. The Continentality proxy (A), however, starts to decline after 1860. We suggest that the response of spring and summer temperatures and the decline in sea ice in the Barents Sea lagged the rise in winter temperatures by several decades.

[34] **Acknowledgments.** The drilling of the Lomonosovfonna 1997 ice core was financed by the Norwegian Polar Institute and the Institute for Marine and Atmospheric Research, Utrecht (IMAU), and we wish to thank the field party. Additional funding was provided by the Thule Institute, Nessling Foundation, Swedish Science Council, Norwegian Research Council, NARP, and Stiftelsen Ymer-80. Finally, the anonymous referees provided very helpful comments.

References

Bolzan, J. F., and V. A. Pohjola (2000), Reconstruction of the undiffused seasonal oxygen isotope signal in central Greenland ice cores, *J. Geophys. Res.*, *105*(C9), 22,095–22,106.

Chen, C. H. (1988), *Signal Processing Handbook*, CRC Press, Boca Raton, Fla.

Cragin, J. H., A. D. Hewitt, and S. C. Colbeck (1996), Grain-scale mechanisms influencing the elution of ions form snow, *Atmos. Environ.*, *30*, 119–127.

Dansgaard, W. (1964), Stable isotopes in precipitation, *Tellus*, *16*, 436–468.

Davies, T. D., C. E. Vincent, and P. Brimblecombe (1982), Preferential elution of strong acids from a Norwegian ice cap, *Nature*, *300*(5888), 161–163.

Domine, F., R. Sparapani, A. Ianniello, and H. J. Beine (2004), The origin of sea salt in snow on Arctic sea ice and in coastal regions, *Atmos. Chem. Phys.*, *4*, 2259–2271.

Hubbard, B., and M. Sharp (1993), Weertman regelation, multiple refreezing events and the isotopic evolution of the basal ice layer, *J. Glaciol.*, *39*(132), 275–291.

Iizuka, Y., M. Igarashi, K. Kamiyama, H. Motoyama, and O. Watanabe (2002), Ratios of Mg^{2+}/Na^{+} in snowpack and an ice core at Austfonna ice cap, Svalbard, as an indicator of seasonal melting, *J. Glaciol.*, *48*(162), 452–460.

Isaksson, E., et al. (2001), A new ice core record from Lomonosovfonna, Svalbard: Viewing the data between 1920–1997 in relation to present climate and environmental conditions, *J. Glaciol.*, *47*(157), 335–345.

Isaksson, E., et al. (2003), Ice cores from Svalbard: Useful archives of past climate and pollution history, *Phys. Chem. Earth*, *28*, 1217–1228.

Isaksson, E., D. Divine, J. Kohler, T. Martma, V. Pohjola, H. Motoyama, and O. Watanabe (2005a), Climate oscillations as recorded in Svalbard ice core $\delta^{18}O$ records between 1200–1997 AD, *Geogr. Ann., Ser. A*, *87*(1), 203–214.

Isaksson, E., J. Kohler, J. Moore, V. Pohjola, M. Igarashi, L. Karlöf, T. Martma, H. A. J. Meijer, H. Motoyama, and R. S. W. van de Wal (2005b), Using two ice core $\delta^{18}O$ records from Svalbard to illustrate climate and sea ice variability over the last 400 years, *Holocene*, *15*(4), 501–509.

Johnsen, S. J., H. Clausen, K. Cuffey, G. Hoffmann, J. Schwander, and T. Creyts (2000), Diffusion of stable isotopes in polar firn and ice: The isotope effect in firn diffusion, in *Physics of Ice Core Records*, pp. 121–140, Hokkaido Univ. Press, Sapporo, Japan.

Jones, P. D., and M. E. Mann (2004), Climate over past millennia, *Rev. Geophys.*, *42*, RG2002, doi:10.1029/2003RG000143.

Kekonen, T., J. Moore, R. Mulvaney, E. Isaksson, V. Pohjola, and R. S. W. van de Wal (2002), An 800 year record of nitrate from the Lomonosovfonna ice core, Svalbard, *Ann. Glaciol.*, *35*, 261–265.

Kekonen, T., J. Moore, P. Perämäki, R. Mulvaney, E. Isaksson, V. Pohjola, and R. S. W. van de Wal (2005), The 800 year long ion record from the Lomonosovfonna (Svalbard) ice core, *J. Geophys. Res.*, *110*, D07304, doi:10.1029/2004JD005223.

Koerner, R. M. (1997), Some comments on climatic reconstructions from ice cores drilled in areas of high melt, *J. Glaciol.*, *43*(143), 90–97, (Correction, *J. Glaciol., 43* (144), 375–376, 1997.)

Moberg, A., D. M. Sonechkin, K. Holmgren, N. M. Datsenko, and W. Karlénm (2005), Highly variable Northern Hemisphere temperatures reconstructed from low- and high-resolution proxy data, *Nature*, *433*, 613–617, doi:10.1038/nature03265.

Moore, J. C., A. Grinsted, T. Kekonen, and V. Pohjola (2005), Separation of melting and environmental signals in an ice core with seasonal melt, *Geophys. Res. Lett.*, *32*, L10501, doi:10.1029/2005GL023039.

Nordli, P. Ø., I. Hanssen-Bauer, and E. J. Førland (1996), Homogeneity analyses of temperature and precipitation series from Svalbard and Jan Mayen, *DNMI-Klima Rep. 16/96*, Norw. Meteorol. Inst., Oslo.

Pfeffer, W. T., and N. F. Humphrey (1998), Formation of ice layers by infiltration and refreezing of meltwater, *Ann. Glaciol.*, *26*, 83–91.

Pohjola, V. A., J. C. Moore, E. Isaksson, T. Jauhiainen, R. S. W. van de Wal, T. Martma, H. A. J. Meijer, and R. Vaikmäe (2002a), Effect of periodic melting on geochemical and isotopic signals in an ice core from Lomonosovfonna, Svalbard, *J. Geophys. Res.*, *107*(D4), 4036, doi:10.1029/2000JD000149.

Pohjola, V. A., T. Martma, H. A. J. Meijer, J. C. Moore, E. Isaksson, R. Vaikmäe, and R. S. W. van de Wal (2002b), Reconstruction of 300 years annual accumulation rates based on the record of stable isotopes of water from Lomonosovfonna, Svalbard, *Ann. Glaciol.*, *35*, 57–62.

Rankin, A. M., E. W. Wolff, and S. Martin (2002), Frost flowers: Implications for tropospheric chemistry and ice core interpretation, *J. Geophys. Res.*, *107*(D23), 4683, doi:10.1029/2002JD002492.

Torrence, C., and G. P. Compo (1998), A practical guide to wavelet analysis, *Bull. Am. Meteorol. Soc.*, *79*, 61–78.

van de Wal, R. S. W., R. Mulvaney, E. Isaksson, J. C. Moore, J.-F. Pinglot, V. Pohjola, and M. P. A. Thomassen (2002), Reconstruction of the historical temperature trend from measurements in a medium-length bore hole on the Lomonosovfonna Plateau, Svalbard, *Ann. Glaciol.*, *35*, 371–378.

van Lipzig, N. P. M., E. van Meijgaard, and J. Oerlemans (2002), The effect of temporal variations in the surface mass balance and temperature-inversion strength on the interpretation of ice core signals, *J. Glaciol.*, *48*(163), 611–621.

Vinje, T. (2001), Anomalies and trends of sea ice extent and atmospheric circulation in the Nordic Seas during the period 1864–1998, *J. Clim.*, *14*(3), 255–267.

Virkkunen, K. (2004), Snowpit studies in 2001–2002 in Lomonosovfonna, Svalbard, M. S. thesis, 71 pp., Univ. of Oulu, Oulu, Finland.

von Storch, H., E. Zorita, J. M. Jones, Y. Dimitriev, F. González-Rouco, and S. F. B. Tett (2004), Reconstructing past climate from noisy data, *Science*, *306*(5696), 679–682, doi:10.1126/science.1096109.

A. Grinsted and J. C. Moore, Arctic Centre, University of Lapland, P. O. Box 122, FIN-96101 Rovaniemi, Finland. (ag@glaciology.net)

E. Isaksson, Norwegian Polar Institute, Polar Environmental Centre, N-9296, Tromsø, Norway.

T. Martma, Institute of Geology, Tallinn University of Technology, Estonia Av. 7, 10143 Tallinn, Estonia.

V. Pohjola, Department of Earth Sciences, Uppsala University, Villavägen 16, SE-752 36 Uppsala, Sweden.

IV

Observational evidence for volcanic impact on sea level and the global water cycle

A. Grinsted[1,2], J. C. Moore[1] & S. Jevrejeva[3]

1. Arctic Centre, University of Lapland, Rovaniemi, Finland

2. Department of Geophysics, University of Oulu, Oulu, Finland

3. Proudman Oceanographic Laboratory, Liverpool, UK

It has previously been noted that there are drops in global sea level (GSL) following some major volcanic eruptions[1,2]. However, observational evidence has not been convincing as there is substantial variability in the global sea level record on periods similar to those at which we expect volcanoes to have an impact[3]. To quantify the impact of volcanic eruptions we average monthly GSL data from 830 tide gauge records around 5 major volcanic eruptions. Surprisingly, we find that the initial response to a volcanic eruption is a significant rise in sea level of 9 mm in the first year after the eruption. This is followed by a drop of 7 mm in the period 2-3 years after the eruption relative to pre-eruption sea level. Neither the drop nor especially the rise in GSL can be explained by models of lower oceanic heat content[4,5]. The volcanic impact on the water cycle is comparable in magnitude to that of a large El Niño-La Niña cycle, amounting to about 5% of global land precipitation[6].

Major volcanic eruptions inject scattering aerosol into the stratosphere and thus impose a significant radiative cooling of the atmosphere[7]. In the years following major eruptions it has been observed that there is a drop in Global Oceanic Heat Content (GOHC)[5]. A colder ocean is denser and an associated drop in global mean sea level of ~5mm during the 1-4 years following a major eruption has been modelled[5]. *Stenchikov et al.*[8] found by modelling that large scale atmospheric circulation patterns such as the Arctic Oscillation (AO) were affected by the Pinatubo eruption. We have previously shown a link between AO and European sea level[3], which is best explained by a redistribution of water driven by shifts in surface air pressure.

Producing a GSL curve with valid confidence intervals from the observational data base is not a trivial job (See Supplementary Information). We use 830 time series of monthly mean relative sea level (RSL) from the Permanent Service for Mean Sea Level (PSMSL) database[9]. Detailed descriptions of these time series are available from www.pol.ac.uk/psmsl. We applied an inverted barometer correction to the records using sea level pressure from the HadSLP2 dataset[10], taking care to adjust the atmospheric pressure so that the over ocean pressure integral is constant. RSL data sets were corrected for local datum changes and glacial isostatic adjustment (GIA) of the solid Earth[11]. However, as we are interested in the transient response of GSL to volcanic eruptions we will be detrending GSL prior to analysis and therefore the choice of GIA corrections is not critical to this study. We have developed a new 'virtual station' method to overcome geographical bias, so that stations close to each other are weighted much less than isolated ones, and which can quantify the uncertainties due to the

representativeness of the stations used[12]. We assign each station to one of 13 regions (Fig. 1) and calculate the GSL from the average of the regional sea level rates. The reconstructed GSL will effectively be smoothed by 12 month averages due to the method used to avoid seasonal bias. The evolution and regional distribution of station numbers as well as a comparison with other GSL reconstructions[1,2,12] can be found in the Supplementary Information.

There are 9 eruptions since 1890 that produced a stratospheric aerosol loading at least ~10% as big as Pinatubo in 1991[7] (see Supplementary information). Only eruptions located in the tropics affect both hemispheres, and the 5 largest eruptions are all tropical, with only one of the 9 located at high latitudes[7]. The GSL curve shows considerable variability on periods comparable to the timescale at which we expect volcanoes to have an impact, and any significant change before and after a particular volcanic eruption could be argued to be caused by natural variability such as e.g. El Niño. We therefore examine the average impact from the 5 most recent major tropical volcanic eruptions (Colima, February 1890; Santa Maria, October 1902; Agung, March 1963; El Chichón, April 1982; Pinatubo, June 1991) which have been previously modelled to have an impact on GSL[5]. Since El Niño-Southern Oscillation has a large impact of sea level[3,12], especially in the tropics[7], it is fortunate that these eruptions occurred in both El Niño and La Niña years, so that the volcanic signal is maximized at the expense of non-volcanic variability. The average detrended GSL can be seen in Fig. 2. The qualitative shape of Fig. 2 (the initial peak followed by a drop) is robust to excluding any particular volcano from the analysis. The curves for the individual eruptions, and an alternative method of calculating average impact using 9 volcanic eruptions may be seen in the Supplementary Information. The GSL response is not dominated by the signal in any single region (See Supplementary Table 4). The detrended GSL curve is far from spectrally white (the coefficient of a first order auto-regressive, AR(1)=0.98) and conventional tests overestimate the significance. For that reason, we test the significance of the main features seen in the plot by Monte Carlo sampling of the detrended GSL series using 5 random dates instead of the real eruption years. That is when testing whether the median sea level in two windows (i.e. the centre line of the boxplots in Fig. 2) are significantly different, we find the distribution of the absolute median difference from 10000 window pairs (with same length and separation). This gives a conservative estimate of the significance because the detrended GSL series presumably contains some volcanic variability.

The observed average response to the eruptions is an initial rise in GSL in the first year followed by a drop in the period 2-4 years after the eruption (Fig. 2). GSL reaches background levels ~5 years after an eruption. The maximal rise of 9 mm occurs 4 months after the eruption which coincides with the timing of the maximal radiative forcing[7], and the maximal drop of 7 mm occurs after 32 months. In order to asses the significance of the rise and drop, we compare the median GSL of windows representing pre-eruption GSL (0-2 years before eruption), the rise (the first year post eruption), and the drop (2-3 years post eruption). We label these 3 windows Before, Rise, and Drop (Fig. 2). We find that the median Before-Rise difference is significant at the 99% confidence level, whereas the Before-Drop difference is only significant at the 81% level. The Drop appears less significant as it is well separated from the Before period. The Rise to Drop median difference is significant at the 99% level. The Rise and Drop

characteristics are robust and not dominated by any particular region or volcanic eruption.

The timing of the largest drop in GSL ~3 years after the eruption agrees with modelling and observations of GOHC[4,13], however its magnitude of ~7 mm is about 40% larger than modelled[5]. Furthermore, we unexpectedly find a significant rise of ~9 mm in GSL in the first year immediately following an eruption. These differences between modelled and observed volcanic impact on sea level suggests that, in addition to lowering the GOHC, major volcanic eruptions affect both ocean volume and mass. Mass changes in the oceans may be mediated by variation in glacier mass balance, river discharge, and precipitation-evaporation (P-E)[14].

Volcanic eruptions reduce atmospheric water vapour[15]. In particular, Pinatubo caused a decrease of only ~0.5 mm[15] and the ~9 mm peak in GSL can therefore not be explained by drying of the atmosphere. There is both observational and modelling evidence for less precipitation over land after volcanic eruptions[7,16]. This reduction in precipitation has previously been tied to reduced evaporation[5,7]. We propose that the initial peak and the larger than expected drop in sea level, may be explained by lower evaporation from the oceans and a delayed response of river discharge to the associated lower precipitation. The volcanic radiative forcing will have an immediate cooling effect at the ocean surface. Oceanic evaporation rate is strongly determined by ocean skin temperature[17], although mixing dilutes the temperature anomalies, and we expect evaporation to closely track the radiative forcing. The observed peak in sea level occurs 4 months after the eruption, which agrees well with the timing of the maximal radiative forcing after a large eruption[7]. In contrast, a steric drop in sea level would be caused by a reduced GOHC and would largely depend on the integrated radiative forcing and hence be delayed and of longer duration[18]. The observation that GSL first rises and then drops thus agrees with our hypothesis. To summarize, initially there is lower ocean evaporation but river discharge does not respond immediately to the consequent lower precipitation and therefore sea level rises. After 1 to 2 years P-E returns to normal, but river discharge is now relatively low due to the reduced land precipitation in the preceding years. Additionally the global cooling caused by the eruption reduces runoff from ice masses – effectively lowering sea level. In addition to this transient response of the water cycle there is the steric drop in GSL that may persist for many years[18,5]. This hypothesis is consistent with the observation (see Supplementary Information) that the initial rise in sea level is especially evident in regions where the steric change is relatively small, such as in the Baltic and Northeast Pacific[19,20].

The magnitude of the impact on the water cycle may be seen by comparison with natural changes in global river discharge[21] where a 5% change corresponds to a change in GSL of 5.5mm yr^{-1}. The initial 9 mm rise in sea level is equivalent to a 2.5% change in global lake and river reservoirs[22]. This rise corresponds to an imbalance in ocean surface water fluxes of ~0.02 mm/day for a year, which translates into a reduction in land P-E of ~0.06 mm/day or ~3% of mean land precipitation. This is in the range of modelled natural variability[23]. The magnitude of this change is similar to the ~4% variations in global land precipitation associated with El Niño-Southern Oscillation[6]. The volcanic induced changes in water cycle may, depending on relative timing, act in

opposite sense to those that occur in a normal El Niño-La Niña cycle, thus supporting observations that the El Niño coincident with eruptions of El Chichón (1982/3) and Pinatubo (1991/2) were rather atypical in their oceanic precipitation/temperature behaviour[6,7]. The respective roles that heat content, evaporation, and inter-oceanic redistribution of water play in the regional response of sea level need further study. The proposed mechanism for the initial rise in sea level can be tested by modelling the volcanic impact on ocean evaporation, ocean precipitation, and river discharge.

<received> Style tag for received and accepted dates (omit if these are unknown).

1. Church, J. A., White, N. J., Coleman, R., Lambeck, K. & Mitrovica, J. X. Estimates of the regional distribution of sea-level rise over the 1950 to 2000 period. *J. Clim.* 17, 2609–-2625 (2004).

2. Church, J. A., & White N. J. A 20th century acceleration in global sea-level rise, *Geophys. Res. Lett.*, **33**, L01602, doi:10.1029.2005GL024826 (2006)

3. Jevrejeva, S., Moore, J. C., Woodworth P.L. & Grinsted A. Influence of large-scale atmospheric circulation on European sea level: results based on the wavelet transform method, *Tellus* **57A**, 183–193 (2005).

4. Hansen, J., et al. Climate forcings in Goddard Institute for Space Studies SI2000 simulations, *J. Geophys. Res.*, **107**, 4347, doi:10.1029.2001JD001143 (2002).

5. Church, J. A., White, N. J. & Arblaster, J. M. Significant decadal-scale impact of volcanic eruptions on sea level and ocean heat content. *Nature* **438**, doi:10.1038.nature04237 (2005)

6. Adler, B.F., et al. The Version 2 Global Precipitation Climatology Project (GPCP) Monthly Precipitation Analysis (1979-Present). *J. Hydrometeorol.* **4**, 1147–1167, (2003).

7. Robock, A. Volcanic eruptions and climate. *Rev. Geophys.* **38**, 191-219 (2000).

8. Stenchikov, G. et al. Arctic Oscillation response to the 1991 Mount Pinatubo eruption: Effects of volcanic aerosols and ozone depletion, *J. Geophys. Res.*, **107**, 4803, doi:10.1029.2002JD002090 (2002).

9. Woodworth, P.L. & Player R. The Permanent Service for Mean Sea Level: an update to the 21st century, *J. Coastal Res.,* **19**, 287-295 (2003).

10. Allan, R. J. & Ansell, T. J. A new globally complete monthly historical mean sea level pressure data set (HadSLP2): 1850-2004, *J. Clim.,* accepted, (2006).

11. Peltier, W.R. Global glacial isostasy and the surface of the ice-age earth: The ICE-5G model and GRACE, *Ann. Rev. Earth Planet. Sci.*, **32**, 111-149 (2004).

12. Jevrejeva, S., A. Grinsted, J. C. Moore, and S. Holgate, Nonlinear trends and multiyear cycles in sea level records, J. Geophys. Res., 111, C09012, doi:10.1029/2005JC003229 (2006).

13. Levitus, S., Antonov, J. & Boyer T. Warming of the world ocean, 1955–2003, *Geophys. Res. Lett.*, **32**, L02604, doi:10.1029/2004GL021592 (2005).

14. Cazenave, A. & Nerem R. S. Present-day sea level change: Observations and causes, *Rev. Geophys.*, **42**, RG3001, doi:10.1029.2003RG000139 (2004).

15. Soden, B. J., R. T. Wetherald, G. L. Stenchikov, and A. Robock: Global cooling following the eruption of Mt. Pinatubo: A test of climate feedback by water vapor. *Science*, **296**, 727–730 (2002).

16. Gillett, N. P., Weaver, A. J., Zwiers, F. W. & Wehner M. F. Detection of volcanic influence on global precipitation, *Geophys. Res. Lett.*, **31**, L12217, doi:10.1029.2004GL020044 (2004).

17. Thomas, G. E. & Stamnes, K. *Radiative transfer in the atmosphere and ocean*. Cambridge Univ. Press, New York. 517 pp, Ch.1, 27-28. (1999).

18. Gleckler, P., T. Wigley, B. Santer, J. Gregory, K. AchutaRao, and K. Taylor (2006). Volcanoes and climate: Krakatoa's signature persists in the ocean. *Nature*, **439**, doi:10.1038/439675a. (2006)

19. Antonov, J.I., Levitus, S. & Boyer T. P. Thermosteric sea level rise, 1955–2003 *Geophys. Res. Lett* **32**, L12602, doi:10.1029.2005GL023112 (2005).

20. Cabanes, C., Cazenave, A. & Le Provost C. Sea Level Rise During Past 40 Years Determined from Satellite and in Situ Observations, *Science*, 294(5543), 840-842 (2001).

21. Fekete, B. M., Vörösmarty, C. J. & Grabs W. Global, Composite Runoff Fields Based on Observed River Discharge and Simulated Water Balances (Report No. 22, GRDC, Koblenz, Germany, 2nd ed.) (1999).

22. Gleick, P. H.: Water resources. In Encyclopedia of Climate and Weather, ed. by S. H. Schneider, Oxford University Press, New York, vol. 2, pp.817-823 (1996).

23. Broccoli, A. J., et al. Twentieth-century temperature and precipitation trends in ensemble climate simulations including natural and anthropogenic forcing, *J. Geophys. Res.*, **108**, 4798, doi:10.1029.2003JD003812 (2003).

Supplementary Information is linked to the online version of the paper at www.nature.com/nature

Acknowledgements Funding was provided by the Thule institute, the Maj and Tor Nessling foundation, and the Finnish Academy.

Author Information Reprints and permissions information is available at npg.nature.com/reprintsandpermissions. The authors declare no competing financial interests. Correspondence and requests for materials should be addressed to A.G. (ag@glaciology.net).

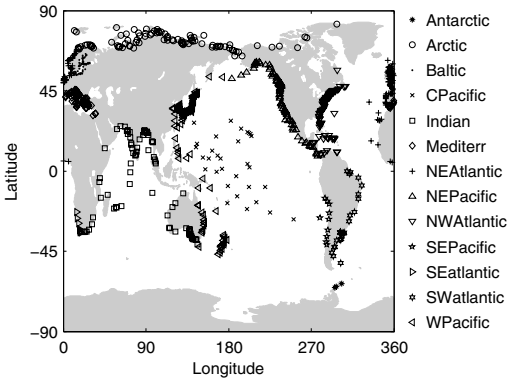

Figure 1. Location of tide gauges and their distribution into 13 regions. Symbols indicate the designated region.

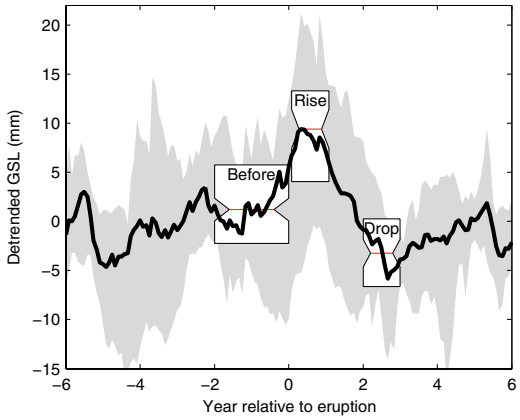

Figure 2. Average impact of 5 major volcanoes on sea level. The solid black curve shows non-linearly detrended (See Ref. 12 and Supplementary Information) GSL as observed in tide gauge records (grey shows range of values). Boxplots show the median sea level (centre line of box) of the “Before”, “Rise” and “Drop” windows which we compare in the text. Notches show the 95% confidence interval of the median, top and bottom edges of each box are the 25th and 75th percentiles and the full range can be seen from the grey shaded area.

Observational evidence for volcanic impact on sea level and the global water cycle

A. Grinsted[1,2], J. C. Moore[1] & S. Jevrejeva[3]

1. Arctic Centre, University of Lapland, Rovaniemi, Finland

2. Department of Geophysics, University of Oulu, Oulu, Finland

3. Proudman Oceanographic Laboratory, Liverpool, UK

It has previously been noted that there are drops in global sea level (GSL) following some major volcanic eruptions[1,2]. However, observational evidence has not been convincing as there is substantial variability in the global sea level record on periods similar to those at which we expect volcanoes to have an impact[3]. To quantify the impact of volcanic eruptions we average monthly GSL data from 830 tide gauge records around 5 major volcanic eruptions. Surprisingly, we find that the initial response to a volcanic eruption is a significant rise in sea level of 9 mm in the first year after the eruption. This is followed by a drop of 7 mm in the period 2-3 years after the eruption relative to pre-eruption sea level. Neither the drop nor especially the rise in GSL can be explained by models of lower oceanic heat content[4,5]. The volcanic impact on the water cycle is comparable in magnitude to that of a large El Niño-La Niña cycle, amounting to about 5% of global land precipitation[6].

Major volcanic eruptions inject scattering aerosol into the stratosphere and thus impose a significant radiative cooling of the atmosphere[7]. In the years following major eruptions it has been observed that there is a drop in Global Oceanic Heat Content (GOHC)[5]. A colder ocean is denser and an associated drop in global mean sea level of ~5mm during the 1-4 years following a major eruption has been modelled[5]. *Stenchikov et al.*[8] found by modelling that large scale atmospheric circulation patterns such as the Arctic Oscillation (AO) were affected by the Pinatubo eruption. We have previously shown a link between AO and European sea level[3], which is best explained by a redistribution of water driven by shifts in surface air pressure.

Producing a GSL curve with valid confidence intervals from the observational data base is not a trivial job (See Supplementary Information). We use 830 time series of monthly mean relative sea level (RSL) from the Permanent Service for Mean Sea Level (PSMSL) database[9]. Detailed descriptions of these time series are available from www.pol.ac.uk/psmsl. We applied an inverted barometer correction to the records using sea level pressure from the HadSLP2 dataset[10], taking care to adjust the atmospheric pressure so that the over ocean pressure integral is constant. RSL data sets were corrected for local datum changes and glacial isostatic adjustment (GIA) of the solid Earth[11]. However, as we are interested in the transient response of GSL to volcanic eruptions we will be detrending GSL prior to analysis and therefore the choice of GIA corrections is not critical to this study. We have developed a new 'virtual station' method to overcome geographical bias, so that stations close to each other are weighted much less than isolated ones, and which can quantify the uncertainties due to the

representativeness of the stations used[12]. We assign each station to one of 13 regions (Fig. 1) and calculate the GSL from the average of the regional sea level rates. The reconstructed GSL will effectively be smoothed by 12 month averages due to the method used to avoid seasonal bias. The evolution and regional distribution of station numbers as well as a comparison with other GSL reconstructions[1,2,12] can be found in the Supplementary Information.

There are 9 eruptions since 1890 that produced a stratospheric aerosol loading at least ~10% as big as Pinatubo in 1991[7] (see Supplementary information). Only eruptions located in the tropics affect both hemispheres, and the 5 largest eruptions are all tropical, with only one of the 9 located at high latitudes[7]. The GSL curve shows considerable variability on periods comparable to the timescale at which we expect volcanoes to have an impact, and any significant change before and after a particular volcanic eruption could be argued to be caused by natural variability such as e.g. El Niño. We therefore examine the average impact from the 5 most recent major tropical volcanic eruptions (Colima, February 1890; Santa Maria, October 1902; Agung, March 1963; El Chichón, April 1982; Pinatubo, June 1991) which have been previously modelled to have an impact on GSL[5]. Since El Niño-Southern Oscillation has a large impact of sea level[3,12], especially in the tropics[7], it is fortunate that these eruptions occurred in both El Niño and La Niña years, so that the volcanic signal is maximized at the expense of non-volcanic variability. The average detrended GSL can be seen in Fig. 2. The qualitative shape of Fig. 2 (the initial peak followed by a drop) is robust to excluding any particular volcano from the analysis. The curves for the individual eruptions, and an alternative method of calculating average impact using 9 volcanic eruptions may be seen in the Supplementary Information. The GSL response is not dominated by the signal in any single region (See Supplementary Table 4). The detrended GSL curve is far from spectrally white (the coefficient of a first order auto-regressive, AR(1)=0.98) and conventional tests overestimate the significance. For that reason, we test the significance of the main features seen in the plot by Monte Carlo sampling of the detrended GSL series using 5 random dates instead of the real eruption years. That is when testing whether the median sea level in two windows (i.e. the centre line of the boxplots in Fig. 2) are significantly different, we find the distribution of the absolute median difference from 10000 window pairs (with same length and separation). This gives a conservative estimate of the significance because the detrended GSL series presumably contains some volcanic variability.

The observed average response to the eruptions is an initial rise in GSL in the first year followed by a drop in the period 2-4 years after the eruption (Fig. 2). GSL reaches background levels ~5 years after an eruption. The maximal rise of 9 mm occurs 4 months after the eruption which coincides with the timing of the maximal radiative forcing[7], and the maximal drop of 7 mm occurs after 32 months. In order to asses the significance of the rise and drop, we compare the median GSL of windows representing pre-eruption GSL (0-2 years before eruption), the rise (the first year post eruption), and the drop (2-3 years post eruption). We label these 3 windows Before, Rise, and Drop (Fig. 2). We find that the median Before-Rise difference is significant at the 99% confidence level, whereas the Before-Drop difference is only significant at the 81% level. The Drop appears less significant as it is well separated from the Before period. The Rise to Drop median difference is significant at the 99% level. The Rise and Drop

characteristics are robust and not dominated by any particular region or volcanic eruption.

The timing of the largest drop in GSL ~3 years after the eruption agrees with modelling and observations of GOHC[4,13], however its magnitude of ~7 mm is about 40% larger than modelled[5]. Furthermore, we unexpectedly find a significant rise of ~9 mm in GSL in the first year immediately following an eruption. These differences between modelled and observed volcanic impact on sea level suggests that, in addition to lowering the GOHC, major volcanic eruptions affect both ocean volume and mass. Mass changes in the oceans may be mediated by variation in glacier mass balance, river discharge, and precipitation-evaporation (P-E)[14].

Volcanic eruptions reduce atmospheric water vapour[15]. In particular, Pinatubo caused a decrease of only ~0.5 mm[15] and the ~9 mm peak in GSL can therefore not be explained by drying of the atmosphere. There is both observational and modelling evidence for less precipitation over land after volcanic eruptions[7,16]. This reduction in precipitation has previously been tied to reduced evaporation[5,7]. We propose that the initial peak and the larger than expected drop in sea level, may be explained by lower evaporation from the oceans and a delayed response of river discharge to the associated lower precipitation. The volcanic radiative forcing will have an immediate cooling effect at the ocean surface. Oceanic evaporation rate is strongly determined by ocean skin temperature[17], although mixing dilutes the temperature anomalies, and we expect evaporation to closely track the radiative forcing. The observed peak in sea level occurs 4 months after the eruption, which agrees well with the timing of the maximal radiative forcing after a large eruption[7]. In contrast, a steric drop in sea level would be caused by a reduced GOHC and would largely depend on the integrated radiative forcing and hence be delayed and of longer duration[18]. The observation that GSL first rises and then drops thus agrees with our hypothesis. To summarize, initially there is lower ocean evaporation but river discharge does not respond immediately to the consequent lower precipitation and therefore sea level rises. After 1 to 2 years P-E returns to normal, but river discharge is now relatively low due to the reduced land precipitation in the preceding years. Additionally the global cooling caused by the eruption reduces runoff from ice masses – effectively lowering sea level. In addition to this transient response of the water cycle there is the steric drop in GSL that may persist for many years[18,5]. This hypothesis is consistent with the observation (see Supplementary Information) that the initial rise in sea level is especially evident in regions where the steric change is relatively small, such as in the Baltic and Northeast Pacific[19,20].

The magnitude of the impact on the water cycle may be seen by comparison with natural changes in global river discharge[21] where a 5% change corresponds to a change in GSL of 5.5mm yr^{-1}. The initial 9 mm rise in sea level is equivalent to a 2.5% change in global lake and river reservoirs[22]. This rise corresponds to an imbalance in ocean surface water fluxes of ~0.02 mm/day for a year, which translates into a reduction in land P-E of ~0.06 mm/day or ~3% of mean land precipitation. This is in the range of modelled natural variability[23]. The magnitude of this change is similar to the ~4% variations in global land precipitation associated with El Niño-Southern Oscillation[6]. The volcanic induced changes in water cycle may, depending on relative timing, act in

opposite sense to those that occur in a normal El Niño-La Niña cycle, thus supporting observations that the El Niño coincident with eruptions of El Chichón (1982/3) and Pinatubo (1991/2) were rather atypical in their oceanic precipitation/temperature behaviour[6,7]. The respective roles that heat content, evaporation, and inter-oceanic redistribution of water play in the regional response of sea level need further study. The proposed mechanism for the initial rise in sea level can be tested by modelling the volcanic impact on ocean evaporation, ocean precipitation, and river discharge.

<received> Style tag for received and accepted dates (omit if these are unknown).

1. Church, J. A., White, N. J., Coleman, R., Lambeck, K. & Mitrovica, J. X. Estimates of the regional distribution of sea-level rise over the 1950 to 2000 period. *J. Clim.* 17, 2609–-2625 (2004).

2. Church, J. A., & White N. J. A 20th century acceleration in global sea-level rise, *Geophys. Res. Lett.*, **33**, L01602, doi:10.1029.2005GL024826 (2006)

3. Jevrejeva, S., Moore, J. C., Woodworth P.L. & Grinsted A. Influence of large-scale atmospheric circulation on European sea level: results based on the wavelet transform method, *Tellus* **57A**, 183–193 (2005).

4. Hansen, J., et al. Climate forcings in Goddard Institute for Space Studies SI2000 simulations, *J. Geophys. Res.*, **107**, 4347, doi:10.1029.2001JD001143 (2002).

5. Church, J. A., White, N. J. & Arblaster, J. M. Significant decadal-scale impact of volcanic eruptions on sea level and ocean heat content. *Nature* **438**, doi:10.1038.nature04237 (2005)

6. Adler, B.F., et al. The Version 2 Global Precipitation Climatology Project (GPCP) Monthly Precipitation Analysis (1979-Present). *J. Hydrometeorol.* **4**, 1147–1167, (2003).

7. Robock, A. Volcanic eruptions and climate. *Rev. Geophys.* **38**, 191-219 (2000).

8. Stenchikov, G. et al. Arctic Oscillation response to the 1991 Mount Pinatubo eruption: Effects of volcanic aerosols and ozone depletion, *J. Geophys. Res.*, **107**, 4803, doi:10.1029.2002JD002090 (2002).

9. Woodworth, P.L. & Player R. The Permanent Service for Mean Sea Level: an update to the 21st century, *J. Coastal Res.,* **19**, 287-295 (2003).

10. Allan, R. J. & Ansell, T. J. A new globally complete monthly historical mean sea level pressure data set (HadSLP2): 1850-2004, *J. Clim.,* accepted, (2006).

11. Peltier, W.R. Global glacial isostasy and the surface of the ice-age earth: The ICE-5G model and GRACE, *Ann. Rev. Earth Planet. Sci.*, **32**, 111-149 (2004).

12. Jevrejeva, S., A. Grinsted, J. C. Moore, and S. Holgate, Nonlinear trends and multiyear cycles in sea level records, J. Geophys. Res., 111, C09012, doi:10.1029/2005JC003229 (2006).

13. Levitus, S., Antonov, J. & Boyer T. Warming of the world ocean, 1955–2003, *Geophys. Res. Lett.*, **32**, L02604, doi:10.1029/2004GL021592 (2005).

14. Cazenave, A. & Nerem R. S. Present-day sea level change: Observations and causes, *Rev. Geophys.*, **42**, RG3001, doi:10.1029.2003RG000139 (2004).

15. Soden, B. J., R. T. Wetherald, G. L. Stenchikov, and A. Robock: Global cooling following the eruption of Mt. Pinatubo: A test of climate feedback by water vapor. *Science*, **296**, 727–730 (2002).

16. Gillett, N. P., Weaver, A. J., Zwiers, F. W. & Wehner M. F. Detection of volcanic influence on global precipitation, *Geophys. Res. Lett.*, **31**, L12217, doi:10.1029.2004GL020044 (2004).

17. Thomas, G. E. & Stamnes, K. *Radiative transfer in the atmosphere and ocean*. Cambridge Univ. Press, New York. 517 pp, Ch.1, 27-28. (1999).

18. Gleckler, P., T. Wigley, B. Santer, J. Gregory, K. AchutaRao, and K. Taylor (2006). Volcanoes and climate: Krakatoa's signature persists in the ocean. *Nature*, **439**, doi:10.1038/439675a. (2006)

19. Antonov, J.I., Levitus, S. & Boyer T. P. Thermosteric sea level rise, 1955–2003 *Geophys. Res. Lett* **32**, L12602, doi:10.1029.2005GL023112 (2005).

20. Cabanes, C., Cazenave, A. & Le Provost C. Sea Level Rise During Past 40 Years Determined from Satellite and in Situ Observations, *Science*, 294(5543), 840-842 (2001).

21. Fekete, B. M., Vörösmarty, C. J. & Grabs W. Global, Composite Runoff Fields Based on Observed River Discharge and Simulated Water Balances (Report No. 22, GRDC, Koblenz, Germany, 2nd ed.) (1999).

22. Gleick, P. H.: Water resources. In Encyclopedia of Climate and Weather, ed. by S. H. Schneider, Oxford University Press, New York, vol. 2, pp.817-823 (1996).

23. Broccoli, A. J., et al. Twentieth-century temperature and precipitation trends in ensemble climate simulations including natural and anthropogenic forcing, *J. Geophys. Res.*, **108**, 4798, doi:10.1029.2003JD003812 (2003).

Supplementary Information is linked to the online version of the paper at www.nature.com/nature

Acknowledgements Funding was provided by the Thule institute, the Maj and Tor Nessling foundation, and the Finnish Academy.

Author Information Reprints and permissions information is available at npg.nature.com/reprintsandpermissions. The authors declare no competing financial interests. Correspondence and requests for materials should be addressed to A.G. (ag@glaciology.net).

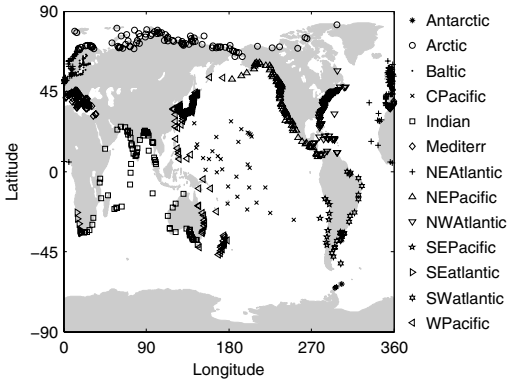

Figure 1. Location of tide gauges and their distribution into 13 regions. Symbols indicate the designated region.

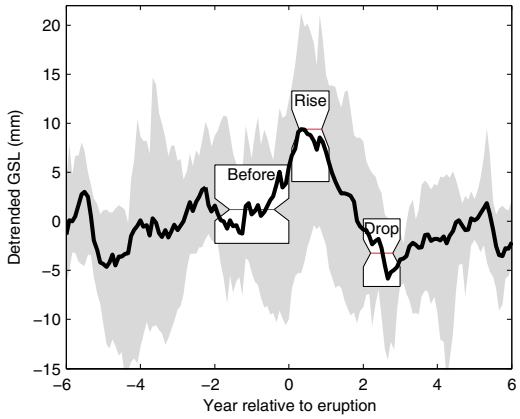

Figure 2. Average impact of 5 major volcanoes on sea level. The solid black curve shows non-linearly detrended (See Ref. 12 and Supplementary Information) GSL as observed in tide gauge records (grey shows range of values). Boxplots show the median sea level (centre line of box) of the “Before”, “Rise” and “Drop” windows which we compare in the text. Notches show the 95% confidence interval of the median, top and bottom edges of each box are the 25th and 75th percentiles and the full range can be seen from the grey shaded area.

V

Instruments and Methods

Singular spectrum analysis and envelope detection: methods of enhancing the utility of ground-penetrating radar data

John C. MOORE, Aslak GRINSTED

Arctic Centre, University of Lapland, Box 122, FIN-96101 Rovaniemi, Finland
E-mail: jmoore@ulapland.fi

ABSTRACT. We present a novel method of improving signal-to-noise ratio in radargrams. The method uses singular spectrum analysis (SSA) to separate each individual radar trace into orthogonal components. The components that explain most of the original trace variance contain mainly physically meaningful signal, while the components with little variance tend to be noise. Adding the largest-magnitude components together until the sum of components accounts for the variance above the noise level (typically 60–80%) of the original trace variance results in a much cleaner radargram with more easily seen internal features than in traditionally filtered data. The radargrams can be further enhanced by envelope-detecting the SSA-filtered data, as this measure of instantaneous energy minimizes the deleterious effects of innumerable phase changes at dielectric boundaries. Subsequent incoherent stacking results in far more structured radargrams than are achieved with traditionally processed radar data and amplitude stacking.

INTRODUCTION

Ground-penetrating radar (GPR) is a very widely used glaciological tool. Commonly GPRs are impulse radars that operate between a few MHz and 1 GHz (e.g. Sinisalo and others, 2003). Lower frequencies give greater penetration but lower resolution, while higher frequencies gain resolution at the expense of much less penetration (e.g. Watts and England, 1976). Frequently it is not simply the depth to bed that is of primary interest, but the internal reflections present in the ice (e.g. Miners and others, 1998; Eisen and others, 2003; Sinisalo and others, 2003). These reflections are usually much weaker than the bed reflector, and usually require more processing power and effort to recover. The vast amount of data usually collected during surveys is seldom exploited beyond the standard output available from fairly elementary qualitative processing and interpretation software such as Radan (Geophysical Survey Systems Inc.) or Haescan (Roadscanners Oy). In glaciological research there are frequently prohibitive logistical difficulties in returning to a particular glacier to collect additional data that may aid interpretation. Therefore it is worth going to more trouble than would be the case in a commercial survey to extract the maximum glaciological information from existing radar data. Typically, radar data processed with commercial packages, which are aimed more at the commercial user than at the researcher, are often manipulated in ways that are not easy to understand as the software source code is private. This severely limits the additional processing researchers can do on the output from the commercial software.

Here we present a simple method that is easily programmed (e.g. in Matlab™), and which can be used on data in a complementary way to commercial software, either on raw data or on output that has been manipulated by other software.

METHODS

Singular spectrum analysis (SSA) was developed as a means of analyzing time series (Allen and Smith, 1996; Ghil and others, 2002). The method is particularly suited to short, noisy time series such as those often found in palaeoclimate datasets. An individual radar trace spans the moment the radar transmitter antenna is triggered to the end of the time period that contains useful reflections. These radar traces are typically only about 1 μs in length, yet they can be analyzed by any time-series method. The method we describe is not a spectral technique; it operates in the time domain, and as such is suited to time series containing quasi-periodic signals, rather than strict sinusoids. This is the situation with a radar trace produced by reflections of the transmitted wavelet from the virtually infinite number of subtle dielectric boundaries in a real glacier. The recorded trace contains a continuously varying power spectrum as the radar waveform is modified over its propagation path through the glacier by the constantly changing ice dielectric properties. This is the case in polar ice, despite density contrasts being rather smooth, as the dielectric constant of firn changes by a factor two in the upper 100 m of the ice sheet due to density increase alone. Thus, accurate modelling of radar traces in Antarctica requires a time-domain finite-difference solution (e.g. Miners and other, 1998; Eisen and others, 2003). In temperate or polythermal glaciers, where melt layers cause rapid changes in density and dielectric properties, the radar wavelet changes even more dramatically with depth. This means that simple frequency filtering is unlikely to be a good way of increasing the signal-to-noise ratio, and in our experience it seldom clarifies radargrams.

We decompose each of the radar trace time series using SSA (Allen and Smith, 1996) with a set of data-adaptive, orthogonal filters. SSA amplifies signal-to-noise ratio by separating the original time series into low-frequency trends

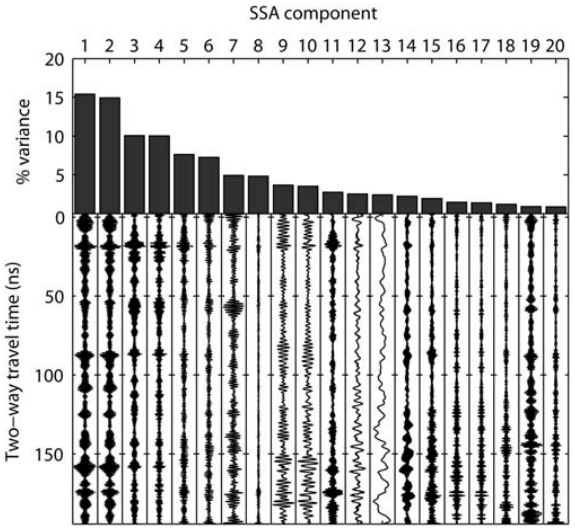

Fig. 1. SSA reconstructed components found by projecting the SSA filters found using the whole 2000 traces in Figure 4, on trace number 1, ordered by magnitude of variance accounted for in the radar trace. The noise floor we estimate as being after the first six components, which accounts for 63% of variance.

and narrowband quasi-periodic signals, with the rest (assumed to be noise) distributed among the filters. The number of orthogonal filters used is called the embedding dimension and is an important parameter in SSA. SSA operates by examining the dynamics of a complex system using the time-lagging method (e.g. Abarbanel, 1996). In this method the only information on the dynamics of the system comes from a time series of observations, in this case the voltages on the receiver antenna. A phase space that will approximate the dynamics of the system is constructed from the coordinates of the original time series and delayed copies of it. Each copy is delayed by a different integer multiple of time known as the lag. The lag is often, as it is here, the time interval between successive samples in the time series. The total number of time-series copies defines the embedding dimension. The smaller the embedding space, the shorter the length of the window over which the resolved components are calculated, and the less resolved is each component. The longer the window, the greater the frequency resolution of each component, but the greater the chance that noise is mistaken for signal and a greater proportion of the time series is affected by the data boundaries. The embedding dimension also determines the low-frequency limit below which oscillations will appear as trends (Moore and others, 2005). In typical time-series analysis we would calculate the statistical significance of individual components by testing the variance explained by the component against suitable noise models using Monte Carlo methods. The Monte Carlo methods are much the slowest computational part of the procedure; however, in the case of radar data we do not need to do this as we have many time series available and the significance of signals can be directly assessed by the observer.

The set of incrementally time-lagged radar traces make up the lagged-data matrix, representing the dynamical phase space. The basic idea behind SSA is to linearly transform the highly correlated set of vectors in the lagged-data matrix into a set of vectors that are linearly independent. The dependence of the lagged data can be expressed in terms of the covariance matrix (C) of the lagged-data matrix. The eigenvectors (p_k, $k = 1 \ldots M$) of C are the principal directions in the data matrix and are often called empirical orthogonal functions (EOFs), where M is the embedding dimension. Principal components (PCs) are obtained by projecting the lagged-data matrix onto the eigenvectors. The eigenvalues (V_k) of C tell us how much variance is captured by each PC and the eigenvectors and eigenvalues are sorted by importance so that V_1 is largest. The PCs that capture little of the variance (low eigenvalues, V_k) can be considered noise. The original time series can be reconstructed from the full set of PCs and EOFs. This can be done so that the reconstructed series is a sum of a set of reconstructed components (RCs) where each RC is only derived from one PC and its associated EOF. Hence, it is possible to make a partial reconstruction of the time series where components that capture little variance and are thus thought to be noise can be excluded. We can write the reconstructed components as

$$R_k(t) = \frac{\rho_k(t) * \rho_k(-t) * X(t)}{M},$$

where * indicates convolution, t is time and X is the time series. For radar filtering, the eigenvectors can be derived from the lag covariance matrix either of the full radargram or on a trace-by-trace basis. Figure 1 shows the RCs found for a single radar trace, and the associated eigenvectors derived from the covariance matrix of 2000 radar traces.

A wise choice of embedding dimension can be made with a priori insight. However, our experience with radar data suggests this choice is not particularly critical as we are mainly interested in the noise reduction properties of SSA as opposed to examining the particular SSA RCs that may correspond with physically meaningful oscillations or trends in the radar data. As larger embedding dimensions carry a computational penalty and are affected more by the data boundaries, we use rather small values of M: typically a value of 20 or 30 is sufficient to perform adequately. We recommend that a wide range of M is experimented with to examine possible unwanted artefacts.

For radar data, we simply sum the reconstructed components that account for the fraction of the original time-series variance that is above the noise floor of the data. The noise floor can be found by plotting the magnitude of V_k as a function of their index k when ordered by magnitude (Fig. 1), or equivalently by considering the contribution to the variance of the original radar trace of the RCs. Often there will be rapid fall-off of V_k with k until a fairly stable level is reached. This stable level represents the noise floor, and the components at this level are then representing mainly noise. The variance accounted for by the number components above the noise floor is then used as the number of RCs to be used in the SSA filtering. Typically, in our experience, the useful signal is 60–80% of the total variance in the radar trace. Figure 1 exhibits two rapid drops in variance (after the first two components and after the third and fourth components), then there is a fairly gradual drop-off in variance accounted for by the RCs rather than a low-level plateau. This example presents a more

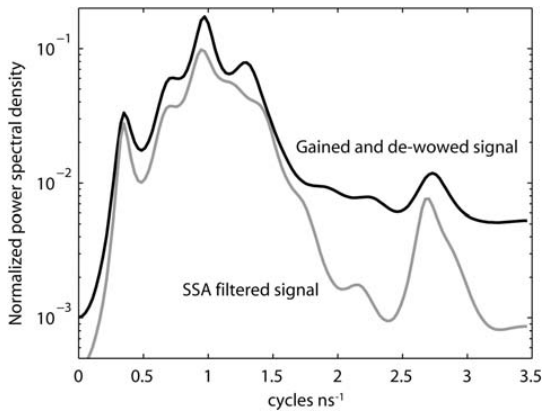

Fig. 2. The normalized power spectral density found using the maximum entropy method of order 20, for a block of 50 traces of radar data used to make one stacked trace in Figure 5. Note the peak in power at around 2.6 cycles ns^{-1} (2600 MHz) that is kept as signal by SSA that would very likely be rejected by bandpass-filtering the 800 MHz centre frequency radar data.

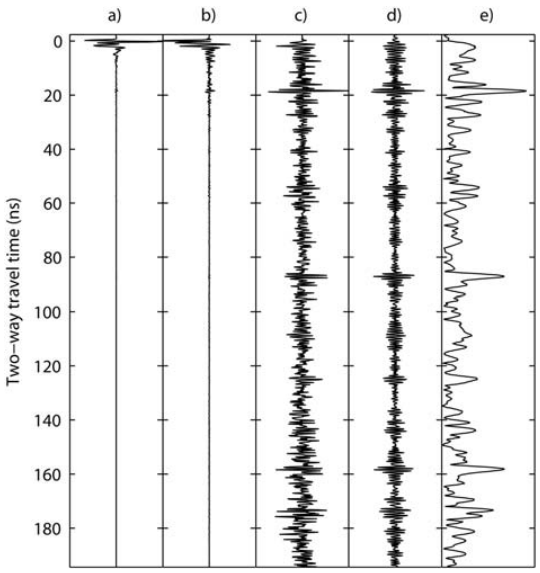

Fig. 3. The steps in the processing of radar trace No. 1000 in Figure 4. (a) The originally recorded radar trace; (b) after removal of the mean background trace; (c) simple linear gaining; (d) after removal of the noise SSA components; and (e) after envelope detection. Signal scaling is arbitrary.

difficult situation than arises when the noise floor is very clear, but there is still only a slow drop-off in variance accounted for beyond the sixth component. Here, we somewhat arbitrarily select six components as the cut-off of signal from noise, equivalent to accounting for a variance of 63%.

Removal of the non-linear trend component in SSA (e.g. Moore and others, 2005) corresponds with the 'd.c. removal' or 'de-wowing' processes usually done in radar processing, whereby the shift in reference voltage level and very long-period oscillations in each radar trace are removed. The SSA approach has the advantage of being a purely objective method of selecting parts of the received antenna voltage power spectrum that correspond with meaningful signals. A common method of attempting a similar process is to use bandpass filtering. However, particular SSA filters often correspond with rather narrowband quasi-period oscillations, and they can also come from anywhere in the full-frequency spectrum of the received radar trace rather than representing high- and low-pass limits. The difference between SSA and bandpass filtering can be seen by comparing the power spectrum of the amplified radar received data with the power spectrum of the SSA components that together comprise the reconstructed signal (Fig. 2).

ENVELOPE DETECTION STACKING

One common method of improving signal-to-noise ratio in radar is stacking. This method relies on coherent signals adding, while noise, being incoherent, rises only as the square root of the stacking number. This should occur where radar data are collected with the antennas stationary. Usually, however, radar data are collected while the antennas are continuously being moved over the snow surface. Thus stacking is done by averaging the radar traces collected over an appreciable distance of horizontal travel. When the radar frequencies used are high, and the dielectric properties of the firn and ice vary rapidly laterally, the assumption of coherence may fail. Since the bandwidth of impulse GPR is high, changes in dielectric layers, even of a few centimetres over distances between radar trace collection, (commonly some decimetres) can cause undesirable phase mismatching in stacking. In our experience, this often occurs, and stacking usually fails to bring significant improvement in signal-to-noise ratio.

Signal envelope detection (Nye and Berry, 1974) is a way of processing the data such that they can be stacked in an incoherent way, but which does significantly improve the signal-to-noise ratio. This method essentially squares and sums the real measured antenna voltage, and its quadrature, that is equivalent to the magnitude of the Hilbert transformation of the radar trace. In practice, this can be simply and very efficiently implemented by summing the squared radar trace data and their squared numerical differences, since the differential or integral of a sinusoid is just a phase shift of $\pi/2$. In some commercial processing packages, the magnitude of the Hilbert transformation is directly implemented. The envelope calculated represents the energy around the particular data point in the radar trace, so the envelope is not affected by the phase changes caused by the many dielectric discontinuities in the firn. Therefore small-scale lateral inhomogeneity that can undermine coherent stacking does not adversely affect the envelope-detected stack, and hence its usefulness for GPR data.

PRACTICAL EXAMPLES OF THE METHOD

Figure 3 shows all the steps in processing a radar trace that we use in the example radargrams discussed next.

To illustrate the advantages of the method we describe over normal processing, we show some radar data collected in Antarctica during December 1999 (Sinisalo and others, 2003). The first example is of a radar survey on Plogbreen,

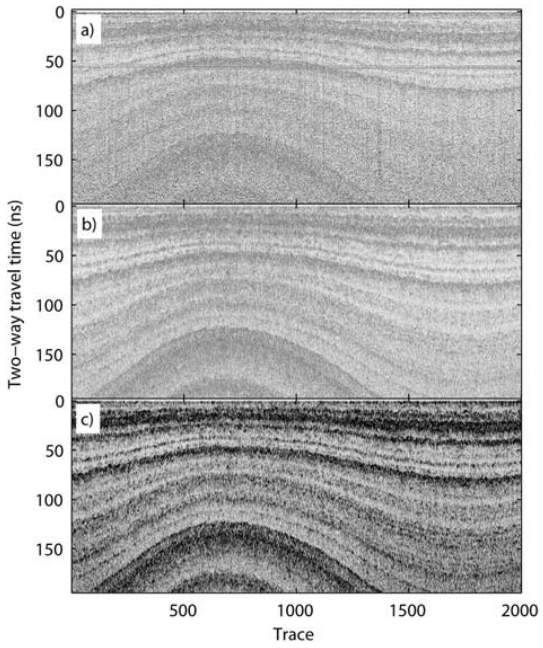

Fig. 4. (a) A profile of 800 MHz data from Antarctica (Sinisalo and others, 2003), that has had the mean background trace removed and linear gaining applied. (b, c) The same image after SSA-processing (b) and after envelope-detecting (c) the radar traces.

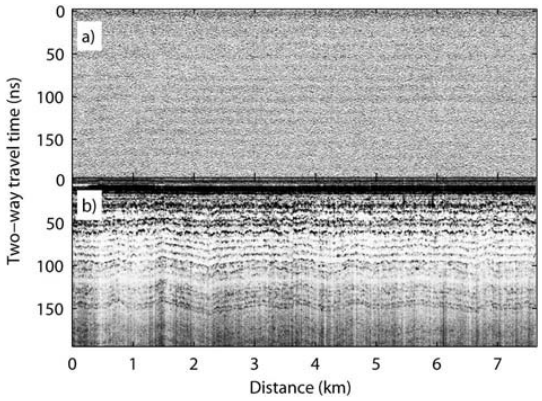

Fig. 5. (a) Radar data processed by background removal, d.c. removal, gaining, de-wowing and high-pass filtering, and stacking 50 times. (b) The same data processed by background removal, gaining, SSA filtering, envelope-detecting and stacking 50 times.

about 6 km from the Finnish research station Aboa (73°03′ S, 13°25′ W). The radar used was a Malå Geoscience Ramac system with an 800 MHz centre frequency shielded-antenna system. The radar control unit, computer and a roving global positioning system (GPS) receiver were mounted on the snowmobile. The antenna system was pulled about 2 m behind the snowmobile, using rigid struts to keep it at a fixed distance. No trace stacking was done and data were collected on a laptop computer. Each trace contains 1024 samples spanning a time window of 197 ns. Traces were collected at 0.25 s intervals, which correspond to horizontal distances of about 0.8 m at the snowmobile travelling speed. We reproduced, using Matlab™, the processing done by Sinisalo and others (2003). Background noise was removed and vertical bandpass filtering was performed. Figure 4 shows an example containing 2000 traces from the radar line, a distance of about 1600 m.

In our new method we do the same initial processing steps on each trace (see Fig. 3), but instead of the frequency filtering we perform SSA. As discussed above, we select an embedding dimension that is relatively short; here we use a value of 20. Figures 1 and 3 show the results of applying SSA to a single trace. The larger-magnitude reconstructed components in Figure 1 have clear changes in amplitude, as may be expected at an internal reflection horizon, but many of the lesser-magnitude components also possess that feature. We think that much more could be achieved by analyzing these components in more detail, as has been done with SSA quasi-periodic components in palaeoclimate time series, which reveal rich structure in the underlying climate system (e.g. Jevrejeva and others, 2004).

Figure 1 suggests that about 60–70% of the variance is above the noise floor and that the six largest reconstructed components amount to 63% of the original trace variance. We therefore extract the six leading RCs from all the 2000 traces in the section shown in Figure 4, to give the SSA-processed image in Figure 4b. There is clearly an enhancement in the SSA-processed image in Figure 4b relative to the normally processed data of Figure 4a. It is clear that the radar data contain eight to ten gently convex-up internal reflection bands, with hints of more detailed structure in places. In particular, there are reflecting layers in the deeper half-profile visible between traces 1500 and 2000 that are completely lost in the normally processed data. The layering is even more obvious in the envelope-detected image in Figure 4c.

It is of interest to consider the cause of the layer reflections. Sinisalo and others (2003) show that accumulation rates in the area are about 300 mm w.e. a^{-1}, and this would be about 500 mm of snow and firn in the upper layers. Given a radar wave velocity of 200 m μs^{-1}, 500 mm thick layers are about 5 ns of two-way travel time. Thus the layering is not simple annual layers, but more likely variation in densities due to the occasional melt events in the area.

The second example we consider examines the advantages of stacking GPR data. Again we consider 800 MHz Ramac radar data collected using the same set-up as described earlier. Each trace consisted of 1024 samples that were collected in a time window of 148 ns, with traces collected at 0.1 s intervals, which corresponds with three traces per metre. The data come from an area (74°34′ S, 10°43′ W) on Ritscherflya, about 15 km from the Swedish Svea station and near to the site of a Dutch automatic weather station. In total, 23 384 traces were collected, and we process the data as described earlier, but with 50 times stacking. SSA processing showed that about 80% of data were above the noise floor. The reconstructed components accounting for 80% of variance were summed and envelope-filtered and then stacked 50 times. Figure 5 shows the results: no layering can be seen in the normally processed and stacked radargram (Fig. 5a), while layers are quite easily seen in the SSA- and envelope-processed data (Fig. 5b). In this example, the envelope detection part of the processing is responsible for most of the improvement,

mainly because there was relatively little noise present in the radar data for SSA filtering to remove. Stacking was needed in this example to reveal layering because of the very small density differences present in the snow at this site. No seasonal melting occurs and wind speeds are high, ensuring considerable surface sastrugi and disturbance to annual layering. The layers are about 5 ns apart in Figure 5, suggesting that they, in contrast with the layers in Figure 4, probably represent annual stratification.

CONCLUSIONS

We present a novel method of processing radar data that should be especially well suited to impulse GPR systems. The SSA method is superior to common bandpass filtering approaches to improving signal-to-noise ratio in several ways: (1) an objective method of separating signal and noise components of the radar trace comes from analysis of the variance accounted for by the orthogonal reconstructed components; (2) SSA non-linear trend terms correspond with the separate 'd.c. level' and 'de-wowing' corrections commonly done to radar data; (3) the full power spectrum of the radar trace is available for analysis rather than arbitrarily setting bandpass filtering limits. The individual SSA reconstructed components also merit examination separately as they contain information on aspects of the complex system comprising the electromagnetic wave interaction with the dielectric medium of sub-parallel firn and ice layers.

We show that the GPR traces that have been 'envelope-detected' can be stacked much more successfully than can be done simply by amplitude stacking as a means of improving signal-to-noise ratio. This is because in high-bandwidth GPR data small lateral changes in the dielectric properties of firn layers cause phase shifts large enough to destroy coherent amplitude stacking in many practical surveys. Envelope detection is also unaffected by electromagnetic phase changes on reflection, as it is a measure of the instantaneous energy at particular times in the radar trace.

ACKNOWLEDGEMENTS

The field logistics in 1999–2002 were provided by the Finnish Antarctic Research Programme (FINNARP) 1999–2002, and we thank A. Sinisalo for help with radar data collection. The work was funded by the Finnish Academy and the Thule Institute. B. Hubbard and R. Pettersson provided helpful comments on the manuscript.

REFERENCES

Abarbanel, H.D.I. 1996. *Analysis of observed chaotic data*. New York, Springer.

Allen, M.R. and L.A. Smith. 1996. Monte Carlo SSA: detecting irregular oscillations in the presence of colored noise. *J. Climate,* **9**(12), 3373–3404.

Eisen, O., F. Wilhelms, U. Nixdorf and H. Miller. 2003. Revealing the nature of radar reflections in ice: DEP-based FDTD forward modeling. *Geophys. Res. Lett.,* **30**(5), 1218–1221.

Ghil, M. *and 10 others*. 2002. Advanced spectral methods for climatic time series. *Rev. Geophys.,* **40**(1), 1003. (10.1029/2000RG000092.)

Jevrejeva, S., J.C. Moore and A. Grinsted. 2004. Oceanic and atmospheric transport of multiyear El Niño–Southern Oscillation (ENSO) signatures to the polar regions. *Geophys. Res. Lett.,* **31**(24), L24210. (10.1029/2004GL020871.)

Miners, W.D., N. Blindow and S. Gerland. 1998. Modelling a GPR record by using ice core data to produce a synthetic radiogram. *In Proceedings of the Seventh International Conference on Ground-Penetrating Radar, May 27–30 1998, Lawrence, Kansas, USA*. Lawrence, KS, Radar Systems and Remote Sensing Laboratory, 437–442.

Moore, J.C., A. Grinsted and S. Jevrejeva. 2005. New tools for analyzing time series relationships and trends. *EOS Trans. AGU,* **86**(24), 226, 232.

Nye, J.F. and M. Berry. 1974. Dislocations in wave trains. *Proc. R. Soc. London A,* **336**, 165–190.

Sinisalo, A., A. Grinsted, J.C. Moore, E. Kärkäs and R. Pettersson. 2003. Snow-accumulation studies in Antarctica with ground-penetrating radar using 50, 100 and 800 MHz antenna frequencies. *Ann. Glaciol.,* **37**, 194–198.

Watts, R.D. and A.W. England. 1976. Radio-echo sounding of temperate glaciers: ice properties and sounder design criteria. *J. Glaciol.,* **17**(75), 39–48.

MS received 11 February 2005 and accepted in revised form 4 November 2005

VI

GEOPHYSICAL RESEARCH LETTERS, VOL. 33, L17705, doi:10.1029/2006GL026501, 2006

Is there evidence for sunspot forcing of climate at multi-year and decadal periods?

John Moore,[1] Aslak Grinsted,[1,2] and Svetlana Jevrejeva[3]

Received 4 April 2006; revised 21 June 2006; accepted 25 July 2006; published 2 September 2006.

[1] It has been proposed that solar cycle irradiance variations may affect the whole planet's climate via the stratosphere, the Quasi-Biennial Oscillation (QBO) and Arctic Oscillation (AO). We test this hypothesis by examining causal links between time series of sunspot number and indices of QBO, AO and ENSO activity. We use various methods: wavelet coherence, average mutual information, and mean phase coherence to study the phase dynamics of weakly interacting oscillating systems. All methods clearly show a cause and effect link between Southern Oscillation Index (SOI) and AO, but no link between AO and QBO or solar cycle over all scales from biannual to decadal. We conclude that the 11-year cycle sometimes seen in climate proxy records is unlikely to be driven by solar forcing, and most likely reflects other natural cycles of the climate system such as the 14-year cycle, or a harmonic combination of multi-year cycles. **Citation:** Moore, J., A. Grinsted, and S. Jevrejeva (2006), Is there evidence for sunspot forcing of climate at multi-year and decadal periods?, *Geophys. Res. Lett.*, *33*, L17705, doi:10.1029/2006GL026501.

1. Introduction

[2] There is considerable dispute as to the strength of the sun-climate link. Many proxy climatic time series exhibit significant power in the 11–14 year band, that several authors have been tempted to ascribe to solar sunspot cycles. However, detailed statistical analysis of many of these correlations shows them to be spurious or statistically insignificant [*Laut*, 2003; *Tsiropoula*, 2003]. Decadal cycles are fairly ubiquitous across the planet, and are therefore persuasive of a global-scale climate mechanism [*Jevrejeva et al.*, 2004]. Various mechanisms have been proposed to amplify the rather weak (0.1%) changes in solar energy output over an 11–12 year solar cycle to a level sufficient to produce changes in weather and climate. Several of these amplifying factors rely on the higher variability of solar energy at UV wavelengths to induce changes in stratospheric ozone and temperature, which can then propagate down to the troposphere [e.g., *Baldwin and Dunkerton*, 2005; *Labitzke*, 2005].

[3] The main features of the planet's climate are the ENSO and the polar annular modes. The strength of the polar stratospheric vortex determines the index of annular mode, which are called the Arctic Oscillation, (AO) and the Antarctic Annular Mode (AAM) [*Thompson and Wallace*, 1998]. The QBO (quasi-biennial oscillation) is a quasi-periodic oscillation of the equatorial zonal wind between easterlies and westerlies in the tropical stratosphere with a mean period of 28 months. Almost all plausible sun-climate links rely on modification of the polar stratosphere, usually with some mediation role being played by the QBO. *Labitzke* [2005] summarize the possible influence of solar cycle on QBO. *Kuroda and Shibata* [2005] modeled the impact of solar cycle on the AAM using a coupled chemistry-climate model in two 21-year long model runs with constantly repeating Sea Surface Temperature (SST). They found that increased ultra-violet radiation led to a more persistent signal from the AAM in the Antarctic stratosphere than during low UV model runs due to formation of an ozone anomaly (amounting to 2–3%). Furthermore they show that it is UV rather than cosmic rays that produce the difference in their model. *Barnston and Livezey* [1989], and later *Hameed and Lee* [2005] showed that stratospheric perturbations are more likely to penetrate to the troposphere during solar cycle maximum than minima, and that the effect is also dependent on the direction of the zonal wind direction in the tropics. However these analyses rely only on data available from 1948 and hence are not very statistically significant. *Kodera and Kuroda* [2002] interpreted reanalyses data from 1979 to 1998 and proposed a mechanism for the dynamical and radiative forcing of the stratosphere by the solar cycle, but there must be doubt to its statistical robustness as the data span less than two whole solar cycles. While it is clear that stratospheric anomalies can penetrate downwards to the troposphere, it is a rather atypical phenomena [*Baldwin and Dunkerton*, 1999, 2001], and in general the troposphere drives the stratosphere. *Mayr et al.* [2006] discuss a model simulation of the solar cycle and the QBO, and present evidence of a weak link, but their modeled solar cycle is fixed in period and amplitude. However, it is clear from both observational and modeling studies that the stratosphere can provide an efficient and fast transport mechanism for linking tropical and polar climate [*Baldwin and Dunkerton*, 2005; *Jevrejeva et al.*, 2004]. Thus the stratosphere provides a bridge between the annular modes and ENSO phenomena, and so we may expect it be one factor that it is especially sensitive to the solar cycle.

[4] In this paper we examine the plausibility of the argument that solar cycles are significant factors in climate on multi-year and decadal timescales. Causality relationships are analyzed using wavelet coherence methods. Wavelet coherence is useful as relative phase relationships between two time series across a wide spectrum of temporal scales are produced. If the variable represented by one of the time series is really the causal agent of the variability in the second time series, then a change in the first must always

[1] Arctic Centre, University of Lapland, Rovaniemi, Finland.
[2] Also at Department of Geophysics, University of Oulu, Oulu, Finland.
[3] Proudman Oceanographic Laboratory, Liverpool, UK.

0094-8276/06/2006GL026501$05.00

precede a reaction in the second. We firstly examine the link between the QBO and the AO to verify if there is a coherent relationship between these indices. Secondly we examine if there is a causal relationship between sunspot numbers and AO. Thirdly we test the mechanism that the solar cycle drives global climate via the polar regions by testing whether the arctic leads tropical climate in the solar cycle band.

2. Methods and Data

[5] We use monthly time series of the AO [*Thompson and Wallace*, 1998] and the QBO from http://www.cdc.noaa.gov/Correlation/qbo.data. ENSO time series comes from monthly SOI [*Ropelewski and Jones*, 1987], and the monthly Niño 3.4 SST index [*Smith and Reynolds*, 2004], defined as the monthly SST averaged over the eastern half of the tropical Pacific (5°S–5°N, 120°–170°W). We use the monthly International Sunspot numbers as the measure of the solar cycle (SC) available from http://sidc.oma.be/DATA/monthssn.dat, as accurate measurements of total and surface solar irradiance variations have been made for only 2–3 decades. We removed the mean monthly values (the annual cycle) from all series, and as the time series are all of different lengths, we restrict analyses to the common period of 1900–2000.

[6] The methods we use in this paper rely on applying the Continuous Wavelet Transform (CWT) to time series. Two useful wavelets are the Morlet, defined as

$$\psi_0(\eta) = \pi^{-1/4} e^{i\omega_0\eta} e^{-\frac{1}{2}\eta^2}, \tag{1}$$

and the Paul [*Torrence and Compo*, 1998]:

$$\psi_0(\eta) = \frac{2^m i^m m!}{\sqrt{\pi(2m)!}} (1 - i\eta)^{-(m+1)}, \tag{2}$$

where ω_0 is dimensionless frequency and η is dimensionless time, and m is the order, taken as 4 here. The idea behind the CWT is to apply the wavelet as a band pass filter to the time series. The wavelet is stretched in time, t, by varying its scale (s), so that $\eta = s{\cdot}t$, and normalizing it to have unit energy. The Morlet wavelet (with $\omega_0 = 6$) provides a good balance between time and frequency localization and is a good choice for feature extraction so will be used in the wavelet coherence analysis. For broad band pass filtering applications, we use the Paul as this is much less localized in frequency space. The CWT of a time series X, $\{x_n, n = 1, \ldots, N\}$ with uniform time steps δt, is defined as the convolution of x_n with the scaled and normalized wavelet.

$$W_n^X(s) = \sqrt{\frac{\delta t}{s}} \sum_{n'=1}^{N} x_{n'} \psi_0 \left[(n' - n) \frac{\delta t}{s} \right]. \tag{3}$$

The complex argument of $W_n^X(s)$ can be interpreted as the phases of $X\{\phi_1 \ldots, \phi_n\}$,

[7] Following *Grinsted et al.* [2004] we define the wavelet coherence of two time series X and $Y\{y_1, \ldots y_n\}$ as

$$R_n^2(s) = \frac{\left| S\left(s^{-1} W_n^{XY}(s)\right) \right|^2}{S\left(s^{-1} \left| W_n^X(s) \right|^2\right) \cdot S\left(s^{-1} \left| W_n^Y(s) \right|^2\right)}, \tag{4}$$

where S is a smoothing operator which is a Gaussian along the time axis and boxcar along the wavelet scale axis, and designed to fit the wavelet decorrelation length [*Grinsted et al.*, 2004]. Notice that the definition of wavelet coherence closely resembles that of a traditional correlation coefficient, and it is useful to think of it as a localized correlation coefficient in time frequency space. We apply significance testing using Monte Carlo methods using a red noise model based on the autocorrelation functions of the two time series [*Grinsted et al.*, 2004].

[8] The other methods we consider are non-linear interactions between the two time series that may be chaotic. Both these methods rely on the phase expression of the time series derived from (3) with the Paul wavelet (2) of the desired Fourier wavelength, $\lambda = 4\pi s/(2m + 1)$ [*Torrence and Compo*, 1998]. The broadband Paul wavelet allows signals that are relatively aperiodic to be included in the analysis, and it also makes the results we show very robust over a large range of λ. We utilize the average mutual information, $I(X, Y)$, between the two series, [e.g., *Papoulis*, 1984, chap. 15]. In our case we are interested in causative relations, so it is appropriate to measure the $I(X, Y)$, between their respective phases ϕ, and θ.

$$I(X, Y) = \frac{1}{\log_2 B} \sum_{y \in Y} \sum_{x \in X} p(\phi, \theta) \log_2 \frac{p(\phi, \theta)}{f(\phi) g(\theta)} \tag{5}$$

where p is the joint probability distribution function of X and Y, and f and g are the marginal probability distribution functions of X and Y respectively, I is normalized by B, the number of histogram bins used to construct f and g.

[9] Another measure of coherence between the two time series is the angle strength of the phase angle difference between the series, also known as the mean phase coherence, ρ [*Mokhov and Smirnov*, 2006]:

$$\rho = \frac{1}{N} \sqrt{\sum_{t=1}^{N} \cos^2(\phi_t - \theta_t) + \sum_{t=1}^{N} \sin^2(\phi_t - \theta_t)} \tag{6}$$

We can search for the optimum relative phase delay between the two series by lagging one time series relative to the other by a phase lag, Δ, in both (5) and (6).

3. Results

3.1. QBO-AO Relationship: Wavelet Coherence

[10] Figure 1 shows the wavelet coherence between the two time series. While both QBO and AO exhibit considerable power at biannual periods, there is no consistent phase relationship between the two series as clearly shown by the random orientations of the arrows in Figure 1. There is no evidence that supports the hypothesis that the strength of any relationship varies with the solar cycle, as even periods of significant coherence at biannual periods separated by a decade do not show any consistent phase relationship, e.g. the phase angle in 1960 was almost 180° different from that in 1970. There is also no evidence of any significant coherence in the solar cycle 11-year band.

3.2. Sunspot Numbers: Phase Coherence

[11] Having failed to establish any significant relationship between QBO and AO, we now assess if any other

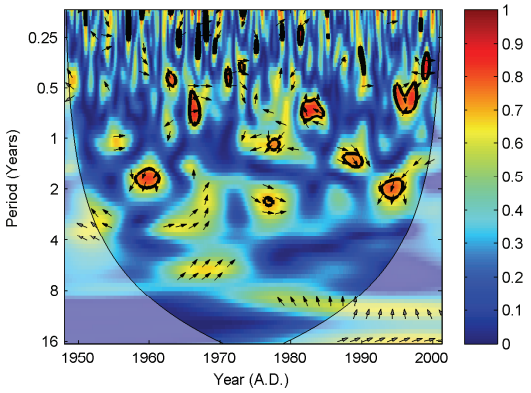

Figure 1. Squared wavelet coherence between AO and QBO. The 5% significance level against red noise is shown as a thick contour. The relative phase relationship is shown as arrows (with in-phase pointing right, anti-phase pointing left, and QBO leading AO by 90° pointing straight down).

links between solar cycle and AO, which may not be dependent on the QBO, can be found. For this analysis we use the I from (5) and ρ from (6). We firstly filter both time series with a Paul wavelet centred on 11 years. We also did the analysis with various other filters – the results are very insensitive and essentially the same as shown in Figure 2.

[12] To illustrate the results expected from successful application of the method we first examine the relationship between SOI and Niño 3.4 (Figure 2a). It is clear that there is the expected obvious relationship, even when the data are filtered with a 5 year centre frequency Paul wavelet. The peak in I and ρ is at 3 months with SOI leading Niño 3.4, as may be expected physically [*Clarke et al.*, 2000a, 2000b; *Jevrejeva et al.*, 2004]. Figure 2b shows that there is no peak in I when $\Delta > 0$ when sunspot number and AO are examined. The ρ has a pronounced minimum around $\Delta = 0$, where one may actually expect significant coherence if a simple physical relationship existed, but ρ does show a small peak at about $\Delta = 7$ years. However the low significance of the peak may be judged by the much larger peak at $\Delta = -17$ years, which is clearly unphysical as AO does not drive sunspot numbers.

[13] To show that the method is capable of detecting a real relationship between two weakly interacting time series, we show the relationship between AO and Niño 3.4 (Figure 2c), where there is clear relationship in the 14 year band with a $\Delta = 3.5$ years from tropics to Arctic. *Jevrejeva et al.* [2004] found a travel time of about 1 year for 13.9 period year waves to travel from tropics to polar regions due to transmission by slow moving ocean waves that are detectable in global sea surface temperature field. The longer delay found here is likely a result of the method, which in the case of weakly coupled oscillators close to synchrony, always displaces the peak to longer delays in lag space [*Cimponeriu et al.*, 2004].

[14] For completeness we also examined the sunspot - tropical climate relationship by examining its links with the SOI and Niño 3.4 indices (Figures 2d and 2e). Once again there is no peak in I and low values of ρ for all Δ up to 10 years.

4. Discussion

[15] It seems clear that there is no simple causative relationship between sunspot numbers (and hence solar insolation) and multi-year to decadal signals in the large circulation systems that largely define the planet's climate. The non-linear analysis we have done also seems to preclude even quite indirect linkages between solar insolation and the SOI or AO, as we would still expect to see evidence of sunspots cycles being ahead of AO even if that delay was quite variable in absolute months or years. More sophisticated analysis of phase interactions could be done [e.g., *Mokhov and Smirnov*, 2006], however such analyses are more suited to very low noise oscillators, or to where such basic information as the sign of the phase is undetermined. If the solar cycle has the large impacts widely claimed then its influence should be readily seen in simpler analyses. In contrast the 13.9 year cycle phasing is quite readily seen, despite

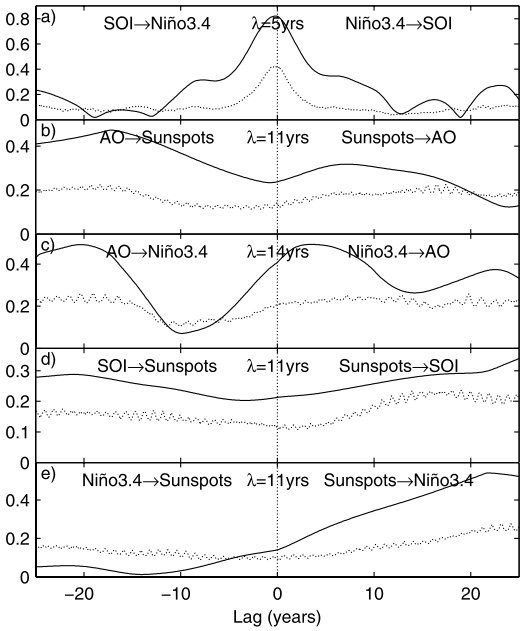

Figure 2. Relationships between time series that have been Paul wavelet filtered with centre frequency λ, expressed as average mutual information, (I), (dotted curves), and mean phase coherence, ρ, (solid line) as a function of the phase lag (Δ) between the series for (a) SOI and Niño3, (b) AO and SC, (c) AO and Niño3, (d) SOI and SC and (e) Niño3 and SC.

it contributing only about 5% of total variance to the SOI, Niño 3.4 and AO indices [*Jevrejeva et al.*, 2004]. Therefore we may confidently assert that the sunspot driving of the AO is certainly less than 5% of total variance; any signal probably accounts for less variance than the plausible limitations of noise in the long atmospheric circulation time series caused by varying spatial coverage, or temperatures being used as proxies for pressure fields.

[16] In time series spanning only 1 or 2 solar cycles it is simply not possible to find significant phase relationships, Figure 1 also illustrates this important point - with only 60 years of data there is only about 20 years of data in the decadal band which are not affected by the data boundaries. While the details of the influence of data boundaries are method-dependent, it is a common feature of the short series regularly used in solar-climate analyses that deriving any statistical significance, especially in realistic red-noise backgrounds, is very challenging.

[17] There is direct evidence from both linear wavelet coherence and from non-linear measures of interactions between time series, that it is the tropics that lead polar climate variability rather than vice-versa as has been proposed for a solar climate driver mechanism. Previous authors have reported numerous examples of 11-year cycles in many different proxy climate records, and often they were assigned to the sunspot cycle. But in the analyses that we have done we find no consistent phase relationship between sunspot numbers and variables such as sea ice extent or spring ice break-up in seas and ports, sea surface temperatures, sea level pressure, and various long meteorological records from cities in Europe. Many of the reports of 11-year cycles come from pure frequency domain analyses such as Fourier transforms, and many of them have dubious levels of significance – either being statistically untested, or only tested against white-noise rather than an appropriate red noise background. In several of these series there is some 11–14 year periodicity that may actually be the 13.9 year signal discussed by *Jevrejeva et al.* [2004] and which seems to be consistently present from the tropics to the polar regions in sea surface temperatures [*Jevrejeva et al.*, 2004], and in various proxy climate series from ice cores [e.g., *Fundel et al.*, 2006]. However, there are other plausible mechanisms for an 11-year cycle. A 5.2–5.7 year cycle is commonly observed in many climate records such as the AO [*Jevrejeva and Moore*, 2001], SSTs from several oceans [*Unal and Ghil*, 1995; *Moron et al.*, 1998], and central England temperatures [*Plaut et al.*, 1995]. A simple doubling of this period comes to 11 years, and such a doubling would be frequently seen, especially in simple Fourier analysis of the data. Natural auto-correlated red-noise in the climate would make this harmonic signal apparently more significant against white-noise background significance tests, thereby leading to claims for an 11 year signal rather than the 5.5 year signal.

5. Conclusion

[18] Numerous authors have considered the apparently self-evident hypothesis that since the sun is the fundamental driving force for the earth's climate, there should be clear links between the main climate patterns and the main index of solar variability. However, rigorous testing of causative links between sunspots and climate indices finds no links on time scales up to about 15 years. Solar driving of climate must be present at timescales relevant to glacial-interglacial cycles and most-likely at shorter scales as well, but solar and climate proxies that meet length and resolution criteria necessary to prove the hypothesis are yet to be adequately tested.

[19] **Acknowledgment.** Financial support came from the Thule Institute and the Academy of Finland.

References

Baldwin, M. P., and T. J. Dunkerton (1999), Propagation of the Arctic Oscillation from the stratosphere to the troposphere, *J. Geophys. Res.*, *104*, 30,937–30,946.

Baldwin, M. P., and T. J. Dunkerton (2001), Stratospheric harbingers of anomalous weather regimes, *Science*, *294*, 581–584.

Baldwin, M. P., and T. J. Dunkerton (2005), The solar cycle and stratosphere-troposphere dynamical coupling, *J. Atmos. Sol. Terr. Phys.*, *67*, 71–82.

Barnston, A. G., and R. E. Livezey (1989), A closer look at the effect of the 11-year solar cycle and the quasi-biennial oscillation on Northern Hemisphere 700 mb height and extratropical North American surface temperature, *J. Clim.*, *2*, 1295–1313, doi:10.1175/1520-0442(1989)002.

Cimponeriu, L. M., G. Rosenblum, and A. S. Pikovsky (2004), Estimation of delay in coupling from time series, *Phys. Rev. E*, *70*, 046213.

Clarke, A. J., J. Wang, and Van Gorder (2000a), A simple warm-pool displacement ENSO model, *J. Phys. Oceanogr.*, *30*, 1679–1691.

Clarke, A. J., J. Wang, and Van Gorder (2000b), Corrigendum: A simple warm-pool displacement ENSO model, *J. Phys. Oceanogr.*, *30*, 3271.

Fundel, F., H. Fischer, R. Weller, F. Traufetter, H. Oerter, and H. Miller (2006), Influence of large-scale teleconnection patterns on methane sulfonate ice core records in Dronning Maud Land, *J. Geophys. Res.*, *111*, D04103, doi:10.1029/2005JD005872.

Grinsted, A., J. C. Moore, and S. Jevrejeva (2004), Application of the cross wavelet transform and wavelet coherence to geophysical time series, *Nonlinear Processes Geophys.*, *11*, 561–566.

Hameed, S., and J. N. Lee (2005), A mechanism for sun-climate connection, *Geophys. Res. Lett.*, *32*, L23817, doi:10.1029/2005GL024393.

Jevrejeva, S., and J. C. Moore (2001), Singular spectrum analysis of Baltic Sea ice conditions and large-scale atmospheric patterns since 1708, *Geophys. Res. Lett.*, *28*, 4503–4506.

Jevrejeva, S., J. C. Moore, and A. Grinsted (2004), Oceanic and atmospheric transport of multi-year ENSO signatures to the polar regions, *Geophys. Res. Lett.*, *31*, L24210, doi:10.1029/2004GL020871.

Kodera, K., and Y. Kuroda (2002), Dynamical response to the solar cycle, *J. Geophys. Res.*, *107*(D24), 4749, doi:10.1029/2002JD002224.

Kuroda, Y., and K. Shibata (2005), Simulation of solar-cycle modulation of the Southern Annular Mode using a chemistry-climate model, *Geophys. Res. Lett.*, *33*, L05703, doi:10.1029/2005GL025095.

Labitzke, K. (2005), On the solar cycle-QBO relationship: A summary, *J. Atmos. Sol. Terr. Phys.*, *67*, 45–54.

Laut, P. (2003), Solar activity and terrestrial climate: An analysis of some purported correlations, *J. Atmos. Sol. Terr. Phys.*, *65*, 801–812.

Mayr, H. G., J. G. Mengel, C. L. Wolff, and H. S. Porter (2006), QBO as potential amplifier of solar cycle influence, *Geophys. Res. Lett.*, *33*, L05812, doi:10.1029/2005GL025650.

Mokhov, I. I., and D. A. Smirnov (2006), El Niño–Southern Oscillation drives North Atlantic Oscillation as revealed with nonlinear techniques from climatic indices, *Geophys. Res. Lett.*, *33*, L03708, doi:10.1029/2005GL024557.

Moron, V., R. Vautard, and M. Ghil (1998), Trends, interdecadal and interannual oscillations in global sea-surface temperatures, *Clim. Dyn.*, *14*, 545–569.

Papoulis, A. (1984), *Probability, Random Variables, and Stochastic Processes*, 2nd ed., McGraw-Hill, New York.

Plaut, G., M. Ghil, and R. Vautard (1995), Interannual and interdecadal variability in 335 years of central England temperatures, *Science*, *268*, 710–713.

Ropelewski, C. F., and P. D. Jones (1987), An extension of the Tahiti-Darwin Southern Oscillation Index, *Mon. Weather Rev.*, *115*, 2161–2165.

Smith, T. M., and R. W. Reynolds (2004), Improved extended reconstruction of SST (1854–1997), *J. Clim.*, *17*, 2466–2477.

Thompson, D. W. J., and J. M. Wallace (1998), The Arctic Oscillation signature in the winter geopotential height and temperature fields, *Geophys. Res. Lett.*, *25*, 1297–1300.

Torrence, C., and G. P. Compo (1998), A practical guide to wavelet analysis, *Bull. Am. Meteorol. Soc.*, *79*, 61–78.

Tsiropoula, G. (2003), Signatures of solar activity variability in meteorological parameters, *J. Atmos. Sol. Terr. Phys.*, *65*, 469–482.

Unal, Y. S., and M. Ghil (1995), Interannual an interdecadal oscillation patterns in sea level, *Clim. Dyn.*, *11*, 255–278.

A. Grinsted and J. Moore, Arctic Centre, University of Lapland, Box 122, FIN-96101 Rovaniemi, Finland. (ag@glaciology.net; john.moore@ulapland.fi)

S. Jevrejeva, Proudman Oceanographic Laboratory, Joseph Proudman Building, 6 Brownlow Street, Liverpool L3 5DA, UK. (sveta@pol.ac.uk)

VII

Oceanic and atmospheric transport of multiyear El Niño–Southern Oscillation (ENSO) signatures to the polar regions

S. Jevrejeva,[1] J. C. Moore,[2] and A. Grinsted[2,3]

Received 29 June 2004; revised 15 October 2004; accepted 1 December 2004; published 24 December 2004.

[1] Using Monte-Carlo Singular Spectrum Analysis (MC- SSA) and Wavelet Transform (WT) we separate statistically significant components from time series and demonstrate significant co-variance and consistent phase differences between ice conditions and the Arctic Oscillation and Southern Oscillation indices (AO and SOI) at 2.2, 3.5, 5.7 and 13.9 year periods. The 2.2, 3.5 and 5.7 year signals detected in the Arctic are generated about three months earlier in the tropical Pacific Ocean. In contrast, we show that the 13.9 year signal propagates eastward from the western Pacific as equatorial coupled waves (ECW, 0.13–0.15 ms^{-1}), and then as fast boundary waves (1–3 ms^{-1}) along the western margins of the Americas, with a phase difference of about 1.8–2.1 years by the time they reach the Arctic. Our results provide evidence of dynamical connections between high latitude surface conditions, tropical ocean sea surface temperatures mediated by tropical wave propagation, the wintertime polar vortex and the AO. *INDEX TERMS:* 1620 Global Change: Climate dynamics (3309); 3309 Meteorology and Atmospheric Dynamics: Climatology (1620); 0312 Atmospheric Composition and Structure: Air/sea constituent fluxes (3339, 4504); 4504 Oceanography: Physical: Air/sea interactions (0312); 4522 Oceanography: Physical: El Nino. **Citation:** Jevrejeva, S., J. C. Moore, and A. Grinsted (2004), Oceanic and atmospheric transport of multiyear El Niño–Southern Oscillation (ENSO) signatures to the polar regions, *Geophys. Res. Lett.*, *31*, L24210, doi:10.1029/2004GL020871.

1. Introduction

[2] Several studies indicate that the relationships between the El Niño-Southern Oscillation (ENSO) and climate anomalies in the North Atlantic (NA) sector are both weak and ubiquitous, however most evidence of linkage comes from model simulations [e.g., *Trenberth et al.*, 1998; *Merkel and Latif*, 2002] or from 50 years of reanalysis data [*Ribera and Mann*, 2002]. What is missing is clear observational evidence, especially spanning long time periods. Impacts of ENSO are more plausibly seen in the NA sector during winter than summer, though the signal to noise ratio is rather low [*Trenberth et al.*, 1998; *Huang et al.*, 1998; *Pozo-Vázquez et al.*, 2001]. These considerations motivated us to use the NH time series of ice conditions and advanced statistical methods to extract signals associated with ENSO. Our idea is that ENSO signals can be extracted from the ice conditions time series, since ice extent is an integrated parameter of winter seasons and acts as a non- linear filter for 2–13 year oscillations during the winter seasons [*Jevrejeva and Moore*, 2001]. ENSO quasi-biennial (QB) and quasi- quadrennial (QQ) signals were detected by Monte Carlo Singular Spectrum Analysis (MC-SSA) in time series of the Northern Hemisphere (NH) annular mode (NAM) and ice conditions in the Baltic Sea [*Jevrejeva and Moore*, 2001], which are consistent with results obtained for the time series of sea ice cover from the Arctic and Antarctic [*Gloersen*, 1995; *Venegas and Mysak*, 2000]. This paper focuses on the dynamic linkages, and putative mechanisms, especially for the low frequency component (13.9 year signal), between the ENSO and NAM circulation indices and between the NH ice conditions and polar/tropical circulation patterns over the past 150 years using the MC-SSA and crosswavelet and wavelet coherence methods.

2. Data

[3] We used a 135-year time series of the monthly SOI [*Ropelewski and Jones*, 1987], as the atmospheric component of ENSO and the Niño3 SST index (1857–2001) [*Kaplan et al.*, 1998], defined as the monthly SST averaged over the eastern half of the tropical Pacific (5°S–5°N, 90°–150°W) as the oceanic part. To ensure the robustness of the results, we repeated the analyses for the monthly Niño1+2 (0°–10°S, 90°–80°W) and monthly Niño3.4 (5°S–5°N, 170°–120°W) time series [*Kaplan et al.*, 1998]. NAM was represented by the monthly AO index based on the pressure pattern (1899–2001) [*Thompson and Wallace*, 1998] and the extended AO index (1857–1997) based on the pattern of surface air temperature anomalies [*Thompson and Wallace*, 1998].

[4] Measures of winter season severity come from the time series of maximum annual ice extent in the Baltic Sea (BMI), 1857–2000 [*Seinä and Palosuo*, 1996], April ice extent in the Barents Sea (BE: Eastern part 10°–70°E; and BW: Western part 30°W–10°E), 1864–1998 [*Venje*, 2001] and the date of ice break-up at Riga since 1857 [*Jevrejeva and Moore*, 2001]. Global SST since 1854 were taken from the Extended Reconstructed Sea Surface Temperature (ERSST) [*Smith and Reynolds*, 2003] 2° × 2° dataset down-sampled to yearly values.

3. Methods

[5] The analysis is performed using MC-SSA [*Allen and Smith*, 1996] and wavelet transform (WT) with a Morlet wavelet [*Foufoula-Georgiou and Kumar*, 1995]. We applied MC-SSA to calculate the contribution from non-linear long-term trends and quasi-regular oscillations to total variance, and analyse their development over time. We used the WT to determine both the dominant modes of variability and

[1]Proudman Oceanographic Laboratory, Birkenhead, UK.
[2]Arctic Centre, University of Lapland, Rovaniemi, Finland.
[3]Also at Department of Geophysics, University of Oulu, Oulu, Finland.

0094-8276/04/2004GL020871$05.00

Table 1. Contribution From Significant Components Detected by MC-SSA in Time Series of SOI, Niño3, AO, and Ice Conditions to the Total Variance[a]

	Period (years)			
Contribution (%)	2.2	3.5	5.7	13.9
SOI	3	27	18	4
Niño3		**3**	**7**	4*
AO	**9**		3	6
Barents sea		1	2	4
Baltic sea	5	**3**	**4**	3
Riga	**4**	4	5	**5**

[a]Rows in bold indicate EOFs at 95% in an AR(1) red-noise model, * indicate EOFs at 90% level, others are significant at 95% level in white noise models.

how those modes vary in time. Statistical significance was estimated against a red noise model. We calculated a coherence measure of the intensity of the covariance of the two series in time-frequency space [*Torrence and Webster*, 1999]. Phase difference between the components of the two time series was estimated as the circular mean of the phase for those regions with higher than 5% statistical significance and which are outside the cone of influence [*Jevrejeva et al.*, 2003].

4. Results

[6] Decomposition of time series of SOI, Niño3, AO and ice conditions are presented in Table 1. Signals with 2.2, 3.5, 5.7 and 13.9 year periodicities were detected in ice conditions time series and associated with similar signals in SOI/Niño3. Results are consistent with QB and QQ detected by [*Gloersen*, 1995; *Venegas and Mysak*, 2000] in shorter time series of ice conditions in polar regions and with signals in SST and sea level pressure (SLP) anomalies over the Pacific Ocean [*Huang et al.*, 1998; *Torrence and Webster*, 1999; *White and Tourre*, 2003; *Ribera and Mann*, 2002]. As expected, the signals, detected in ice time series, are rather weak; with 1–6% contribution to the total variance, however, this amounts to 20–25% of all statistically significant signals (Table 1).

[7] To investigate the direct link between the localised signals from atmospheric circulation index and ice conditions we use crosswavelet and coherency methods. Results for the Barents Sea ice conditions with AO/Niño3 (Figures 1a and 1c) and Baltic Sea with AO/SOI (Figures 1b and 1d) show that the phase lag where coherency >0.8 (corresponding to the 95% significance level) is consistently about 3 months for the 2.2–5.7 year signals. The same lag has also been found for the NA region [*Pozo-Vázquez et al.*, 2001].

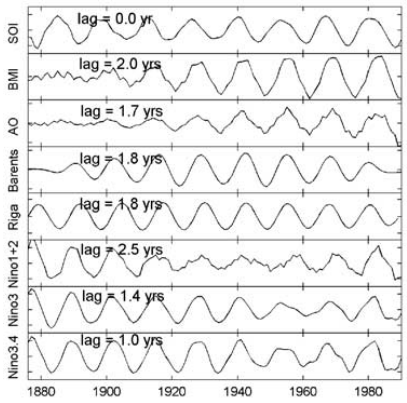

Figure 2. 13.9 year signals from time series of SOI, ice extent in the Baltic Sea, AO, ice extent in the Barents Sea, time series of date of ice break-up at Riga, Niño1+2, Niño3, Niño3.4.

[8] Wavelet coherence between SOI, Niño3, AO and ice conditions is significant in the 12–20 year band. Using MC-SSA we isolated the 13.9 year oscillations in time series (Figure 2). The phase relationship between the oscillations was then determined by cross spectral density estimates (relative to SOI). The 13.9 year SOI signal leads the AO by 1.7 years and ice conditions by 1.8–2.1 years. We also found a 1.4 year lag between the 13.9 year signals from SOI and Niño3. The different phase relationship between signals with periodicities of 2.2–5.7 and 13.9 years suggests different mechanisms of signal propagation from the equatorial Pacific Ocean to the polar regions for the 13.9 year signal and for the shorter period ones.

[9] The mechanism linking between the QB oscillations (2.2–3.5 years) signals detected in ice conditions time series and in tropical forcing, has been described by *Baldwin and Dunkerton* [2001], as extra-tropical wave propagation,

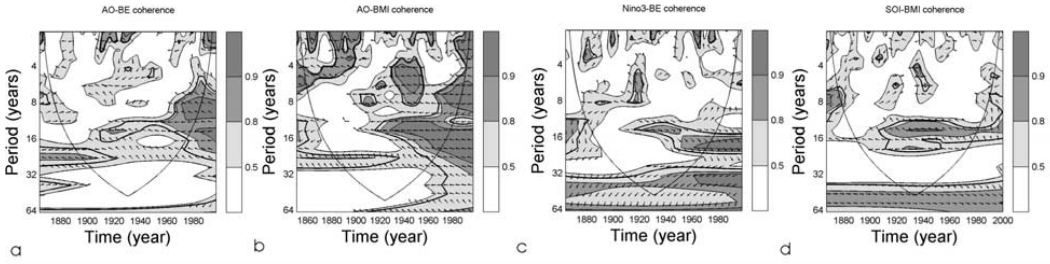

Figure 1. The wavelet coherency and phase difference between AO/ice extent in the Barents Sea (a). Contours are wavelet squared coherencies. The vectors indicate the phase difference a) horizontal arrow pointing from left to right signifies in-phase and an arrow pointing vertically upward means the second series lags the first by 90 degrees (i.e., the phase angle is 270°); b) the same for the AO/ice extent in the Baltic Sea; c) the same for the Niño3/ice extent in the Barents Sea; d) the same for the SOI/ice extent in the Baltic Sea.

affecting breakdown of the wintertime stratospheric polar vortices. Since the AO may be interpreted as a physical phenomenon associated with the structure of the polar vortex and related changes in the stratospheric and tropospheric pressure fields and the stratospheric polar vortex affects surface weather patterns, the QBO has an effect on high latitude weather patterns [*Baldwin and Dunkerton*, 2001; *Castanheira and Graf*, 2003]. The marked similarity in the phase lag of the 5.7 year signal to that of QB signal in SOI and ice conditions strongly suggests a similar mechanism of propagation.

[10] We hypothesize that the lag between SOI and Niño3 signals can be explained by propagation of ECW on a decadal scale [*White et al.*, 2003; *Capotondi and Alexander*, 2001], from off-equatorial wind stress curl and triggered ECW by reflected coupled Rossby waves (CRW). We consider Rossby waves as a solution to the problem of adjustment of the geophysical fluid to large-scale perturbation, based on the conservation of angular momentum. *Wang and Weisberg* [1994] found that ECW propagate eastward across the Pacific at speed of 0.28 ms^{-1}. *White et al.* [2003] showed the existence of coupled waves occurring in response to Rossby wave reflection on the western boundary that propagate eastward with phase speeds of about 0.12 ms^{-1} on decadal period scales. These waves propagate slowly eastward along the equator in the Pacific Ocean in concert with global SST/SLP waves. To investigate these decadal-scale waves, on the assumption that they are identifiable in the 13.9 year signals found in the SOI and Niño3 series, we analysed the phase difference between the 13.9 years signals from SOI, Niño3, Niño1+2 and Niño3.4 calculated by MC-SSA (Figure 2). The results provide evidence of an increase of phase difference for 13.9 year signals with eastward propagation. Using these lags gives an eastward propagation speed of 0.13–0.17 ms^{-1} for 13.9 year signals along the equator, which is in excellent agreement with the speed of decadal- period ECW described by *White et al.* [2003].

[11] We have projected the 13.9 year signal extracted from SOI on the SST anomalies in the Pacific (1854–1997) (Figure 3). The strength of correlation and the phase of correlation maps illustrate a meridional V-shape pattern, which is symmetric along the equator, propagating eastward across the ocean, with a speed of 0.15 ms^{-1} interrupted in the central tropical Pacific Ocean by the development of anomalous warm/cool tongues. When ECW reach the margins of North and South America they transform to baroclinic Kelvin boundary waves (KBW), propagating polewards [*Enfield and Allen*, 1980; *Meyers et al.*, 1998], of which the most energetic waves can reach as far north as Alaska [*Meyers et al.*, 1998]. They are thought to start near the equator with Kelvin wave-like structure, and evolve towards a continental shelf wave structure at higher latitudes [*Suginohara*, 1981]. This mechanism is well-established for equatorial Kelvin waves. For ECW, the excitation of boundary Kelvin waves may be due to a combination of the incoming ocean signal and forcing by coupled wind stress at the boundary (*Clark* [1992] suggested that wind stress becomes relatively more important at longer periods).

[12] Fast poleward propagation of KBW (a few months) is confirmed by the phase angle map (Figure 3b), where we can trace the propagation along the western margin of South and North America and also along the Arctic continental shelf.

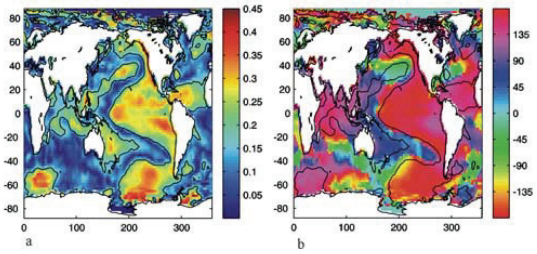

Figure 3. Map of magnitude of correlation between SST and the in-phase and quadrature 13.9 year SOI cycle, 95% significance is delineated by the black line (a). Map of relative phase angle (degrees) between the SST and in-phase and quadrature SOI 13.9 year cycle (b).

[13] A noticeable feature of Figure 3 is the strong 13.9 year signal around the Antarctic, a similar 13.9 year signal was reported as a long-standing feature in 2000 year ice core record from the Antarctic [*Fischer et al.*, 2004], which they ascribed to a mode of variability in the Antarctic Circumpolar Wave (ACW). However, the ACW has also been thought of as an ENSO teleconnnection, and *Park et al.* [2004] argue strongly that it is a geographically phase-locked standing wave train linked to tropical ENSO episodes. This ENSO-modulated quasi-stationary variability is not zonally uniform, rather, the strongest ENSO impact is consistently concentrated in the Pacific sector of the Southern Ocean, as we observe in Figure 3.

5. Conclusion

[14] We provide evidence of ENSO influence on the winter climate variability in NH during the last 150 years via signals in the 2.2, 3.5, 5.7 and 13.9 year bands. The contribution from the signals to the total variance is relatively weak, varies considerably with time, but is statistically significant. Phase relationships for the different frequency signals suggest that there are different mechanisms for distribution of the 2.2–5.7 year and the 13.9 year signals. The 2.2–5.7 year signals are most likely transmitted via the stratosphere, and the AO mediating propagation of the signals, through coupled stratospheric and tropospheric circulation variability that accounts for vertical planetary wave propagation.

[15] The delay of about two years in the 13.9 year signals detected in polar region can be explained by the transit time of the 13.9 year signal associated with ECW (0.13–0.17 ms^{-1}) propagation in the Pacific ocean, KBW (1–3 ms^{-1}) propagation along the western margins of the Americas and by poleward-propagating of atmospheric angular momentum [*Dickey et al.*, 2003]. This mechanism is supported by similar features in the Pacific sector of the Antarctic SST field.

[16] Our results highlight the importance of tropical variations for the Arctic and NA climate and probably at least the Pacific sector of the Antarctic, suggesting a global mode of interaction between atmosphere and ocean and consistent with GCM experiments of a proposed ENSO-NA

link [e.g., *Trenberth et al.*, 1998; *Dong et al.*, 2000; *Merkel and Latif*, 2002].

[17] **Acknowledgments.** Financial assistance was provided by NERC and the Thule Institute. Software is available at http://www.pol.ac.uk/home/research/waveletcoherence. We thank two anonymous referees.

References

Allen, M. R., and L. A. Smith (1996), Monte Carlo SSA, detecting irregular oscillations in the presence of coloured noise, *J. Clim.*, *9*, 3383–3404.

Baldwin, M. P., and T. J. Dunkerton (2001), Stratospheric harbingers of anomalous weather regimes, *Science*, *294*, 581–584.

Capotondi, A., and M. A. Alexander (2001), Rossby waves in the tropical North Pacific and their role in decadal thermocline variability, *J. Phys. Oceanogr.*, *31*, 3496–3515.

Castanheira, J. M., and H.-F. Graf (2003), North Pacific–North Atlantic relationships under stratospheric control?, *J. Geophys. Res.*, *108*(D1), 4036, doi:10.1029/2002JD002754.

Clark, A. J. (1992), Low-frequency reflection from a nonmeriodional eastern ocean boundary and the use of coastal sea level to monitor eastern Pacific equatorial Kelvin waves, *J. Phys. Oceanogr.*, *22*, 163–183.

Dickey, J. O., S. L. Marcus, and O. Viron (2003), Coherent interannual and decadal variations in the atmosphere-ocean system, *Geophys. Res. Lett.*, *30*(11), 1573, doi:10.1029/2002GL016763.

Dong, B.-W., R. T. Sutton, S. P. Jewson, A. O'Neil, and J. M. Slingo (2000), Predictable winter climate in the North Atlantic sector during the 1997–1999 ENSO cycle, *Geophys. Res. Lett.*, *27*, 985–988.

Enfield, D. B., and J. S. Allen (1980), On the structure and dynamics of monthly mean sea level anomalies along the Pacific coast of North and South America, *J. Phys. Oceanogr.*, *10*, 557–578.

Fischer, H., F. Traufetter, H. Oerter, R. Weller, and H. Miller (2004), Prevalence of the Antarctic Circumpolar Wave over the last two millennia recorded in Dronning Maud Land ice, *Geophys. Res. Let.*, *31*, L08202, doi:10.1029/2003GL019186.

Foufoula-Georgiou, E., and K. Kumar (1995), *Wavelets in Geophysics*, 373 pp., Elsevier, New York.

Gloersen, R. (1995), Modulation of hemispheric sea-ice cover by ENSO events, *Nature*, *373*, 503–505.

Huang, J., K. Higuchi, and A. Shabbar (1998), The relationship between the North Atlantic Oscillation and the ENSO, *Geophys. Res. Lett.*, *25*, 2707–2710.

Jevrejeva, S., and J. C. Moore (2001), Singular spectrum analysis of Baltic Sea ice conditions and large-scale atmospheric patterns since 1708, *Geophys. Res. Lett.*, *28*, 4503–4507.

Jevrejeva, S., J. C. Moore, and A. Grinsted (2003), Influence of the Arctic Oscillation and El Niño-Southern Oscillation (ENSO) on ice conditions in the Baltic Sea: The wavelet approach, *J. Geophys. Res.*, *108*(D21), 4677, doi:10.1029/2003JD003417.

Kaplan, A., M. A. Cane, Y. Kushnir, A. C. Clement, M. B. Blumenthal, and B. Rajagopalan (1998), Analyses of global sea surface temperature 1856–1991, *J. Geophys. Res.*, *103*, 18,567–18,589.

Merkel, U., and M. Latif (2002), A high resolution AGCM study of the El Niño impact on the North Atlantic/European sector, *Geophys. Res. Lett.*, *29*(9), 1291, doi:10.1029/2001GL013726.

Meyers, S. D., A. Melsom, G. T. Mitchum, and J. J. O'Brien (1998), Detection of the fast Kelvin waves teleconnection due to El Niño Southern Oscillation, *J. Geophys. Res.*, *103*, 27,655–27,663.

Park, Y.-H., F. Roquet, and F. Vivier (2004), Quasi-stationary ENSO wave signals versus the Antarctic Circumpolar Wave scenario, *Geophys. Res. Lett.*, *31*, L09315, doi:10.1029/2004GL019806.

Pozo-Vázquez, D., M. J. Esteban-Parra, F. S. Rodrigo, and Y. Castro-Diez (2001), The association between ENSO and winter atmospheric circulation and temperature in the North Atlantic region, *J. Clim.*, *14*, 3408–3420.

Ribera, P., and M. Mann (2002), Interannual variability in the NCEP reanalysis 1948–1999, *Geophys. Res. Lett.*, *29*(10), 1494, doi:10.1029/2001GL013905.

Ropelewski, C. F., and P. D. Jones (1987), An extension of the Tahiti-Darwin Southern Oscillation Index, *Mon. Weather Rev.*, *115*, 2161–2165.

Seinä, A., and E. Palosuo (1996), The classification of the maximum annual extent of ice cover in the Baltic Sea 1720–1995, *Rep. Ser. 27*, pp. 79–91, Finn. Inst. Mar. Res., Helsinki.

Smith, T. M., and R. W. Reynolds (2003), Extended reconstruction of global sea surface temperatures based on COADS data (1854–1997), *J. Clim.*, *16*, 1495–1510.

Suginohara, N. (1981), Propagation of coastal-trapped waves at low latitudes in a stratified ocean with continental shelf slope, *J. Phys. Oceanogr.*, *11*, 1113–1122.

Thompson, D. W. J., and J. M. Wallace (1998), The Arctic Oscillation signature in the winter geopotential height and temperature fields, *Geophys. Res. Lett.*, *25*, 1297–1300.

Torrence, C., and P. Webster (1999), Interdecadal changes in the ENSO-monsoon system, *J. Clim.*, *12*, 2679–2690.

Trenberth, K. E., W. Branstator, D. Karoly, A. Kumar, N. Lau, and C. Ropelewski (1998), Progress during TOGA in understanding and modeling global teleconnections associated with tropical sea surface temperatures, *J. Geophys. Res.*, *103*, 14,291–14,324.

Venegas, S. A., and L. A. Mysak (2000), Is there a dominant timescale of natural climate variability in the Arctic?, *J. Clim.*, *13*, 3412–3434.

Venje, T. (2001), Anomalies and trends of sea ice extent and atmospheric circulation in the Nordic Seas during the period 1864–1998, *J. Clim.*, *14*, 255–267.

Wang, C., and R. H. Weisberg (1994), On the "slow mode" mechanism in ENSO- related coupled ocean-atmosphere models, *J. Clim.*, *7*, 1657–1667.

White, W. B., and Y. M. Tourre (2003), Global SST/SLP waves during the 20th century, *Geophys. Res. Lett.*, *30*(12), 1651, doi:10.1029/2003GL017055.

White, W. B., Y. M. Tourre, M. Barlow, and M. Dettinger (2003), A delayed action oscillator shared by biennial, interannual, and decadal signals in the Pacific Basin, *J. Geophys. Res.*, *108*(C3), 3070, doi:10.1029/2002JC001490.

A. Grinsted and J. C. Moore, Arctic Centre, University of Lapland, FIN-96101 Rovaniemi, Finland.

S. Jevrejeva, Proudman Oceanographic Laboratory, Birkenhead CH43 7RA, UK. (sveta@pol.ac.uk)

VIII

JOURNAL OF GEOPHYSICAL RESEARCH, VOL. 111, C09012, doi:10.1029/2005JC003229, 2006

Nonlinear trends and multiyear cycles in sea level records

S. Jevrejeva,[1] A. Grinsted,[2,3] J. C. Moore,[2] and S. Holgate[1]

Received 16 August 2005; revised 19 May 2006; accepted 12 June 2006; published 12 September 2006.

[1] We analyze the Permanent Service for Mean Sea Level (PSMSL) database of sea level time series using a method based on Monte Carlo Singular Spectrum Analysis (MC-SSA). We remove 2–30 year quasi-periodic oscillations and determine the nonlinear long-term trends for 12 large ocean regions. Our global sea level trend estimate of 2.4 ± 1.0 mm/yr for the period from 1993 to 2000 is comparable with the 2.6 ± 0.7 mm/yr sea level rise calculated from TOPEX/Poseidon altimeter measurements. However, we show that over the last 100 years the rate of 2.5 ± 1.0 mm/yr occurred between 1920 and 1945, is likely to be as large as the 1990s, and resulted in a mean sea level rise of 48 mm. We evaluate errors in sea level using two independent approaches, the robust bi-weight mean and variance, and a novel "virtual station" approach that utilizes geographic locations of stations. Results suggest that a region cannot be adequately represented by a simple mean curve with standard error, assuming all stations are independent, as multiyear cycles within regions are very significant. Additionally, much of the between-region mismatch errors are due to multiyear cycles in the global sea level that limit the ability of simple means to capture sea level accurately. We demonstrate that variability in sea level records over periods 2–30 years has increased during the past 50 years in most ocean basins.

Citation: Jevrejeva, S., A. Grinsted, J. C. Moore, and S. Holgate (2006), Nonlinear trends and multiyear cycles in sea level records, *J. Geophys. Res.*, *111*, C09012, doi:10.1029/2005JC003229.

1. Introduction

[2] The rate of global mean sea level rise over the last decade (1993–2000) determined from TOPEX/Poseidon altimeter measurements is 2.6 ± 0.7 mm/yr [*White et al.*, 2005], which is significantly larger than estimates (1–2 mm/yr) of the 20th century linear trend for sea level rise [*Church et al.*, 2001], and has reignited the discussion on whether sea level rise is accelerating. Long term sea level rates come from sea level gauge stations, that now number in excess of 1000. However, most of these stations were established in the 1950s, with only a handful extending back 100 years or more. According to *White et al.* [2005], decadal trends in the global reconstruction of sea level vary from 0 to 4 mm/yr during the period 1950–2000, with a maximum during the 1970s. However, *Holgate and Woodworth* [2004] argue that in 10-year trends since 1950, the highest rates of sea level rise occurred in the 1990s, with the lowest rates in the 1980s.

[3] In this paper we address the development of the regional and global nonlinear sea level trends over the full length of tide-gauge records, however as pre-20th century records are sparse and geographically very limited, we focus on the 20th century. We use several novel approaches in calculating mean sea level and errors for ocean regions and then analyze the sea level using Monte-Carlo Singular Spectrum Analysis (MC-SSA) with confidence intervals for nonlinear trends [*Allen and Smith*, 1996; *Moore et al.*, 2005]. This approach provides information on changes in contribution from 12 large ocean regions to global sea level rise over time. In addition, we use wavelet and wavelet coherence methods [*Torrence and Compo*, 1998; *Grinsted et al.*, 2004] to investigate the role of signals with periods of 2–13.9 years in the variability of sea level records, their links to the large scale atmospheric circulation patterns and how these relationships have changed over the past 100 years.

[4] In previously published results [see, e.g., *Church et al.*, 2001; *Nerem and Mitchum*, 2002], linear trends were calculated by ordinary least squares methods, which can produce misleading results if the residuals do not have a white noise spectrum [*Kuo et al.*, 1990]. Additionally, most tide gauge records demonstrate distinctly nonuniform trends, which makes the linear trends sensitive to the arbitrarily chosen start and end dates. Here we apply MC-SSA to extract nonlinear long-term trends from time series of mean sea level. We filter the low frequency variability by removing the statistically significant 2–13.9 year oscillations associated with large scale atmospheric circulation [*Unal and Ghil*, 1995; *Jevrejeva et al.*, 2005]; along with multidecadal oscillations (14–30 year periods). We then estimate the nonlinear long-term trend, providing the statistical significance of the trend, and its confidence intervals.

2. Data and Methodology

2.1. Tide Gauge Stations

[5] We aimed to use all relative sea level (RSL) monthly mean time series in the Permanent Service for Mean Sea Level (PSMSL) database [*Woodworth and Player*, 2003]. However, data from Japan were excluded from the analysis

[1] Proudman Oceanographic Laboratory, Liverpool, UK.
[2] Arctic Centre, University of Lapland, Rovaniemi, Finland.
[3] Also at Department of Geophysics, University of Oulu, Oulu, Finland.

0148-0227/06/2005JC003229$09.00

due to uncertainty in earthquake-related land movement of bench marks and tide gauge stations. Detailed descriptions of the RSL time series are available from www.pol.ac.uk/psmsl. No inverted barometer correction was applied. RSL data sets were corrected for local datum changes and glacial isostatic adjustment (GIA) of the solid Earth [*Peltier*, 2001]. In the GIA data set there were missing rates for several stations particularly in Arctic Siberia, and much of Australia. We addressed these deficiencies in GIA by assigning a station with no GIA correction the same GIA as the nearest station within 100 km of it. If no GIA corrected station was within 100 km, we used an interpolation scheme in assigning GIA rates from stations up to 1000 km away. Stations further than 1000 km from sites with assigned GIA were removed from the analyses.

[6] There is no common reference level for the tide gauge records and this provides a problem when stacking records that do not cover the same time periods. One way overcome this problem is to calculate the rate of change in sea level for each station and stack the rates [*Barnett*, 1984]. However, many stations have historically only been measured for some months of the year and an annual cycle in sea level could therefore lead to severe bias. To maximize data usage, we calculate the mean annual rate for a given month over a whole year (e.g., the rate in January is calculated as the July to July difference). Using this method removes all systematic sub-annual signals from the data. Data gaps shorter than one year in the final rate series are filled by interpolation. This procedure results in data from 1023 stations containing 385324 individual monthly records, of which 22130 months were filled by interpolation. The maximum number of stations in any year is 585, with only 70 stations in 1900, and 5 in 1850. Due to the time lag between data collection and supply to the PSMSL recent decades have also seen reductions in station numbers with only 390 stations in 2000.

2.2. Regional Trends

[7] The geographical distribution of tide gauges provides a poor sampling of the ocean basins, and most of tide gauges are situated in the Northern Hemisphere (Europe, Japan, and the United States). Additionally tide gauge records do not cover the same time period. It is useful to define 12 sea level regions (Figure 1) and calculate the mean sea level time series for the each region. The degree to which a station represents fluctuations in sea level across a region, and errors in the sea level measurements of stations are key issues in estimating region sea level trends. We use two independent methods of estimating these. The first is the standard method of the statistical bi-weight robust mean and variance [*Mosteller and Tukey*, 1977], commonly used in dendrochronology to produce mean indices that are robust in excluding time series that are far from the median series. This procedure leads to a mean and a standard error estimate directly from all the stations in a region. The second method we employ seeks to resolve the issue of spatial inhomogeneity. The stations are not evenly distributed spatially, and therefore we have developed a novel way of stacking the stations. Dealing separately with each region of the world ocean (Figure 1), we recursively find the two closest stations (x and y) and merge them creating a new virtual station located halfway between the original stations.

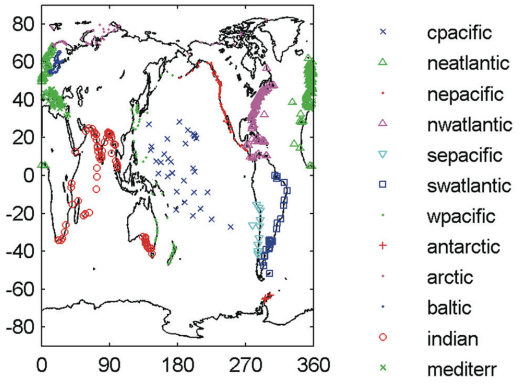

Figure 1. Location of the tide gauges included in this study (12 regions: cpacific, Central Pacific; neatlantic, northeast Atlantic; nepacific, northeast Pacific; nwatlantic, northwest Atlantic; sepacifc, southeast Pacific; swatlantic, southwest Atlantic; wpacific, western Pacific; antarctic, Antarctica; arctic, Arctic; baltic, Baltic; indian, Indian; mediterr, Mediterranean).

The error for the virtual station for the i^{th} year can be written as

$$e_i = \sqrt{m_i^2 + r_i^2}, \tag{1}$$

where m is the measurement error associated with each station measurement and r is the misfit error, that is the difference in sea level trend recorded at the two stations in any particular year. The error e is treated as a measurement error when a virtual station is merged with another station in the next step in the recursion. Generally time series from x and y do not span exactly the same period. The mean measurement error (m) is then calculated as

$$m_i = \frac{\sqrt{m_{x,i}^2 + m_{y,i}^2}}{n_i}, \tag{2}$$

where m_x and m_y are the measurement errors of station x and y respectively. In years where only one station has data $n_i = 1$ and the other is simply left out of the equation, otherwise $n_i = 2$. The misfit error tells how well the virtual station represents stations x and y and is written

$$r_i = \frac{\sigma_{xy}}{2\sqrt{n_i}}, \tag{3}$$

where σ_{xy} is calculated as the standard deviation of the rates at x minus those at y over the interval of common overlap. When the recursive procedure has been carried out we are left with the sea level rate of the entire region and its associated error.

[8] Figure 2 shows the yearly sea level rate of change in the eastern North Atlantic region with the bi-weight mean and the virtual station method. The general features agree

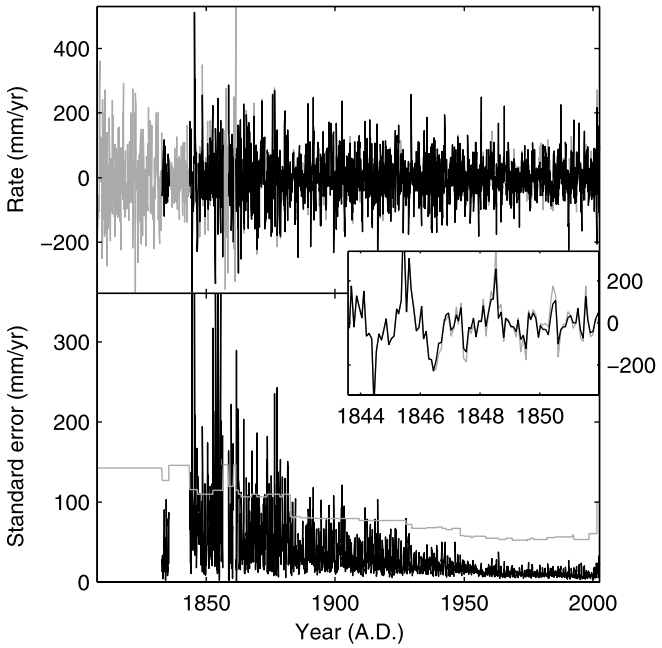

Figure 2. Comparison of the northeastern Atlantic sea level rates from monthly data (top and zoomed inset showing generally close agreement in the two estimates) and associated standard error (bottom) estimated using bi-weight robust means (black) and the virtual station method (grey) from equation (1).

well over most of the full length of the record, though it can be see that the bi-weight mean estimate tends to have smaller amplitude in some periods where statistical outliers are removed from the robust mean. Note that there is very little overall trend apparent in the rate curve. The variation in the standard errors shows more interesting differences between the methods. In the early part of the record, when there are few stations, the two methods give quite similar estimates of the errors. However, when the number of stations becomes much larger in the middle of the 20th century, the bi-weight standard error becomes much smaller than the virtual station estimate. This is because the simple assumption of statistical independence inherent in the bi-weight method, reduces the standard error of the mean by the square root of the number of stations. However, the virtual station error remains large as it is dominated by the station mismatch error in the final step of the recursion process, when two far-apart stations that generally have large mismatch, are meaned. This reflects the true limit of how representative a single curve is of region-wide sea level. Therefore the virtual station error is a much more reliable estimate of uncertainty than a simple robust standard error.

2.3. Global Sea Level

[9] Previous authors have used estimates of the linear trends for oceanic basins (found by averaging the basin rates) to compute a simple global trend by taking the mean and the error in the mean between basins [*Douglas*, 1997]. Simple averaging of these errors would lead to incorrect uncertainties in sea level rise. Despite the relatively large virtual station error estimates, we find that integrating the trends results in positive rates in all regions over the last 150 years. This strongly suggests that errors in rates are not random, but caused by systematic oscillations in sea level within the regions which will be manifested as autocorrelation within the errors. We define a region mismatch error (b_i) as the difference in sea level rates between that in the particular region and the mean over all the regions in the i^{th} year. We can correct for the autocorrelated fraction of the b_i error by considering its power spectrum (Figure 3). The power spectrum shows a marked decrease with frequency, due to the importance of multiyear oscillations in sea level. Since the low frequencies dominate the total mismatch error, we should reduce the mismatch error estimate on the yearly rates by the square root ratio of the high frequency power to the low frequency power, (P). From Figure 3 it can be seen that this ratio is typically about 2–3 and so the between-region sea level yearly rate error estimate should be only about 1/2 of the standard error found simply by considering the rates between regions. To calculate the total error in the global trend (g_i) we need to add (as a vector) this between-region error to the station representativity error (again correcting for the power spectrum of the error).

$$g_i = P\sqrt{b_i^2 + \frac{\sum_j e_{ij}^2}{N_i^2}} \tag{4}$$

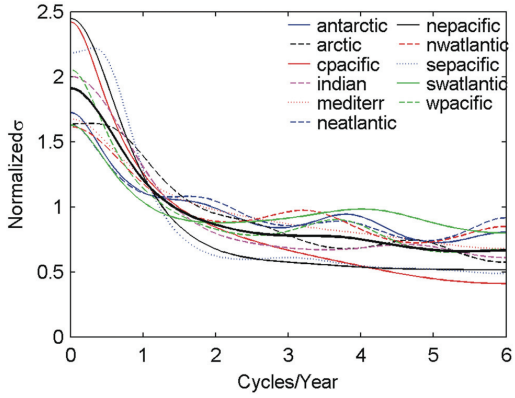

Figure 3. Normalized square rooted power spectrum of the mismatch error between each of the regions (Figure 1), except the Baltic, and the mean global sea level rate, calculated using an order 6 maximum entropy method. The thick black curve is the region mean spectrum. The power spectrum peaks at low frequencies due to long period oscillations, while the high frequency tail represents the "correct" mismatch error.

where N_i is the number of regions with stations operating in the i^{th} year, and e_{ij} is the e_i from equation (1) in jth region. This is the error that we shall report in global rate estimates.

2.4. Sea Level Analysis

[10] In this study the sea level time series were considered as a combination of the long-term trends, oscillations and noise. For trend analysis we use a novel approach [*Moore et al.*, 2005] that has significant advantages over traditional low-pass filtering in that we can estimate the significance of the trend, its confidence intervals and its contribution to the total series variance. We decompose the time series using the MC-SSA [*Allen and Smith*, 1996] with data-adaptive orthogonal filters, separating the original time series into the nonlinear low frequency trend, quasiperiodic signals and noise, distributed among the filters. We use an embedding dimension of equivalent to 30 years, which means low frequency oscillations will appear as trends in a similar way to filtering with a Gaussian of 60 year cutoff period [*Moore et al.*, 2005]. We calculate the statistical significance of components reconstructed by convoluting the original series with each of the filters and comparing against red noise models (Monte Carlo method, with 1000 surrogate series with the same length, observed variance and lag-one autocorrelations as the original time series). All results presented in this paper are statistically significant at the 95% level against white noise models, and many are also significant against red noise models. The contribution from the trends and quasi-regular oscillations to the total variance, are calculated as a projected component relative to the original time series. Finally, we remove the effects of the short timescale variability (2–30 years) from the time series, then extract the long-term trends and analyze their development over time. *Mann* [2004] discusses methods of calculating trends close to the observational boundaries, and we use a variation on the minimum roughness criterion here. We implement the minimum roughness by extrapolating the time series 30 years forward and backward in time using a least squares linear fit onto the 30 years of data nearest to a boundary before applying the SSA nonlinear trend filter. The nonlinear trend at the data boundaries may therefore be said to be composed of 30 data points and 29 extrapolated points from the linear trend.

[11] In comparison with the least squares linear fits, often used to compute confidence intervals of means, we have the advantage of requiring errors to conform only to the optimal data adaptive filter specifying the trend, and thus find that confidence intervals in nonlinear time series are perhaps 3–4 times smaller than found by linear fitting [*Moore et al.*, 2005].

[12] Nonlinear trends for regional sea level yearly rate are calculated from the integrated mean regional monthly rates to give a sea level curve, then performing MC-SSA to extract the nonlinear trend and finally differentiating to give the nonlinear trend in regional sea level rate. This method avoids uncertainties in decomposing the monthly rate where the trend accounts for a small fraction of the variance in the data, whereas using the integrated data the trend often accounts for 50% of the variance.

[13] Global sea level rate is calculated by simply averaging the regional rates (the Baltic being excluded, as discussed later). Global sea level is found from the mean of the regional sea level curves. The error in global sea level is estimated from the standard deviation of the regional sea level curves for each year, however, the errors produced are not statistically independent for similar reasons as those discussed earlier in relation to equation (4), and so we estimate the confidence interval using a "jack knife" method [*Press et al.*, 1992] which can compensate for this effect.

[14] To investigate the role of 2–30 year oscillations we use MC-SSA and wavelet methods. We apply the wavelet method [*Torrence and Compo*, 1998] and decompose the time series into time –frequency space, in order to determine both the dominant modes of variability and how those modes vary in time. We compare results with the oscillations detected by MC-SSA, and the consistency of the results obtained by these independent methods strengthens their credibility.

[15] To analyze the direct links between the statistically significant components in regional sea level time series and time series representing the large scale atmospheric circulation we use the wavelet coherence method [*Grinsted et al.*, 2004; *Jevrejeva et al.*, 2005]. We give descriptions of the changes in covariance between time series and show that there is considerable linkage between the statistically significant components in time series of sea level and atmospheric circulation.

3. Results

3.1. Nonlinear Trends in Sea Level

[16] Figure 4 shows the rates of the nonlinear trends in 10 of the 12 regions (Antarctic and southeastern Pacific, time series are too short to perform trend analysis). Figure 5 shows the mean global sea level and its nonlinear trend with

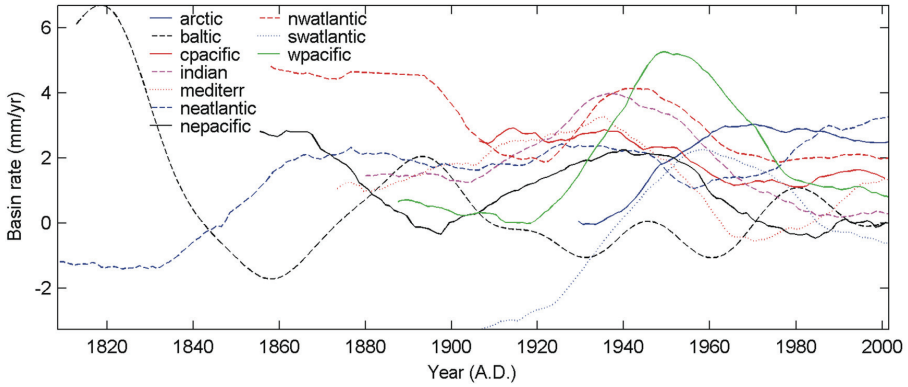

Figure 4. Rates of nonlinear sea level trends in the regions defined in Figure 1, found using an SSA embedding dimension equivalent to 30 years. Errors are not shown in the plot, but using the example of Figure 2 for northeastern Atlantic, the maximum error at the start of the time series would be about $150P/\sqrt{(12 \times 30 \times 2)} = 2-3$ mm yr^{-1} and the minimum error about 1 mm yr^{-1}; other regions will have similar errors. Note that extrapolation at data boundaries means that curves are increasingly more uncertain within 30 years of the start and end of the records.

95% confidence interval, and also the nonlinear global sea level rate. Only 5 stations were active during 1850 and all of them were in the North Atlantic or the Baltic (Figure 4), so estimates of global trends are rather uncertain before 1900, as is reflected in the large errors in Figure 5. The large acceleration in sea level 1850–1870 coincides with a few new stations becoming active, and is probably not statistically significant.

[17] In contrast with linear trends, where the rate of mean sea level rise is constant, our results (Figure 4) reveal the evolution of sea level rise during the 20th century and show that the highest regional rates of up to 3–5 mm/yr occurred between 1920–1950 (with some regional variations, e.g., the later maximum for the southwestern Atlantic and western Pacific). The major contributions to the global sea level rise during 1920–1940 are from the northwestern Atlantic (4.2 ± 1.0 mm/yr), Indian (3.5 ± 1.0 mm/yr), and Mediterranean (3.1 ± 1.0 mm/yr) regions. Even smoothed by the 30 year SSA window, the trends from the different ocean regions show slightly dissimilar patterns and still demonstrate some cyclic variability. This cyclicity is associated with longer term oceanic variations [e.g., *Ghil*, 2001], changes in thermal expansion and water mass adding to the ocean, which may provide nonuniform regional sea level rise, and melting of continental ice leads to the significant geographic variations in the sea level change due to both gravitational and loading effects [*Mitrovica et al.*, 2001].

[18] A notable feature of Figure 4 is that for the last 20 years the regional trends are more coherent in the sense that the trends are closely grouped, and the rates for the southern and northern hemisphere become similar. The trend for the Baltic Sea is strongly influenced by limited water exchange with larger regions and fresh water flux variations [*Meier and Kauker*, 2003] which leads to its rate curve being quite dissimilar from the other regions, and in our study we have excluded the Baltic Sea time series from the calculation of the global sea level trend. Arctic sea level trend has been accelerating for the last 30 years, which can be explained by the warming of the Arctic coupled with increased influx of warmer Atlantic waters to the arctic region, the increase of fresh water inflow from Siberian rivers [*Dickson et al.*, 2002; *Wu et al.*, 2005], and changes in the Arctic Ocean circulation [*Proshutinsky et al.*, 2001].

[19] Applying a least squares linear regression analysis to the global sea level in Figure 5 gives a trend of 1.8 mm/yr between 1900 and 2000, as found in earlier studies [*Church*

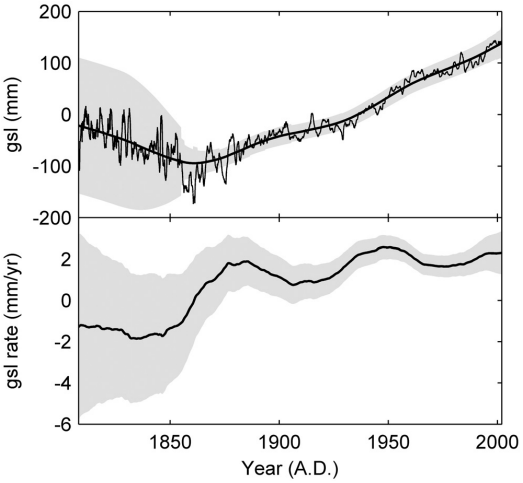

Figure 5. (top) Nonlinear trend (thick black line) in global sea level using an SSA embedding dimension equivalent to 30 years. Paralleling the trend is the 95% confidence interval in the trend found by considering the mismatch between the regional sea level curves; thin curve is the yearly global sea level. (bottom) Rate of the global sea level trend, and its standard error from equation (4).

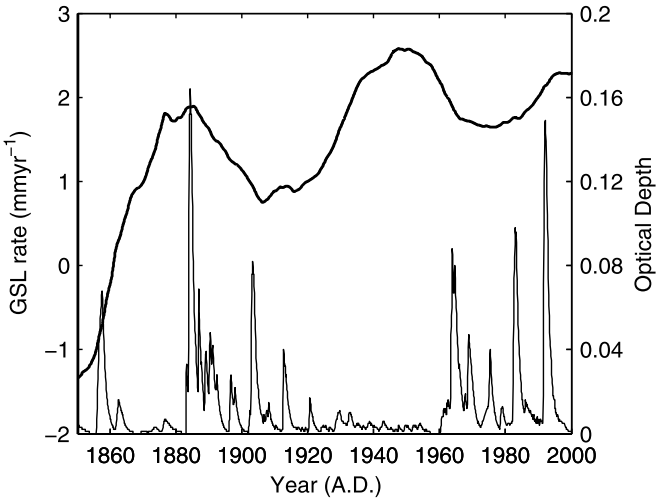

Figure 6. Rate of the nonlinear global sea level trend (thick black line, mm/yr) and stratospheric aerosol optical depth (thin line) [*Sato et al.*, 1993].

et al., 2001]. However, our results show that global sea level rise is irregular and varies greatly over time, it is apparent that rates in the 1920–1945 period are likely to be as large as today's. Nevertheless, considerable uncertainties remain.

[20] The nonlinear trend for the 1990s show about the same sea level rise (2.4 ± 1.0 mm/yr) as TOPEX/Poseidon, which demonstrates the ability of the nonlinear trend to resolve (with certain errors) the temporal evolution of the spatial sea level field. The largest contributions to the global sea level trend during the 1990s are from northwestern Atlantic, northeastern Atlantic and Arctic regions (Figure 4), which is in good agreement with results from *Levitus et al.* [2005] showing the warming of the Atlantic regions providing the largest contribution to the global ocean heat content during 1955–2003.

[21] Sea level is an integrated indicator of climate variability, which reflects changes in the dynamic and thermodynamic in atmosphere, ocean and cryosphere. Both land surface [*Jones and Moberg*, 2003] and sea surface temperature data [*Kaplan et al.*, 1998; *Rayner et al.*, 2003] are in good agreement with the gsl curve in Figure 5, in particular, the increases from 1910 to 1940, and from 1980 until the present, as well as a stagnation between 1940 and 1975. One possible explanation for the sea level acceleration during 1920–1945 was the low level of volcanic activity. Recently published model results [*Church et al.*, 2005] suggest that multiyear to decadal sea level variability is significantly affected by volcanic activity. The climate system responds to volcanic forcing on a range of timescales. The short period (generally lasting 1–3 yrs) response is mainly due to stratospheric aerosols from explosive volcanic eruptions scattering incoming solar short wave radiation, which leads to cooling of the global average temperature [*Sato et al.*, 1993; *Robock and Liu*, 1994; *Robock*, 2000] and a reduction in rainfall [*Robock and Liu*, 1994; *Gillett et al.*, 2004; *Lambert et al.*, 2004]. A simple comparison between the rate of sea level rise and stratospheric aerosol optical thickness, the principal parameter affecting stratospheric aerosol climate forcing [*Sato et al.*, 1993], is shown in Figure 6 and suggests that rapid sea level rise prior to 1980 occurred during periods of low volcanic activity. While it is tempting to perform regression modeling of sea level on the trends in optical depth and e.g., global temperature, it is problematic as the short term volcanic impact on global temperatures means that the variables are highly co-dependent. Applying regression on MC-SSA trend data (effectively moving averaged with a 60 year window) reduces the available degrees of freedom in 150 years of data to the point where fits are statistically insignificant. However, our hypothesis is supported by the results from the SI200 version of Goddard Institute for Space Studies (GISS) simulations, where since 1950, minima in the ocean heat content occurred due to the large volcanic eruptions of Agung, El Chichon and Pinatubo [*Hansen et al.*, 2002]. The observed ocean heat content [*Levitus et al.*, 2005] provides evidence of cooling after all three eruptions (Agung, El Chichon, and Pinatubo). *Bengtsson et al.* [1999] also demonstrate that the Pinatubo eruption had a recognizable effect on climate, with direct forcing limited in duration to a few years and a long-term effect, lasting 7 years, due to cooling of the oceans.

3.2. Role of Oscillations in the 2–30 Year Band

[22] Using MC-SSA, we extract statistically significant components from time series of regional sea level. Signals in the 3.5–13.9 year band contribute from 5 to 20% of variability in time series. There is also a substantial contribution from signals with 13–30 year periodicity. In our study signals with 13–30 year periodicity from regional time series are statistically significant against a white noise model. However, for individual stations these signals are statistically significant against red noise [*Unal and Ghil*, 1995]. Our results are in good agreement with oscillations detected at 3.5, 5.2–5.7, 7–8.5 and 10–13.9 years for individual sea level station time series by *Unal and Ghil*

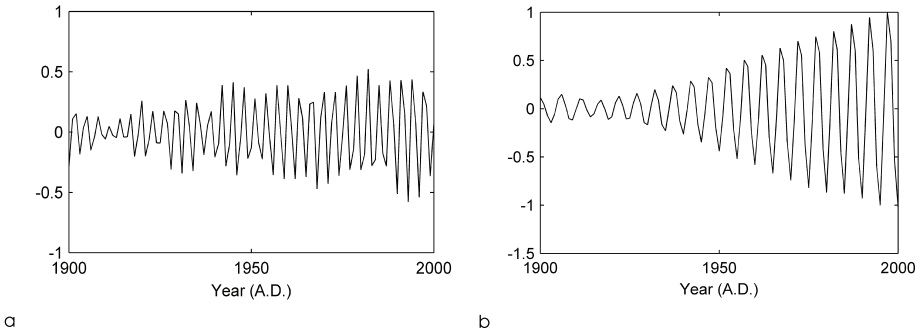

Figure 7. (a) Standardized sum of the statistically significant (at the 95% confidence level against red noise model) SSA components for the 3.5- and 2.4-year oscillations in time series of mean sea level in northeastern Atlantic region; (b) for 5.2-year oscillations in northeastern Pacific. Both showing increased amplitude since 1950.

[1995]. It is notable that 3.5–13.9 year oscillations demonstrate an increase in amplitude since the 1940s in several regions: northeastern Atlantic, northwestern Atlantic, and eastern Pacific, presented in Figure 7.

[23] To isolate the different timescales of variability, and analyze the changes of variance in the time series of sea level we examine their behavior in time-frequency space using the Morlet wavelet. Figure 8 shows the wavelet power spectrum of 4 regional sea level time series, displayed as a function of cycle period and time. The left axis is the Fourier period; the bottom axis shows the time in years. The strong nonstationary behavior of the spectra is clearly seen. Most of the time series show an increase of power in the wavelet power spectrum at 2–30 year periods since 1940s.

[24] Oscillations in the 2.2–7.8 year band in individual sea level records have been associated with large scale atmospheric circulation signals [*Unal and Ghil*, 1995; *Jevrejeva et al.*, 2005], which generate a sea level response through a number of processes: the direct influence of changed atmospheric pressure, changes in wind stresses, and changes in atmosphere-ocean fluxes as well as storm surges. Previously published results have revealed the influence of large scale atmospheric circulation on sea level variability for various ocean basins. According to the *Hughes et al.* [2003] Antarctic sea level is highly coherent with the Antarctic Annular Mode (AAO). Substantial contributions from changes in large scale atmospheric circulation patterns to the sea level variability in Arctic were found by *Proshutinsky et al.* [2001]. The role of the SOI index in variability in the Pacific sea level is discussed by *Church et al.* [2004].

[25] To identify the frequency bands within which time series of sea level and the large scale atmospheric circulation are co-varying, we use the wavelet coherency method [*Grinsted et al.*, 2004; *Jevrejeva et al.*, 2005]. Figure 9a demonstrates the influence of the Arctic Oscillation (AO) [*Thompson and Wallace*, 1998] on the variability of the North Atlantic associated with 2.2–13.9 year signals after 1940, which is in excellent agreement with results for the individual records reported by *Jevrejeva et al.* [2005]. Influence of the North Atlantic Oscillation (NAO) [*Jones et al.*, 1997] in the Mediterranean region, shown by *Tsimplis and Josey* [2001], is associated with 2.2–7.8 year signals (Figure 9b). There is also evidence of a shift in the period of maximum coherence from the 2.2–3.5 to the 3.5–7.8 year band for the northeastern Atlantic after 1950 and noticeable changes in the 2.2–5.7 year band for the Mediterranean region.

[26] Indian and Pacific Oceans sea level variability is mainly associated with Southern Oscillation Index (SOI) [*Ropelewski and Jones*, 1987] signals at 2.2, 3.5, 5.7 year periods. Figures 9c and 9d demonstrate that the relationship is not stationary and the influence of SOI has generally increased over the last 60 years over a broadening spectrum of periods. Our results (Figure 9d) show increasing influence from 13.9 year signal, previously found in Sea Surface Temeprature (SST) in the Pacific Ocean and extending to the polar regions [*Jevrejeva et al.*, 2004]. We also use the Pacific Decadal Oscillation (PDO) index [*Zhang et al.*, 1997], derived as the leading mode of monthly SST anomalies in the North Pacific Ocean, as a representation of the Pacific climate variability. The signature of the 2.2–30 year signals, associated with PDO, is clearly seen in the eastern Pacific sea level variability (not shown here). The PDO's influence since 1940 shows an increase in the low frequency power in the 13–30 year band, somewhat similar to seen for the SOI in Figure 9d, and large changes in the 3.5–7.8 year band. Our results are consistent with a previous study by *Church et al.* [2004] where SOI was found to be strongly anticorrelated (−0.78) with the first Empirical Orthogonal Function (EOF) of sea level in the Pacific. Furthermore, increased variance is sea level is associated with a tendency for ENSO events to be more frequent, persistent and intense in the equatorial Pacific in the last two decades.

4. Discussion

[27] Our global sea level trend estimate of 2.4 ± 1.0 mm/yr for the period from 1993 to 2000 matches the 2.6 ± 0.7 mm/yr sea level rise found from TOPEX/Poseidon altimeter data. However, Figure 5 suggests that during 20th century a similar sea level rise was observed between 1920 and 1945.

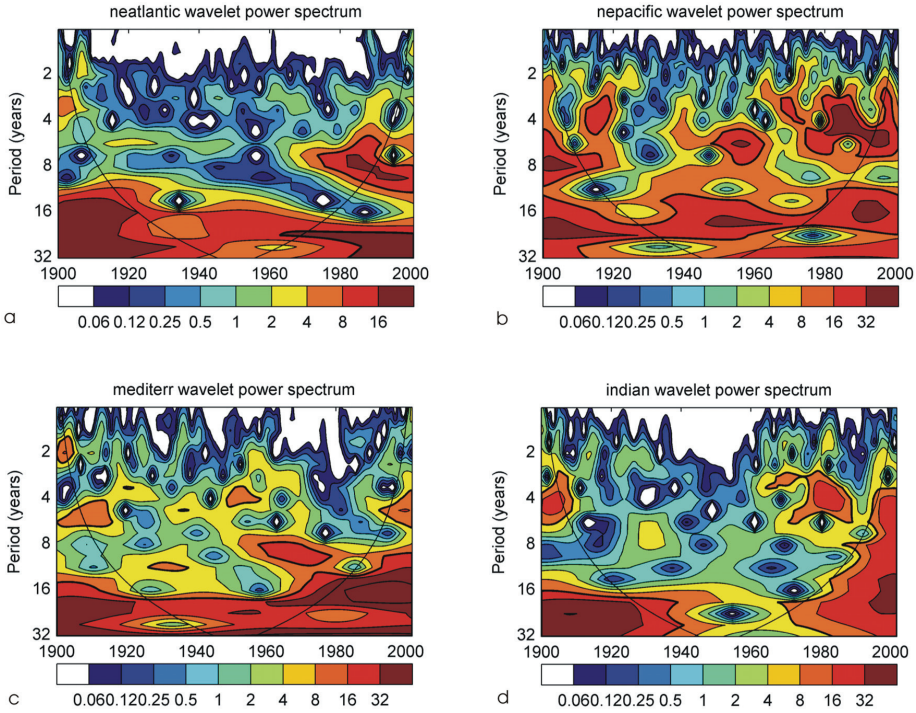

Figure 8. Wavelet power spectrum (Morlet) of mean monthly mean sea level for the (a) northeastern Atlantic; (b) northeastern Pacific; (c) Mediterranean; (d) Indian. Contours are in variance units. In all panels the black thick line is the 5% significance level using the red noise model; solid line indicates the cone of influence. The color bar represents normalized variances. All of the time series show an increase of power in the wavelet power spectrum at 2–30 year periods since 1940s as can be seen by the spread of the red and yellow shading to the upper rights of the panels.

The maximum rate of global mean sea level rise was 2.5 ± 1.0 mm/yr during the period 1920–45, with cumulative rise of 48 mm in 25 years.

[28] These results differ slightly from previously published conclusions [e.g., *Cazenave and Nerem*, 2002] concerning historical rates of mean sea level rise during recent decades. Most probably the difference in the results can be explained by the use of different data (number of stations, location of the stations), GIA corrections, methods and errors for trend calculation. *Church et al.* [2004] pointed out that with decadal variability in the computed global mean sea level, it is not possible to detect a significant increase in the rate of sea level rise over the period 1950–2000. However, results from *White et al.* [2005] suggest that decadal reconstructed sea level trends have varied from 0 to 4 mm/yr since 1950. The results of *Holgate and Woodworth* [2004] for the second half of the 20th century reveal that the highest rates in decadal sea level trends were in the 1990s, but the lowest rises were in the 1980s, demonstrating a significant variation in rates of sea level rise.

[29] Furthermore, observed ocean heat content, the major contributor to sea level rise, has significant decadal variability [*Levitus et al.*, 2005]. According to results from simulations using the GISS global climate model these decadal heat content changes do not appear to be caused by the climate forcing, but are more likely to be dynamical features [*Hansen et al.*, 2002]. Similar results are found with the National Centre for Atmospheric Research (NCAR) Parallel Climate Model [*Barnett et al.*, 2001]. Multidecadal variability in sea level records most probably links to the variability in the heat transported by the thermohaline circulation, driven by the temperature and salinity differences [*Deser and Blackmon*, 1993; *Rajagopalan et al.*, 1998; *Rodwell et al.*, 1999]. Such changes in the thermal structure of the ocean can result in steric (density) sea level changes [*Knutti and Stocker*, 2000].

[30] Our results show that there is an increase in 2–30 year variability is sea level over the recent decades for several regions. We speculate that one of the possible sources for increase in 2–13.9 year variability could be the large scale atmospheric circulation represented by the SOI, AO, NAO and PDO.

[31] Figure 4 shows some evidence that the nonlinear trends for the different regions are in closer agreement around 1980 than previously, though it must be noted that errors in the trends are relatively large. Additionally Figure 8 shows that 2–30 year variability is increasing.

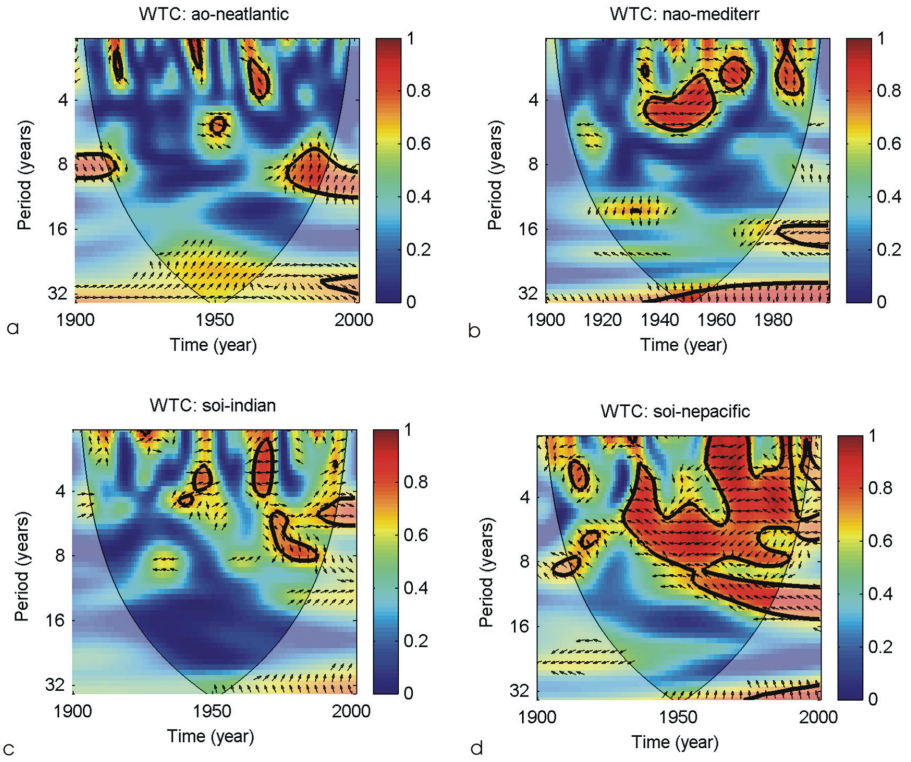

Figure 9. (a) Wavelet coherency between AO/sea level in the northeastern Atlantic; (b) the same for the NAO/Mediterranean sea level; (c) the same for the SOI/Indian Ocean sea level; (d) the same for the SOI/northeastern Pacific sea level. Contours are wavelet squared coherencies. The vectors indicate the phase difference (a horizontal arrow pointing from left to right signifies in-phase, and an arrow pointing vertically upward means the second series lags the first by 90 degrees (i.e., the phase angle is 270°)). In all panels the black thick line is the 5% significance level using the red noise model. Data analyzed are annual sea level.

One possible explanation is a warmer ocean makes the large scales more coherent, as ocean temperature and heat content increase in all regions of the world. At the same time, the 2–13.9 year variability in sea level records in some regions, for example, North Atlantic, Mediterranean Sea, eastern Pacific, and Indian Oceans associated with atmospheric forcing, which has increased over the last 50 years [*Wakelin et al.*, 2003; *Jevrejeva et al.*, 2005], shows the relationship is changing with time. This phenomenon may be expected on theoretical grounds [e.g., *Tsonis*, 2004]. It is likely as a warmer ocean leads to more large scale teleconnections, while also tending to introduce more variability at any particular place [*Tsonis*, 2004]. This can be seen in Figure 9d where long period signals increase in strength and generally the Pacific sea level at all frequencies is seen to be more coherent with SOI. Increases in high frequency coherency in the Pacific (Figure 9d) are also suggestive of the increasing frequency of El-Nino events [*Church et al.*, 2004]. Similar results are seen in many other records of the climate system, for example global temperature records [*Jones and Moberg*, 2003] and 500 mbar pressure height fields [*Tsonis*, 2004]. The manifestation of the climatic mechanisms responsible for the increased long-range teleconnections is presently little understood, but must be related to the low-order dynamics of the global system, for example the increasing rate of El-Nino events, and reduction in La Nina in a warming world discussed by *Tsonis et al.* [2005].

[32] Our study shows the importance of estimates of uncertainties and hence some of the limitation of tide gauges measurements, previously pointed out by *Church et al.* [2004] and *Cazenave and Nerem* [2004]. In our method the estimates explicitly account for the spatial redistribution of sea level, and record the temporal variability better than estimations from individual stations. The errors in the estimates are inevitably quite large, due to the poor special distribution of tide gauges, as they are located only on the continental margins and ocean islands. The alternative method of producing a mean sea level curve by choosing tide gauges from suitable locations by selective criteria, as used by *Douglas* [1997], reduces the number of useful tide gauges to very few (25). Thus a producing

possibly larger error source for sea level estimates [*Cazenave and Nerem*, 2004]. Our results show that error can be reduced with substantial increase of number of tide gauge records; for example, for the period 1800–1900 the errors are 2–3 mm/yr, compare to 1 mm/yr during 20th century.

5. Conclusion

[33] We developed a new "virtual station" method of analyzing sea level records from across different oceanic regions. This is statistically more appropriate than assuming independent errors from all stations in a region, as there are important multiyear cycles in sea level that have different phase lags at stations across an ocean region. We can then get an appropriate sea level curve for each region, and importantly, an error estimate is also produced that can then be used in analysis of the nonlinear trend from SSA with confidence intervals.

[34] We have shown that the development of global sea level rise is highly dependent on the time period chosen and the global sea level rise occurred during the period from 1920 to 1945 is comparable with present-day rate of sea level rise. Nonlinear sea level trends for the ocean regions are nonuniform even after 30 year smoothing (trends in high latitude ocean regions have huge uncertainties, which is a challenge for future study). We provide evidence that 2–13.9 year variability in sea level records is increasing during the past 50 years for most of the ocean basins.

[35] Our study demonstrates the importance of identifying the effect of multiyear to decadal scale anomalies on sea level trends in very short time series. We also show that low-frequency, multidecadal variability is significant and that linear trends do not properly represent this. By removing the high frequency variability we reduce the uncertainties associated with redistribution of sea level due to varying geographical locations of tide gauges along the coastline as well as noise associated with coastal processes and determine the sea level rise driven by the climatic forcing.

[36] We demonstrate that advanced statistical methods improve error estimations and reduce uncertainties for calculation of regional and global sea level rise. However, the main source for the uncertainties in sea level studies using tide gauge records still remain: poor historical distribution of tide gauges, lack of the data from Southern Hemisphere (Africa and Antarctica), the GIA corrections used, and localized tectonic activity.

[37] **Acknowledgments.** Some of our software includes code originally written by E. Breitenberger of the University of Alaska adapted from the freeware SSA-MTM Toolkit: http://www.atmos.ucla.edu/tcd/ssa. We thank the Thule Institute and Finnish Academy for financial support; two anonymous referees provided useful comments.

References

Allen, M. R., and L. A. Smith (1996), Monte Carlo SSA: Detecting irregular oscillations in the presence of coloured noise, *J. Clim.*, *9*, 3383–3404.

Barnett, T. P. (1984), The estimation of "global" sea level change: A problem of uniqueness, *J. Geophys. Res.*, *89*(C5), 7980–7988.

Barnett, T. P., D. W. Pierce, and R. Schnur (2001), Detection of anthropogenic climate change in the world's oceans, *Science*, *292*, 270–274.

Bengtsson, L., E. Roeckner, and M. Stendel (1999), Why is the global warming proceeding much slower than expected?, *J. Geophys. Res.*, *104*, 3865–3876.

Cazenave, A., and R. S. Nerem (2002), Geophysics: Redistributing Earth's mass, *Science*, *294*, 840–842.

Cazenave, A., and R. S. Nerem (2004), Present-day sea level change: Observations and causes, *Rev. Geophys.*, *42*, RG3001, doi:10.1029/2003RG000139.

Church, J. A., J. M. Gregory, P. Huybrechts, M. Kuhn, K. Lambeck, M. T. Nhuan, D. Qin, and P. L. Woodworth (2001), Changes in sea level, in *Climate Change 2001: The Scientific Basis. Contribution of Working Group 1 to the Third Assessment Report of the Intergovernmental Panel on Climate Change*, edited by J. T. Houghton et al., pp. 639–694, Cambridge Univ. Press, New York.

Church, J. A., N. J. White, R. Coleman, K. Lambert, and J. X. Mitrovica (2004), Estimates of the regional distribution of sea level rise over the 1950–2000 period, *J. Clim.*, *17*, 2609–2625.

Church, J. A., N. J. White, and J. M. Arblaster (2005), Significant decadal-scale impact of volcanic eruptions on sea level and ocean heat content, *Nature*, *438*, 74–77.

Deser, C., and H.-G. Blackmon (1993), Surface climate variations over the North Atlantic Ocean during winter: 1900–1989, *J. Clim.*, *6*, 1743–1753.

Dickson, B., I. Yashayaev, J. Meincke, B. Turrell, S. Dye, and J. Holfort (2002), Rapid freshening of the deep North Atlantic Ocean over the past four decades, *Nature*, *416*, 832–837.

Douglas, B. C. (1997), Global sea rise: A redetermination, *Surv. Geophys.*, *18*, 270–292.

Ghil, M. (2001), Natural climate variability, in *Encyclopedia of Global Environmental Change*, vol. 1, edited by M. MacCracken and J. Perry, pp. 544–549, John Wiley, Hoboken, N. J.

Gillett, N. P., A. J. Weaver, F. W. Zwiers, and M. F. Wehner (2004), Detection of volcanic influence on global precipitation, *Geophys. Res. Lett.*, *31*, L12217, doi:10.1029/2004GL020044.

Grinsted, A., J. C. Moore, and S. Jevrejeva (2004), Application of the cross wavelet transform and wavelet coherence to geophysical time series, *Nonlinear Processes Geophys.*, *11*(5/6), 561–566.

Hansen, J., et al. (2002), Climate forcings in Goddard Institute for Space Studies SI2000 simulations, *J. Geophys. Res.*, *107*(D18), 4347, doi:10.1029/2001JD001143.

Holgate, S. J., and P. L. Woodworth (2004), Evidence for enhanced coastal sea level rise during the 1990s, *Geophys. Res. Lett.*, *31*, L07305, doi:10.1029/2004GL019626.

Hughes, C. W., P. L. Woodworth, M. P. Meredith, V. Stepanov, T. Whitworth, and A. R. Pyne (2003), Coherence of Antarctic sea levels, Southern Hemisphere Annular Mode, and flow through Drake Passage, *Geophys. Res. Lett.*, *30*(9), 1464, doi:10.1029/2003GL017240.

Jevrejeva, S., J. C. Moore, and A. Grinsted (2004), Oceanic and atmospheric transport of multi-year ENSO signatures to the polar regions, *Geophys. Res. Lett.*, *31*, L24210, doi:10.1029/2004GL020871.

Jevrejeva, S., J. C. Moore, P. L. Woodworth, and A. Grinsted (2005), Influence of large scale atmospheric circulation on the European sea level: Results based on the wavelet transform method, *Tellus, Ser. A*, *57*, 129–149.

Jones, P. D., and A. Moberg (2003), Hemispheric and large-scale surface air temperature variations: An extensive revision and an update to 2001, *J. Clim.*, *16*, 206–223.

Jones, P. D., T. Jonsson, and D. Wheeler (1997), Extension using early instrumental pressure observations from Gibraltar and SW Iceland to the North Atlantic Oscillation, *Int. J. Climatol.*, *17*, 1433–1450.

Kaplan, A., M. A. Cane, Y. Kushnir, A. C. Clement, M. B. Blumenthal, and B. Rajagopalan (1998), Analyses of global sea surface temperature 1856–1991, *J. Geophys. Res.*, *103*, 18,567–18,589.

Knutti, R., and T. F. Stocker (2000), Influence of the thermohaline circulation on projected sea level rise, *J. Clim.*, *13*, 1997–2001.

Kuo, C., C. Lindberg, and D. J. Thomson (1990), Coherence established between atmospheric carbon dioxide and global temperature, *Nature*, *343*, 709–713.

Lambert, F. H., P. A. Stott, M. R. Allen, and M. A. Palmer (2004), Detection and attribution of changes in 20th century land precipitation, *Geophys. Res. Lett.*, *31*, L10203, doi:10.1029/2004GL019545.

Levitus, S., J. I. Antonov, and T. P. Boyer (2005), Warming of the world ocean, 1955–2003, *Geophys. Res. Lett.*, *32*, L02604, doi:10.1029/2004GL021592.

Mann, M. (2004), On smoothing potentially nonstationary climate time series, *Geophys. Res. Lett.*, *31*, L07214, doi:10.1029/2004GL019569.

Meier, H. E. M., and F. Kauker (2003), Modeling decadal variability of the Baltic Sea: 2. Role of freshwater inflow and large-scale atmospheric circulation for salinity, *J. Geophys. Res.*, *108*(C11), 3368, doi:10.1029/2003JC001799.

Mitrovica, J. X., M. Tamisiea, J. L. Davis, and G. A. Milne (2001), Recent mass balance of polar ice sheets inferred from patterns of global sea-level change, *Nature*, *409*, 1026–1029.

Moore, J. C., A. Grinsted, and S. Jevrejeva (2005), The new tools for analyzing the time series relationships and trends, *Eos Trans. AGU*, *86*, 24.

Mosteller, F., and J. Tukey (1977), *Data Analysis and Regression*, Addison-Wesley, Boston, Mass.

Nerem, R. S., and G. T. Mitchum (2002), Estimates of vertical crustal motion derived from differences of TOPEX/Poseidon and tide gauge sea level measurements, *Geophys. Res. Lett.*, *29*(19), 1934, doi:10.1029/2002GL015037.

Peltier, W. R. (2001), Global glacial isostatic adjustment and modern instrumental records of relative sea level history, in *Sea Level Rise*, edited by B. C. Douglas, M. S. Kearney, and S. P. Leatherman, Elsevier, New York.

Press, W. H., B. Flannery, S. A. Teukolsky, and W. Vetterling (1992), *Numerical Recipes in C*, 2nd ed., Cambridge Univ. Press, New York.

Proshutinsky, A., V. Pavlov, and R. H. Bourke (2001), Sea level rise in the Arctic Ocean, *Geophys. Res. Lett.*, *28*(11), 2237–2240.

Rajagopalan, B., Y. Kushnir, and Y. M. Tourre (1998), Observed decadal midlatitude and tropical Atlantic climate variability, *Geophys. Res. Lett.*, *25*, 3967–3970.

Rayner, N. A., D. E. Parker, E. B. Horton, C. K. Folland, L. V. Alexander, D. P. Rowell, E. C. Kent, and A. Kaplan (2003), Global analysis of sea surface temperature, sea ice, and night marine air temperature since the late nineteenth century, *J. Geophys. Res.*, *108*(D14), 4407, doi:10.1029/2002JD002670.

Robock, A. (2000), Volcanic eruptions and climate, *Rev. Geophys.*, *38*(2), 191–220.

Robock, A., and Y. Liu (1994), The volcanic signal in Goddard Institute for Space Studies three-dimensional model simulations, *J. Clim.*, *7*, 44–55.

Rodwell, M. J., D. P. Rowell, and C. K. Folland (1999), Oceanic forcing of the wintertime North Atlantic Oscillation and European climate, *Nature*, *398*, 320–323.

Ropelewski, C. F., and P. D. Jones (1987), An extension of the Tahiti-Darwin Southern Oscillation Index, *Mon. Weather Rev.*, *115*, 2161–2165.

Sato, M., J. E. Hansen, M. P. McCormick, and J. B. Pollack (1993), Stratospheric aerosol optical depth, 1850–1990, *J. Geophys. Res.*, *98*, 22,987–22,994.

Thompson, D. W. J., and J. M. Wallace (1998), The Arctic Oscillation signature in the winter geopotential height and temperature fields, *Geophys. Res. Lett.*, *25*, 1297–1300.

Torrence, C., and G. P. Compo (1998), A practical guide to wavelet analysis, *Bull. Am. Meteorol. Soc.*, *79*, 61–78.

Tsimplis, M. N., and S. A. Josey (2001), Forcing of the Mediterranean Sea by atmospheric oscillations over the North Atlantic, *Geophys. Res. Lett.*, *28*, 803–806.

Tsonis, A. A. (2004), Is global warming injecting randomness into the climate system?, *Eos Trans. AGU*, *85*, 38.

Tsonis, A. A., J. B. Elsner, A. G. Hunt, and T. H. Jagger (2005), Unfolding the relation between global temperature and ENSO, *Geophys. Res. Lett.*, *32*, L09701, doi:10.1029/2005GL022875.

Unal, Y. S., and M. Ghil (1995), Interannual an interdecadal oscillation patterns in sea level, *Clim. Dyn.*, *11*, 255–278.

Wakelin, S. L., P. L. Woodworth, R. Flather, and J. A. Williams (2003), Sea-level dependence on the NAO over the NW European Continental Shelf, *Geophys. Res. Lett.*, *30*(7), 1403, doi:10.1029/2003GL017041.

White, N. J., J. A. Church, and J. M. Gregory (2005), Coastal and global averaged sea level rise for 1950 to 2000, *Geophys. Res. Lett.*, *32*, L01601, doi:10.1029/2004GL021391.

Woodworth, P. L., and R. Player (2003), The permanent service for mean sea level: An update to the 21st century, *J. Coastal Res.*, *19*, 287–295.

Wu, P., R. Wood, and P. Stott (2005), Human influence on increasing Arctic river discharges, *Geophys. Res. Lett.*, *32*, L02703, doi:10.1029/2004GL021570.

Zhang, Y., J. M. Wallace, and D. S. Battisti (1997), ENSO-like interdecadal variability: 1900–93, *J. Clim.*, *10*, 1004–1020.

A. Grinsted and J. C. Moore, Arctic Centre, University of Lapland, 96101 Rovaniemi, Finland.

S. Holgate and S. Jevrejeva, Proudman Oceanographic Laboratory, Liverpool L3 5DA, UK. (sveta@pol.ac.uk)